Dynamic response of individual cells in heterogeneous population

Farzad Sekhavati

München 2015

Dynamic response of individual cells in heterogeneous population

Farzad Sekhavati

Dissertation
an der Fakultät für Physik
der Ludwig–Maximilians–Universität
München

vorgelegt von
Farzad Sekhavati
aus dem Iran

München, den 27.05.2015

Erstgutachter: Prof. Dr. Joachim O. Rädler
Zweitgutachter: Prof. Dr. Jochen Feldman
Tag der mündlichen Prüfung: 30.07.2015

Contents

Zusammenfassung

Die Betrachtung von biologischen Systemen mit Einzelzellauflösung ermöglicht die Analyse von Heterogenität in Zellpopulationen. Trotz dieser Heterogenität auf Einzelzellniveau, zeigen Populationen ein robustes gemitteltes Antwortsignal gegenüber externen Reizen. In der Systembiologie werden mathematische Modelle verwendet, um Netzwerke der Entscheidungsndung zu beschreiben, die für das Schicksal von Populationen verantwortlich sind. Eine parallelisierbare Hochdurchsatz-Methode für Zellpopulation auf Einzelzellniveau oder einer Population ist für die genaue Zuordnung von experimentellen Daten in den Modellen von großem Nutzen. In der vorliegenden Arbeit haben wir ein Microwell-Array basiertes Lab-on-a-Chip (LoC) System entworfen, entwickelt und hergestellt. Microwell-Arrays ermöglichen es, Zellen auf einem denierten Gitter zu lokalisieren und damit die Genauigkeit und die Geschwindigkeit des automatisierten Verfolgens von einzelnen Zellen zu erhöhen. Das Screening tausender einzelner Zellen wird dadurch ermöglicht. Durch die Kombination von LoC Systemen mit (einer) Lebendzell-Fluoreszenzmikroskopie kann die Dynamik von biologischen Prozessen in Zeitraer-Studien untersucht werden. Mit Hilfe dieser Systeme haben wir zwei prominente Prozesse in der Schicksalsentscheidung von Zellen untersucht, nämlich Stammzelldierenzierung und Apoptose. Stammzelldierenzierungen sind für die Ausbildung aller spezialisierten Zellen im Körper verantwortlich; das Apoptose-Regelnetzwerk schützt gesunde Zellen, indem es beschädigte oder Krebszellen vollständig abbaut.

Wir haben Microwell-Arrays dazu verwendet, um die Bewegung der Progenitorzelle der Makrophagen über 20 Stunden lang zu verfolgen. Es ist allgemein bekannt, dass Makrophagen im Gegensatz zu Progenitorzellen auf Zellkultursubstrat haften. Durch das Verfolgen des Brownschen Bewegungsregimes von Einzelzellen haben wir eine markierungsfreie Technik zur Dierenzierungs-Erkennung entwickelt. Wir konnten zeigen, dass die Differenzierung unmittelbar nach dem Hinzufügen von M-CSF Cytokine beginnt. Innerhalb der ersten 20 Stunden differenzieren 80% der Zellen zu Makrophagen. Die Adhäsions-Detektionstechnik korreliert sehr gut mit den charakteristischen Zeitverläufen von etablierten Fluoreszenzmarkern für Dierenzierung.

Die zweiten Mikroarrays wurden als Microslit entworfen. In den Microslit-Arrays haben bis zu vier einzelne Zellen Platz, d.h. die Familie zweier Generationen von einem einzigen Vorfahren stammend. Mit Hilfe dieser Plattform konnte direkt die Reaktion der Zelle mit ihrem Alter, der sogenannten Zellphase, korreliert werden. Es wird im Allgemeinen angenommen, dass die Wirksamkeit chemotherapeutischer Medikamente mit der Zellzyklusphase korreliert. Als Modellsystem untersuchten wir das Apoptoseverhalten der Leukämie Zelllinie MOLM-13 im Hinblick auf das Medikament Doxorubicin. Interessanterweise beobachteten wir, dass in diesem System das Auslösen der Apoptose nicht vom Zellzyklus abhing. Die Anschaltzeiten der Apoptose folgten einer Gamma Verteilungsfunktion mit einer Verzögerung von 3 Stunden und einer maximalen Sterberate von 5,5 Stunden. Die synchronisierte Population wies eine breitere Verteilung mit der gleichen Verzögerung auf. Wir sind überzeugt, dass die Microslit-Arrays den biologischen Prozess genauer beschreiben können, da Zeitverläufe der Antwortreaktionen der einzelnen Zellen direkt gemessen wer-

den. Über die vorgestellten Methoden hinaus wurde auch Raman-Spektroskopie an unseren LoC Systemen durchgeführt. Wir konnten zeigen, dass diese Technik die Apoptosephasen der einzelnen Zellen direkt identifizierbar macht und eine zuverlässige Methode für eine automatisierbare markierungsfreie Apoptosedetektion ist.

In den Entwicklungsstudien von Einzelzellen wird gewünscht, einzelne Zellen aus der Population zu isolieren. Um dies zu verwirklichen, integrierten wir die Microwell-Arrays-Plattform mit Mikrouidikkanälen. Eine automatisierte Methode für das "drag-and-release" von Zellen mit einer optischen Pinzette wurde vorgestellt, in der einzelne Zellen aus den Microwells selektiert und entnommen werden. In einer ersten Machbarkeitsstudie wurde die Technik verwendet, um haftende und nicht-haftende Zellen in den Microwells zu unterscheiden. Markierungsfreie Methoden in Verbindung mit Lab on Chip (LoC) Systemen können verwendet werden, um die zugrunde liegende stochastische Dynamik von Einzelzellen in Erwiderung auf externe Reize, z.B. Cytokine oder Drogen aufzuklären. Die hier in der Arbeit vorgestellten Methoden und die Reaktionsdynamik dienen als Grundlage für die Entwicklung von personalisierten Medikamenten, sowohl in der regenerativen Medizin durch Stammzellen als auch in der Krebsbehandlung.

Abstract

Looking at biological systems with single cell resolution reveals heterogeneity in populations. Despite the heterogeneity at the single cell level, populations exhibit a robust average response to external stimuli. In systems biology, the aim is to describe the decision making networks responsible for the fate of populations with mathematical models. A high throughput parallel investigation of populations at single cell level is highly beneficial for the accurate mapping of experimental data to the models. In this thesis, we designed, developed and fabricated lab on a chip (LoC) devices based on micro-well arrays. The micro-well arrays localize the cells on a defined lattice, thus increasing the accuracy and speed of the automated single cell tracking. It also enables the simultaneous screening of thousands of single cells. Combining the LoC devices with live cell fluorescent microscopy provides the possibility of investigating dynamics of biological processes in time lapse studies. Using these devices, we studied two prominent fate decision making systems, namely stem cell differentiation and apoptosis. Stem cell differentiations give rise to all of specialized cells in the body and the apoptosis regulatory network protects the healthy cells by clean removal of damaged or cancerous cells.

We have used micro-well arrays to track the motion of the macrophage's progenitor over 20 hours. It is known that macrophages adhere to tissue culture substrate while their progenitors do not. By tracking the Brownian motion regimes of single cells, we established a label free technique for differentiation detection. We showed that the differentiation starts immediately after the addition of M-CSF cytokine, and within the first 20 hours 80% of cells transition to macrophages. The adherence detection technique was correlated well with the time course of known fluorescence markers of differentiation.

The second micro-arrays were designed as micro-slits which can hold up to four single cells, i.e. a family of two generations from a single ancestor. In this platform we were able to directly correlate the cells' responses with their age, i.e. cell phase. It has been suggested that the efficiency of chemotherapeutic drugs can correlated with cell phase. For our study, we followed the apoptosis responses of a leukemia cell line, MOLM-13, to doxorubicin as the model system. Interestingly, we observed that in this system, the apoptosis response did not depend on the cell age. It followed a gamma distribution function with a lag time of 3 hours and maximum killing rate at 5.5 hours. Artificially synchronized population exhibited a broader distribution with the same lag time. We believe that by providing a direct measure of time course of response, the micro-slit arrays can describe the biological process more accurately.

Raman spectroscopy was also performed on our LoC devices. We showed that this technique can directly identify the apoptosis stages in individual cells and is a reliable method for an automated label-free detection of apoptosis.

In the single cell development studies it is desired to extract the cells of interest from the populations. To achieve this functionality, we integrated the micro-array platform with microfluidic channels. An automated method for drag-and-release of cells with optical tweezers was introduced to select and extract individual cells from micro-well arrays. As a proof of principle, the technique was used to distinguish the adherent and non-adherent

cells in the micro-wells.

The label-free methods in combination with lab on a chip devices can be used to resolve the underlying stochastic dynamics of single cells in response to external stimuli, e.g. a cytokine or drug. The methods and response dynamics which were proposed here can be used as a foundation for development of personalized medicine, both in regenerative medicine through stem cells and in personalized cancer treatment plans.

Introduction

In the field of system biology, the complex interaction of cells in a population is investigated and the dynamics of related biological processes are modeled. A precise mathematical models of the system requires a detailed study of individual cells at a large scale. Hence a high throughput single cell study of the population is required to describe the nonlinear dynamics of biological processes [1]. The Fluorescent microscopy of cells *in vitro* has significantly contributed to unravel the code of life or the origin of diseases [2]. There are several end point analysis which can characterize large number of cells at the same time and even sort them according to specific markers, e.g. fluorescence activated cell sorting (FACS) and magnetic activated cell sorting (MACS). However, population studies lack the detail description of the intrinsic dynamics of events or temporal resolution at single cell level.

One of the the central questions in system biology is the cell fate decision making process, e.g. stem cell differentiation, and apoptosis. Recently several studies have used single cell microscopy to investigate the decision making circuits [3, 4, 5, 6]. The common consensus is that the fate of a population rooted in the decisions of individual cells. The variability at single cell level, which was considered noises before, is the necessity of evolution, i.e. fate, of population. The single cell studies confirmed the active role of stochastic noise, in the biological processes and heterogeneity in the population [7, 6]. Colman-Lerner et al. [8] showed that the stochasticity is originated from both the intrinsic and extrinsic noises. The intrinsic noise is the result of stochastic fluctuation in biological process, e.g. the level of expression of each reporter protein. The extrinsic noise is the difference in the level of cellular components needed for expression a reporters. A time lapse microscopy at single cell level provides the temporal resolution, which combined with a high throughput automated system can be used for the modeling of a complex dynamic systems such as biological processes.

The analytical framework which is used for data analysis must be considered at the experimental design step. The average time scale of biological process under study defines the interval of microscopy images. The image processing is the first step to map the biological experiment into the analytical models. Automated tracking with minimum user involvement, both decrease the analysis costs and is less prone to user biased errors. Several

algorithms [9] and image processing softwares [10] has been developed for a rapid and efficient single cell tracking. Buggenthin et al.[11] showed that an out-of-focus brightfield image achieves a stable single cell tracking.

In fluorescent microscopy before any observation is possible, a set of specialized genes must be identified and be fluorescent tagged before the dynamics of that process can be analyzed. A robust label free detection can overcome this as well as common limitations of fluorescent microscopy, such as number of colors and phototoxicity. Several label-free techniques has been developed such as size and morphology classification, impedance [12, 13], and Raman spectroscopy [14, 15, 16].

Lab on a chip devices based on microfluidics have been increasingly used for *in vitro* studies at single cell level [17, 18]. Active and passive microfluidics provide a high throughput single cell screening platform [19]. Micro-arrays, the common passive microfluidics, were used for single cell imaging of highly motile cells such as primary lymphocytes [20], or hematopoietic stem cells [21]. In combination with live cell imaging, it is possible to study the kinetics of biological processes on lab on chip devices. An on stage supply of *in vitro* conditions, i.e. temperature, nutrient, and CO_2 concentration, is required for a long term live cell imaging.

Two of the prominent fate decisions of cells are the stem cell differentiation and apoptosis in cancer treatment. The single cell time lapse studies can identify dynamics of these processes and explain how the population average emerges from this individual responses.

The stem cells differentiation is the corner stone of a highly controlled evolutionary process in biological system. The development starts from a single embryonic stem cell and gives rise to complete organism. The decision making circuits of single cells differentiation ensure the correct development to a complex organism. And the biological networks of stem cells, progenitors and specialized cells maintain a fully functional organism. In recent year, there has been an increasing efforts in single cell time lapse microscopy of stem cells [22]. A differentiation promoting molecule, e.g. a cytokine, can either instruct the cells to differentiate to a specific lineage [23], or by blocking other possibilities favors the survival of that lineage. While for a population both outcomes are the same, single cell time lapse studies can resolve the distribution of the differentiation events. Stem cell research plots a bright future for emerging field of regenerative medicine. The range of applications is from an organ repair to treating neuro-degenerative diseases.

Another well controlled cell fate decision is the cell death. The apoptosis is a crucial mechanism to keep the organism in a healthy and functional state by clean removal of damaged cells. The fate of a cell is controlled through external and internal signaling pathways. At the same time that Kerr et al. [24] coined the term “apoptosis”, they proposed that a damaged apoptosis pathways leads to the development of tumors. Cotter et al. [25] showed that a damages apoptosis pathways causes several type of cancers. The single cell studies showed that the stochasticity and cell-to-cell variability has an effect on the cell commitment to apoptosis [26, 27]. The dynamics of apoptotic pathway plays a big role in cancer treatment.

This thesis is organized in four chapters as follows:
The **1th chapter** is about the design, development, and implementation of the *in vitro* platform. We optimized micro-well arrays to obtain a high throughput automated acquisition platform for time lapse single cell studies. The fluorescent microscopy setup was also upgraded to maintain an on-stage cell culture condition. The CO_2 concentration, temperature, and nutrients was maintained in this setup. We have also introduced an out-of-focus imaging technique. A pipeline of the image processing and data analysis with our in house softwares has also been established.

We have studies the differentiation dynamics of a progenitor cell in **chapter 2**. The progenitor, granulocyte-macrophage progenitor (GMP), is from the family of hematopoietic stem cells (HSCs) and gives rise to two types of white blood cells, namely macrophage and granulocyte. In this chapter we introduced our label-free detection technique based on the random motion of cells inside micro-well array. The differentiation is detected from the motion transition from a non-adherent GMP to an adherent macrophages. The dynamics of GMP to macrophage differentiation was investigated for hundreds of cells in parallel using three fluorescent markers and our label-free technique. We proved that the label-free technique can robustly identify the differentiation events of cells.

In **chapter 3** we investigated the cell fate decision for apoptosis in the response of cancer cell to chemotherapeutic drugs. MOLM-13 cells, a leukemia cell line, was treated with doxorubicin drug. The micro-slit array in this study to confine a two-generations family of cells from a single ancestor. This has two advantages, one the possibility to track the cell cycle using only the first division time of cells, and two is to be able to compare the difference in drug response between sister cells as apposed to non-related cells. We modeled the dynamic response of population at single cell level in an intact, i.e. non-synchronized, and a synchronized MOLM-13 cell lines. The synchronized population has a large mean time of apoptosis with broader distribution. This dynamic suggests that the synchronized cells have a higher chemoresistance to the drug than the intact cells. Interestingly we did not observe a correlation between cell cycle and the efficiency of doxorubicin.

In parallel to fluorescent microscopy, we have included the single cell Raman spectroscopy as a non-invasive, label-free detection of apoptosis. The Raman spectra of a small population of cell was taken at 3 time points after addition of apoptotic drug. The automated time lapse scanning of single cells was possible by using micro-well arrays. We have shown that using principal component analysis Raman spectra has a reliable signature to distinguish apoptotic from live cells.

The **4th Chapter** discusses the micro-manipulation with optical tweezers. The optical tweezers provide a non-invasive manipulation tool to select and move individual cells from the population. We showed that the optical tweezers can be used for a high throughput automated cell sorting microfluidics. The lab on a chip device integrates our micro-well arrays with an active microfluidic channels for cell collection. A drag-and-release procedure by optical tweezers is used for on-chip transportation of single cells of interest to the collection channel. The cell sorting microfluidics combines the benefits of a time lapse studies of dynamics of cell development on-chip and the single cell selection for further off-chip studies. While the time lapse microscopy has inherent limits of the choice of target

genes, we can collect the cells of interest and in the next steps used the genome sequencing techniques for more in-depth study.

Chapter 1

A polymeric micro-array for single cell studies of non-adherent cells

The single cell fluorescent microscopy techniques has been used for time lapse study of the dynamic biological process at the single cell level [3, 4, 5, 6]. Several microfluidic devices has been used to keep the spatio-temporal identity of single cells and at the same time, follow their biological dynamics [18].

This chapter discusses the technical developments of the macro and micro platform that was established here to facilitate the high-throughput parallel single cell studies. To begin with, we introduce the microfluidics systems and more specifically our micro-patterns and their parameters. Second section introduces a suitable *in vitro* condition for cell growth on the microscope stage. At the final section we introduce the software for automated parallel single cell analysis.

1.1 Microfluidics systems

Culturing and investigating cells in culture flasks and tubes has been a common way of *in vitro* cell study in biology. While this is an effective way to see the average response of cell population, it cannot resolve inter cellular interactions. A single cell study requires a well separated population of cells with a precise micro-environment condition. The microfluidics devices provide such conditions.

The field of single cell studies has developed rapidly when the microfabrication techniques from the semi-conductor industry was modified and became available in biology laboratories. The technology had long passed the micron scale barrier, yet the complexity of design and fabrication prevented the wide-range use of them in biology. Softlithography [28], a combination of photolithography from semi-conductor industry and wet bench polymer chemistry, brought the microfabrication industry into the common chemistry laboratory. This reduced the complexity of cleanroom facility which are not readily accessible in biolabs. Early works in this field were done in Whitesides research group at Harvard

[28, 29, 30].

The general term of microfluidics refers to a broad range of applications of micro devices which hold and control the flow of a liquid, e.g. cell culture medium. Microfluidics systems are divided into active and passive devices based on whether they can actively control and manipulate the micro-niches. Active devices such as micro-valves [31] can perform sophisticated chemical processes; even reactions at individual cell level [32]. While passive devices, such as micro-arrays, provide a rapid parallel observation platform.

The microfluidic devices are able to miniaturize the cell culture conditions. Therefore, they can precisely control, manipulate, and monitor the micro-environment [33, 18]. It makes it possible to investigate the heterogeneity of single cell responses on a seemingly homogeneous population under well defined conditions.

We selected passive microfluidics systems to separate individual cells and investigate the stochasticity at single cell level under a defined condition. The environmental condition for cell growth is controlled at micro-liter scale resulting in a homogeneous condition for the whole population.

The tracking of cells becomes even more challenging when we deal with non-adherent cells since they can easily float on the surface and small mechanical disturbance can push them away from the field of view of microscope. While there are several chemical ways to immobilize the cells on the surface, these techniques can put the cells in distress and adversely affect their natural response to the other stimuli. Our microfluidic device localizes the non-adherent cells in a confinement to reduce their motion while keeping them intact.

The automated acquisition system and passive localization of suspension cells enable us to collect statistically significant data in a short time. This set of data is directly comparable on the statistical average to the population studies. The following sections introduce the criteria and choices for the materials, techniques, and geometrical characteristics of micro-patterns.

1.1.1 Microfabrication

The goal of the micro-patterns is to localize non-adherent cells to a predefined lattice sites for an automated microscopy investigation without altering their natural state. At the same time, a parallel, high throughput acquisition, as well as analysis, is desired on this platform. To achieve these goals we developed a micro-pattern substrate which is integrated into a commercially available 6 channel slide (sticky slide VI, ibidi GmbH, Germany) (see Figure 1.5). The standard substrate for this slides is either topas, a cyclic olefin copolymer, or glass (D-263M Schott).

We have examined several common polymers in microfluidics for our micro-patterns. There are four criteria to select target polymers: 1) Biocompatibility, 2) Strong binding to the substrate and high stability under cell-culture condition, 3) Best image quality, 4) Simple fabrication.

Biocompatibility

We tested three polymers: polydimethylsiloxane (PDMS), polyethyleneglycol dimethacry-

late (PEGDMA), and polyethyleneglycol diacrylate (PEGDA). All of these polymers are transparent and biocompatible. PDMS is common choice for microfluidic devices. PEG has also been widely used as a hydrogel in biomedical applications [34, 35] e.g. for drug delivery. Recently, it has been used for microfluidics devices for single cell studies [36, 37, 38] and stem cell niches [38, 39, 40].

Bindings and durability
PEGDMA structures adhere nicely to the dry topas substrate, however under the humid conditions these structures peel off and detach from substrate [41]. PEGDA structures, on the other hand, adhere to the substrate strongly and are stable for several weeks under the cell-culture medium. We kept the samples under the cell-culture medium for 2 month and saw no changes in the structures. Both these polymers do not adhere to the glass substrate. However, coating the glass with 3-(trimethoxysilyl)propyl methacrylate (TMSPMA) monolayer introduces a covalent bond between PEGD(M)A and substrate [42, 43, 44].

High durability under cell culture condition also requires low influence on the chemical composition of medium. PEGDA has lower unspecific absorption than PDMS [45], which in long term leads to lower unspecific nutrient depletion from medium.

Image quality
All of the mentioned polymers have an autofluorescent background signal which can interfere with cell markers signals. Cesaro-Tadic et al. [46] measured the autofluorescent of PDMS in visible light range and found out that it has a high fluorescent in ∼540-630 nm range which overlaps with some of the common fluorescent markers, e.g. Cy3. On the other hand, a surface coated with polymers can introduce lens effect on the images. For these reasons we decided to work with through-holes (stencils) of micro-patterns on low autofluorescent substrate such as glass, or some polymers. Hawkins and Yager [47] showed that topas has a similar autofluorescent characteristics as glass. This not only improves the optical contrast for fluorescent microscopy, but also provides the possibility to use substrate specific chemistry to functionalize the bottom of micro-patterns and keep the rest of structure intact.

Microfabrication techniques
A wide variety of choices for microfabrication of stencils are available [42, 48, 49]. We looked for a technique that is easily achievable in a common chemistry lab with minimum extra infrastructure and maximum reproducibility. Making micro-array stencils with PDMS is possible, however, it requires complicated fabrication steps. RIE etching of PDMS, uses the photolithography techniques [50] to directly etch the pattern on the PDMS surface. Using a silicon wafer with the SU-8 patterns as a stamp requires high vacuum [51] or high pressure [52] to squeeze out PDMS from the substrate to form holes.

Micromolding in capillaries (MIMIC) uses the capillary forces to suck in the liquid in a structured PDMS stamp on the surface. A CH_4/He RF plasma surface treatment of PDMS

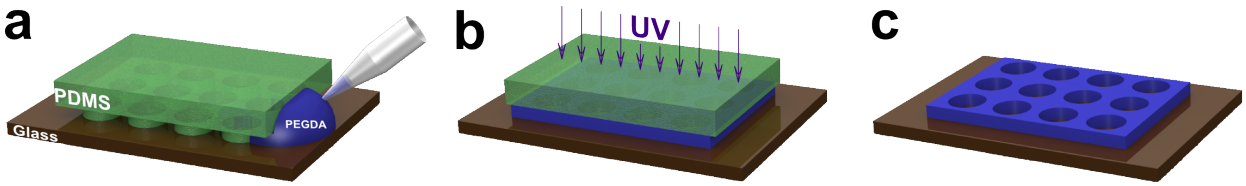

Figure 1.1: Micromolding in capillaries.
a) A drop of PEGDA is put on the side of stamp which goes inside the structures with the capillary forces. b) The sample is put under the UV light to cure PEGDA. c) The PDMS stamp is removed and the PEGDA structure is left on the substrate.

stamp is required to mold PDMS [53]. However, it was shown that PEGDA polymers do not adhere to the PDMS and can be mold using MIMIC. The MIMIC technique has initially proposed in Whitesides research group in 1995 [54, 29] and further developed to be used for PEGDA structures by other groups [37, 43]. In our lab, this technique was used [41] and its compatibility and long term stability for single cell studies was proven. As it is shown in Figure 1.1 a drop of PEGDA is put on the side of the PDMS stamp which is sucked in the structures with capillary forces. This PEGDA liquid is then cured under the UV light and form a solid polymer on the substrate.

From the aforementioned criteria in the beginning of this section, we concluded that PEGDA structures is good candidate: 1) It is biocompatible and stable under cell culture condition. 2) It has a strong bond to topas and covalently binds to silanized-glass. 3) MIMIC microfabrication can easily produce stencils from it. 4) The autofluorescent is similar to PDMS and the stencil eliminate the background signal inside the micro-wells.

1.1.2 Geometrical characteristics

The geometrical properties of micro-patterns, such as size and shape can have effect on cell properties. Kurt et al [21] showed that confining hematopoietic stem cells (HSCs) in adhesive micro-wells can affect their state. They showed that micro-wells with 15 µm (average cell diameter) has higher fraction of quiescent stem cells in comparison to larger micro-wells. On the other hand the micro-well diameter affect the distribution of single cell occupancy of patterns [55]. This suggests that there is an optimum in geometrical properties of micro-patterns for single cell studies. We have chosen three criteria for an optimum micro-well diameter and depth:

a) Cells must be viable for 3 days with the same average doubling time as bulk.
b) Once cells settled inside the micro-well, they should not be washed away with the flow of medium.
c) Maximum single cell occupancy.

To find the best dimension, we have examined diameter and depth of micro-wells experimentally and confirmed our findings with a simulation.

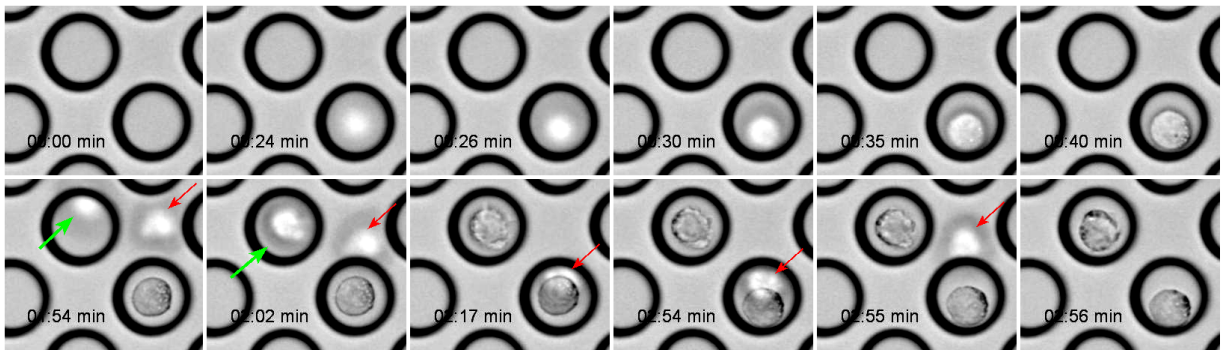

Figure 1.2: This time lapse shows a bright field image of cells settling down into a micro-well. The first pipetting put a single cell in the lower right well. The second row shows a second flushing of cells into the channel which adds a single cell to the neighboring well (green arrow) and an extra cell on top of first well (red arrow). This extra cell cannot settle completely into the well because of the micro-well diameter and is washed away in the consequent washing step.

Micro-well diameter optimization

We have tested a range of micro-well diameter (d_W= 20, 25, 30, 35, 50 µm) on murine erythroleukemia (MEL) cell-line with average diameter (d_C) of 20 µm. MEL cells were cultured on these patterns for three days. All the samples with $d_W > 1.5 \times d_C$ showed high viability without a change in average doubling time compare to bulk. To measure the maximum single cell occupancy we have counted the number of cell per well for each of the samples. For micro-wells with $d_W > 1.8 \times d_C$, the probability of double cell occupancy is increased. We have chosen micro-well diameters between $1.5 - 1.8 \times d_C$ for our studies.

Micro-well depth

Two depth of micro-patterns was tested: Shallow structures with 18 µm, and deep structures with 30 µm.

The shallow structure provide a pattered surface with can separate individual cells, however, flow of new medium can easily wash the cells aways, thus it is not possible to exchange medium or add additional components in the medium during the experiment.

The deep structures are able to keep the cells inside the micro-well even with the flow. The maximum possible flow-rate on the channels of micro-well were tested with a syringe pump. The cells will remain in micro-wells with the flow-rate of $<720 \mu m\, s^{-1}$. The maximum rate corresponds to complete exchange of medium inside the channel in 5 minutes. The deep micro-wells are also not too deep to accommodate a stack of two cells, and all the extra cells are washed away, see Figure 1.2.

To increase the level of micro-well occupancy further, we used a two-step protocol followed by several washing steps. The optimal diameter of micro-wells is beneficial in this approach. As it is shown in Figure 1.2, the initial cells sediment down into a single

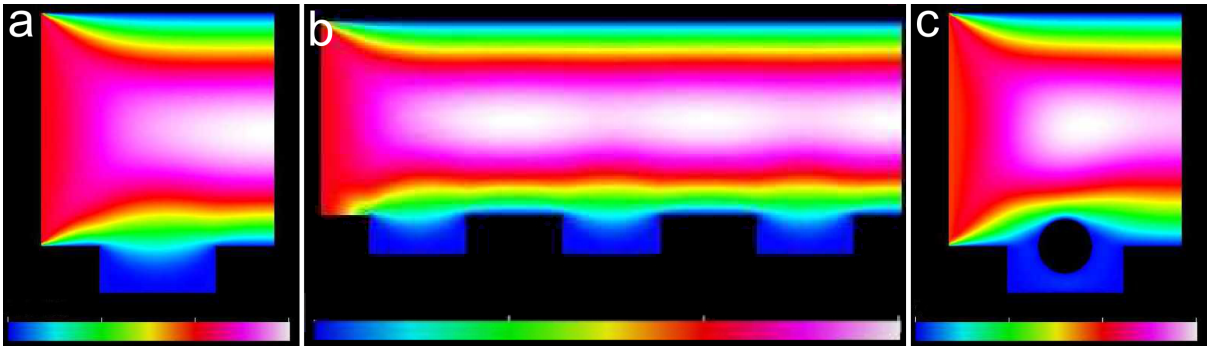

Figure 1.3: The 2D simulation of flow over micro-wells. The computational fluid dynamics (CFD) was done in Elmer FEM software calculating the flow trajectory and velocity on top of micro-wells. The color code is in arbitrary units to show the relative flow-rates. a) Flow velocity over single well; b) Flow over series of three wells; c) The cell is approximated as rigid body inside a single well.

well over few seconds. In following seeding steps, more single cells can settle into empty micro-wells. At the final steps the loose cells on top of the structures or in double occupied micro-wells are washed away.

2D simulation of flow

A 2D simulation of flow over a micro-well is performed to see the trajectory of flow on top and near the micro-well. The computational fluid dynamics (CFD) simulation is done in Elmer FEM (CSC - IT Centre for Science, Finland) software. The 2D model and finite element mesh is produced in Gmsh [56] and exported to Elmer FEM for CFD analysis. A constant inlet-outlet flow and no-slip walls have been used with transient analysis using Navier stokes equations. The complete set of parameters on the Elmer solver is reported in Appendix E. This set of simulation was only used to visualize the direction and relative speed of flow on top of the micro-wells, hence the cell is simplifies as a fixed solid body. Figure 1.3 shows the final results.

Our findings are in agreement with the previous simulations by Wang et al. [57]. They used ComSol® and concluded that this flow profile assures the placement of cells only inside the micro-well. They called this phenomenon a passive hydrodynamic docking of cells. In Figure 1.3.c we used a stationary object as a representative of cell, while this could be not completely describe the situation, however the similarity of our simulations with Wang et al. is assuring for our application purposes.

Maximum number of micro-wells in a single slide

The maximum coverage of substrate is an important factor to achieve highly parallel single cell acquisition. The hexagonal lattice provides the minimum space between circular objects, hence we chosen this lattice for the pattern of our micro-wells array. The unit-cell of a micro-well array are shown in Figure 1.4. Two shapes of micro-structures are

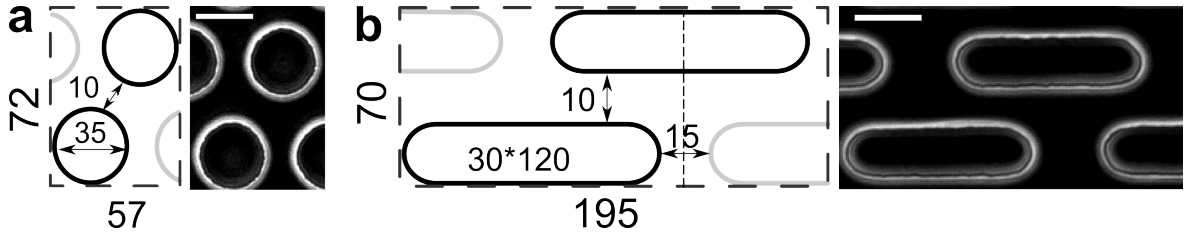

Figure 1.4: The dimensions of micro-array. The scale bar is 30 µm. a) Micro-wells with 35 µm diameter, b) Micro-slits with width of 30 µm.

designed and fabricated throughout this project: **micro-well**, the circular micro-patterns and **micro-slits**, the elongated slit patterns with the length four times the width. The optimal dimensions that are selected for final designs is shown in Figure 1.4.

We have already discussed the criteria for choosing the micro-well diameters. The 35 µm diameter of micro-well in Figure 1.4 is $1.5 \times D_c$ of the average stem cells' diameter used in chapter 2. Their average diameters were 20 µm. The final distances between the micro-patterns are defined by process constrains. The design and fabrication constrains are imposed by photolithography and softlithography limitations. We selected for the maximum resolutions at all the steps in fabrication.

We have used two methods for photolithography, UV-lithography and laser lithography. The mask for UV-lithography is a high-resolution printed transparency mask. The resolution of the printer in this case is 20 µm. The laser lithography is done by a ProtoLaser LDI device (LPKF Laser & Elektronika, Naklo, Slovenia), with a laser with 375 nm wavelength and 1 µm spot diameter. The dose tests on this method showed that a structures with minimum size of 10 µm can clearly be fabricated on a 30 µm thick resist.

The softlithography limits the aspect ratio of structures, e.g. well to well distance to depth, or well's diameter to depth. Very low aspect ratio can lead to pairing of pillars of PDMS after release from SU-8 structures. Delamarche et al.[58] showed that this ratio should stay between 0.2 to 2. This means that a the minimum distance should always be bigger than 6 µm for a 30 µm thick resist.

With aforementioned resolutions we concluded that the photolithography resolution with 10 µm minimum distance is the deciding factor for our design. The distances that are shown in the Figure 1.4 has been chosen for microfabrication. The experimental tests showed that with these parameters we get a reproducible PDMS and consequently PEGDA structures.

The reuse of PDMS stamps was also checked. We found out that the stamps for high aspect ratio structures (>35 µm micro-wells) can be used for up to 5 times. However, for smaller micro-wells (25 µm) the micro-pillar broke off after the 3rd use of the same stamp (see Appendix C). This can be explained with the fatigue forces which weakens of sample quite dramatically over several use because of possible micro-fractures. This was not considered in the study of Delamarche et al. [58]. It has been mentioned that PDMS has a low fatigue resistance [59] but finding the exact reason of failure need more micro

Pattern type: Array of	Dimension (µm)	Area p. pattern (µm^2)	Slide Type ibidi	# Patterns p. Channel	Cell Density #Cell mL^{-1} $\times 10^4$
micro-well	35	1370	I Leuer	$\approx$ 146000	48.6
			VI $^{0.4}$	$\approx$ 35000	14
Micro-slit	30 $\times$ 120	4550	I Leuer	$\approx$ 44000	14.6
			VI $^{0.4}$	$\approx$ 10500	4.2

Table 1.1: Number of micro-wells. The two microscopy slides from ibidi (ibidi GmbH, Germany) has either 1 channel (I Leuer) or 6 channels (VI).

mechanical investigation of PDMS which was out of the scope of this project.

Micro-patterned substrate on the ibidi sticky slides
As mentioned before the micro-patterned surface is mounted to an ibidi sticky slide (ibidi GmbH, Germany). The sticky slide VI has 6 individual channels each with 120 µl capacity on a standard microscopy slide (25 $\times$ 75 mm). This provides a versatile platform for a high throughput multi-variable (up to 6 variable) investigation per experiment. The one channels slide (I Leuer) has bigger growth surface and can house higher number of micro-wells per condition. Table 1.1 shows an overview of number of micro-wells per channel. The slides have defined growth area (0.6 cm^2 for 6 channels and 2.5 cm^2) out of which only $\sim$ 80% can be covered with micro-patterns. The whole area of microscope slide was imaged using a computer controlled automated x-y stage (Tango XY Stage, Märzhäuser). The microscope stage can raster scan 60-70 fields of views per minute which corresponds to 2 channels per minute.

1.2 Cell Culture conditions

For survival of cells *in vitro* it is required to provide *in vivo* like conditions. The blood-stream in the body provides nutrient and other metabolite to cells. The body also regulates and keeps the temperature constant at 37°C.

For our *in vitro* systems we have also designed the microscopy setup to provide the same conditions on the stage. Figure 1.5.a shows an overview of the experimental microscopy setup. A cell culture medium (RPMI 1640, lifetechnology, Germany) provides the nutrients which are necessary for the cells. This medium requires a 5% atmospheric pressure of CO_2 to balance the buffering condition [60] which is provided by a CO_2 mixer device (Brick, ibidi GmbH, Germany) to the observation chamber. The constant temperature is maintained in a temperature and humidity controlled chamber (Heating system, ibidi GmbH, Germany) on the microscope stage.

Despite above equipments, we have observed number of unexpected cell death in the *in vitro* culture on our slide. In order to assess the reasons for this problem, we performed an in depth investigation of the properties of samples and the incubator on the microscope.

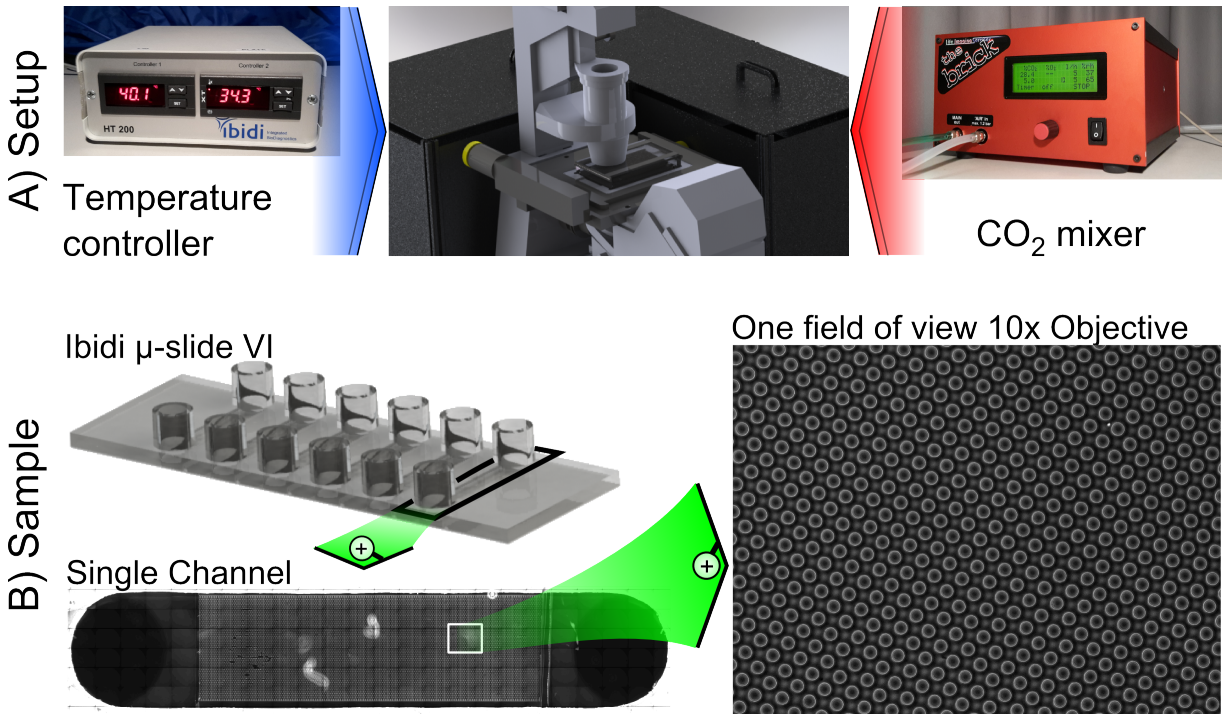

Figure 1.5: On stage live cell imaging setup.
A) The temperature of microscope stage and CO_2 concentration are kept constant with an ibidi heating system and CO_2 mixer. B) micro-well arrays are housed in an ibidi sticky slide VI. All the micro-wells in each of the channels is raster scanned over 5×14 fields of view of 10x objective. The number of micro-wells is mentioned in Table 1.1

We have checked three parameters that are essentials for cell growth: nutrient, temperature and CO_2 concentration.

Nutrient
Cells were viable on the slide inside the common cell culture incubator for at least 3 days. After that the test was stopped and a 90% viability of cells was confirmed with PI staining. This test confirmed that the medium provides enough nutrients for cell growth for the whole duration of experiment.

Temperature stability
The temperature of slide is controlled by ibidi heating system (ibidi GmbH, Germany). The heating chamber is design for the microscopy slides and provides a constant temperature for culture medium on the microscope. The plate warms the slide and keeps the temperature constant. The heated lid of chamber keeps a warm and humid environment around the slide while preventing the vapor condensation.

The temperatures of the controller was checked with an external thermometer as well as an infra-red camera. While the average temperature shown by thermometer and con-

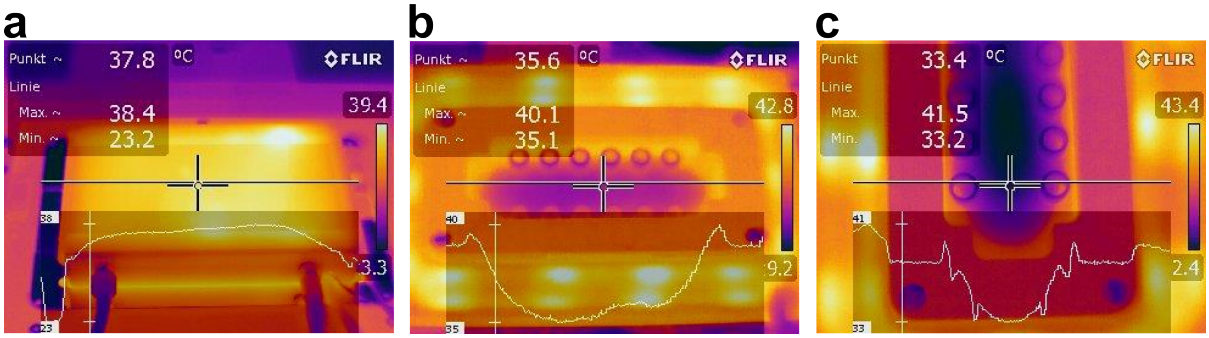

Figure 1.6: Infra red images of heating system showing the temperature gradient. Sample and stage was chalk sprayed to remove reflection effect in IR image. The temperature of the center pointer is given on top left value, the temperature profile of the line is also shown at the bottom of image. a) An overview image of the box with the lid on. b) Infra red image of 6 channel slide right after removal of the lid a slight temperature gradient $\sim$ 3 °C is observable here. c) Temperature gradient over the length of one channel . This image was taken several minutes after the removal of lid. The actual temperatures maybe higher with lower gradient (as visible in b).

troller agreed with each other, the IR images revealed some issues with the temperature distribution. There is a visible temperature gradient from the sides to the center of slides. This temperature difference is around 3°C which can affect temperature sensitive studies (see Figure 1.6).

If the low temperature caused the cell-death we expect to see a partial survival of the population on the area with 37°C. However, this phenomenon was not observed in experiments. We have applied some other measures, e.g. the control of room temperature, and minimized this gradient to 1-2°C, but it did not prevent the unspecific cell death in our time lapse movies.

The temperature may play a big role in more sensitive studies about the short term dynamics of cells and this gradient must be characterized. However, we concluded that it will not cause the cell death in the time-course that has been observed.

It is important to point out that Figure 1.6.a and .b was taken right after opening the lid of the chamber. Hence, they show a reliable value of absolute temperatures. In Figure 1.6.c the lid was removed several minutes before the image was taken. The sample cooled down because of surrounding low-temperature which resulted in a higher gradient. This also shows that it is important to keep the lid on at all time and keep the sample away from the extreme changes in temperature, as well as keeping the whole room at a moderate temperature. The warming elements of the heating system can equalize their temperature fast in response to the environmental changes. However, the temperature lost from the sample needs more time to equilibrate and may not be well maintained, as there is no active element on the sample to warm it up.

CO_2 concentration

Cells were grown in normal RPMI medium which requires 5% ambient CO_2 for buffer conditions. The exchange and consumption of nutrients in cells induce high pH fluctuation which is not healthy for the cells. In blood stream as well as several cell culture media, CO_2 in the form of bicarbonate (HCO_3-) in solution provides the buffer to conserve pH [61]. This concentration is provided by the CO_2 mixer (Brick, ibidi GmbH, Germany).

In order to test the CO_2 system, we have perform three types of experiment: using a CO_2 independent medium, increasing the CO_2 concentration in the chamber, and changing the substrate of structure.

The CO_2 independent medium is achieved by supplementing the RPMI medium with 1mM sodium-pyruvate [60]. An overnight experiment with CO_2 independent medium showed no sign of sudden death.

In second set of experiment we increased the concentration of CO_2 in chamber up to 10%. At this rate, the cell population in shallow micro-well arrays survived and proliferate for two days. However, with the same condition in deep micro-well arrays, cells started dying after 12 hours.

In the next test, the standard topas substrate of the μ-slides (ibidi, Germany) is substituted with a glass (D-263M Schott) substrate. In the same condition, e.g.10% CO_2, the cell population retain a normal proliferating behavior for two days in shallow as well as deep micro-well arrays.

We have investigated the exact cause of the problem with respect to CO_2 concentration. The detail information of topas substrates, indicated that this material is permeable to CO_2. The design of heating chamber is such that the substrate is in contact with the medium with high CO_2 concentration on one side and room air on the other side. The permeability results in an out-diffusion of the CO_2 from the bottom of micro-well which is faster than in-diffusion of CO_2 from the CO_2 containing chamber (see Figure 1.7). This is in agreement with the observation of viable cells in incubator, because there topas is in contact with 5% CO_2 atmosphere. This phenomenon also explains the reason that the glass substrate gave a better outcome.

We modeled the diffusion of CO_2 in the channels as a one dimensional diffusion inside the channel. The assumption is justified since the CO_2 is provided through a fixed concentration at the inlet on the surface cross-section of the channel and diffuses through the long channel in one direction. The Fick's second law of diffusion (Equation 1.1) gives an approximate on how long it takes for the CO_2 to diffuse through the whole channel. The solution of 1D Fick's law is given in Equation 1.2.

$$\frac{\partial y}{\partial x} = D\frac{\partial^2 y}{\partial^2 x} \tag{1.1}$$

$$c(x,t) = c_0\left[1 - \frac{x}{\sqrt{D\pi t}}\right] \tag{1.2}$$

The diffusion of CO_2 in water at 37°C is 2.4 $cm^2\,s^{-1}$ [62]. If the atmospheric concentration is 5%, it takes 2:30 minutes to reach a same level of CO_2 at a distance of 1mm

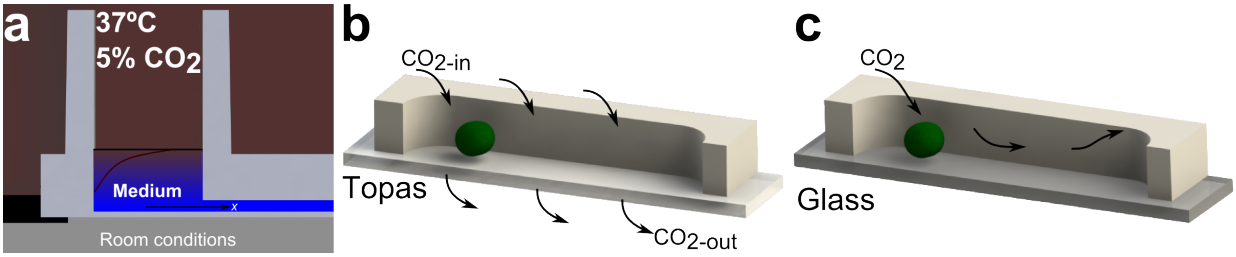

Figure 1.7: The diffusion of 5% concentration of CO_2 into the medium. a) Schematic of the condition at the interface of gas and medium at the inlet of channels. The diffusion condition for micro-patterned surfaces of CO_2 permeable topas (b) and impermeable glass (c) substrate.

inside the channel. Similarly, it takes 3 hours to have a same condition at the center of the channel (9 mm). To get the 5% concentration in the center of channel, having a 10% atmospheric conditions reduces the time 4 folds, meaning it reaches the desirable concentration within 50 mins. The diffusion behavior can well explain the behavior we observed in our experiments. In the absence of out-diffusion, i.e. glass substrate, 10% atmospheric concentration assure the enough diffusion speed for soluble CO_2 to keep the buffer condition over the whole channel within 50 mins. and preventing the build up of pH over time.

1.2.1 Cell density

The cells were seeded by pipetting the culture medium on top of the micro-well arrays. Therefore, they are randomly distributed in the available micro-wells due to sedimentation. The "filling factor" is the number of cells per micro-well. The filling factor is defined to quantify the cell occupancy of micro-wells and its value depends on the cell density and geometrical parameters. As explained in subsection 1.1.2, for deep micro-wells the density is irrelevant while only filling factor 1 is possible and the rest of the cells can be washed away (look at Figure 1.2). The best approach is to overfill the whole sample with the number of cells 3 times the number of available wells.

For shallow micro-wells and micro-slits, only the initial seeding defines the random distribution of sedimented cells. Therefore, the cell density is an important factor. We have tested several cell density on these micro-patterns and counted the wells with filling factor one. A distribution of around 30-40% of occupied micro-patterns proved to have the highest filling factor 1. The number of cells must be 40% the number of available micro-wells, the corresponding cell density is listed in Table 1.1.

Incidentally, the number of cells required for I-Leuer slides (ibidi GmbH, Germany) is equal to the limits of harvested progenitor cells from a single mouse, which is close to 40000 cells (see chapter 2).

1.2.2 Surface treatment

The properties of the surface of microfluidic device can have an effect on the natural state of cells. It can induce some artificial *in vitro* stress on the cells that they would not have in their natural *in vivo* state. The bio-compatibility of our substrate and microfluidics materials are well-established [63]. However, in microfabrication process, each step can potentially change the surface properties. These properties can be either mechanical (e.g. roughness, softness, elasticity module) or chemical (e.g. oxidation, activation of surface molecules). Hence, it is necessary to perform a viability test with the new structures or when there is a change in the protocol.

In the majority of available microfabrication protocols, oxygen plasma is used to activate the surface and make it hydrophilic. While this is proved useful in fabrication steps, one has to take into account that oxygen plasma also leaves free radicals on the surface of the substrate. The reactive oxygen residue induces cell apoptosis [64, 65]. We have observed the same phenomenon when introduced a short (10 sec) oxygen plasma, to increase the wetting speed, before adding the medium and cells. This resulted in a rapid cell death just after two hours from seeding the cells. The problems was resolved when the samples were kept under the medium for two days before seeding the cells. This neutralizes the oxygen radicals on the surface.

To remove this adverse effects, we substituted the plasma steps in protocol with other treatments. The plasma with a neutral gas, e.g. Argon [66], was used to increase the hydrophilicity of the surface. The plasma cleaning steps were also replaced by the sonication of samples in ethanol and water. In order to expel the air bubbles from micro-wells we added a sonication under the medium. Sonication results in the breaking of the surface tension at water/air boundary in micro-patterns and removing the air bubbles from the patterns.

1.3 Time lapse single cell screening

The cell development and their response to external stimuli is a gradual process which ultimately decides the fate of a population. In stem cells, external chemical and physical signals drive them to the differentiation point and development to specialized cells. For the tumorous cell, the internal and external conditions affect their response to the drugs and radiation therapy. While the end point single cell studies (such as FACS) reveal the outcome of the signal. The underlying processes cannot be explained with this method. Different temporal dynamics at the single cell level can lead to a similar outcome at the end point studies [67]. The dynamic response of cells which guide them to their fate plays an important role in understanding the internal decision making machinery of cells.

Recent technological advances in microfluidic and microscopy systems provided the possibilities to cultivate, label, and follow live cells *in vivo* and *in vitro* . The *in vitro* observation of live cells with time lapse microscopy can resolve some of the underlying mechanism of single cell decision making. The main parameter of time lapse study is the

time-interval. While high frequency gives more detail on cell behavior, it may also adversely influence the cell behavior, so the time-interval has to be chosen according to two main factors: a) Phototoxicity b) Average time course of investigated biological system.

Phototoxicity in fluorescent microscopy is the effect of intense light on the molecular machinery of cells which could be fatal for such cells. It is a crucial point in data acquisition to prevent unwanted alteration of cell behavior [68, 69]. Phototoxicity is mainly due to induction of reactive oxygen species [65] or other types of free radicals [70] in the cells, hence activating the apoptosis pathways of the cells and killing them. To minimize this effect the dose of light shined at the cell should be minimized, which means the time interval, lamp intensity, and exposure time has to be adjusted.

Long time-interval can potentially mask the underlying dynamics of a biological process. The chosen time-interval have to be lower that the expected time course of the reactions in the system under investigation.

The brightfield imaging operates with a low intensity light which reduces the phototoxicity risks dramatically. Therefore, it is a better candidate for short time-interval experiments. We have employed phase-contrast, brightfield microscopy technique for motion tracking to keep the cell identity throughout the time lapse experiment; details are explained in section 1.4.2. The high-intensity fluorescent images were limited to the maximum possible intervals to still be able to deduce the dynamic properties of the processes under investigation.

1.4 Image processing

The data acquired with time lapse studies quickly reach hundreds of gigabyte. On the one hand, we must make sure that enough acquisition points are present to resolve the underlying dynamics. On the other hand, we should prevent the high acquisition frequency which leads to a bulk mass of unnecessary data, or as discussed, phototoxicity. In both cases, the manual analysis of images is out of question. To achieve these goals, we have considered a "smart acquisition" technique. This method tailors the microscopy imaging toward an goal specific acquisition which reduces the image processing costs at the next step. Furthermore, it aims for a simplified, parallelized, and categorized sets of acquired data which reduces the complexity of detection algorithms. One of these approaches for simplifies cell tracking is out-of-focus brightfield microscopy.

1.4.1 Out-of-focus brightfield microscopy

We took brightfield and phase-contrast images of our samples and checked them with several detection algorithms. The simplest and computationally cost effective algorithm for image segmentation is thresholding analysis. Hence in the first step of design for "smart acquisition", we have checked several techniques to find the images that can be segmented fastest using thresholding algorithm. We have tested different focal planes, as Buggenthin et al. [11] has also suggested, for an optimum blurriness in an image to increase the

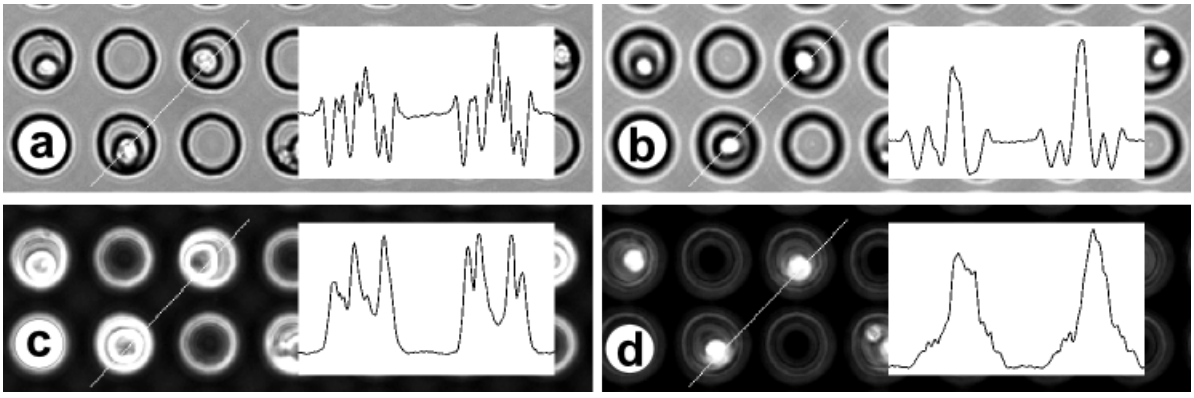

Figure 1.8: The contrast difference in transmission microscopy images for Brightfield (a,b) and Phase-contrasts (c,d) microscopy. The out-of-focus images (b,d) as oppose to in-focus images (a,c) show a nice characteristic intensity profile for threshold detection algorithm.

contrast between cells and surrounding. We have tested 9 focal planes over 9µm shift with sharp-focus being in the middle point. We have concluded that both in phase-contrast and brightfield images, a focal point with a distance of less than average cell-diameter (here 20µm) results in high contrast images. A cell in the out-of-focus phase-contrast image is represented by a bright-spot in black background which can easily be segmented and tracked over-time, while in brightfield this contrast is lower and with a gray background. Figure 1.8 shows the in-focus and out-of-focus images of cells in corresponding structures, the top images are from brightfield and the bottom ones from phase-contrast microscopy.

Cells change positions dramatically at the division point, making the difference between frames of phase-contrast image large. Hence, we have only used phase contrast in micro-well arrays (in chapter 2), where we follow each cell only up to division point. The tree of cell family in micro-slit (in chapter 3) was obtained using more complex algorithms on a low-contrast out-of-focus brightfield image which is less susceptible to large variation of cell motion at division point. In both cases a focused image is captured for morphological inspections.

1.4.2 Software: MicroWell Analysis

The efficient analysis of data plays a pivotal role in high throughput single cell research. The image processing steps to produce the analytical data from the raw images constitute the major computationally intensive part of analysis. We used the popular open source image processing software ImageJ [71] as the base for our image processing and benefited both from the large sum of available plug-ins as well as the possibility to develop a new plug-in based on Java.

The work flow of our image analysis is shown in Figure 1.9. The preprocessing of images are done to remove the experimental artifacts from the stack of microscopy images. The motorized stage is used in scanning mode to cover big sample area over several fields of

view simultaneously. However, the repositioning at each time-point had one to two µm precision. The image stabilizer plug-in [72] is designed to align images based on the fixed features over the stack. In our images the micro-patterns are the fixed features which are aligned through an x-y transformation. This transformation also decouples the random error from the repositioning of stage from the Brownian motion of the cells inside the micro-wells.

The mercury lamp can have a slightly fluctuating intensity during 2 to 3 days experiment. We have used "Correct Bleach" plug-in [73] to normalize the average background values through all the frames of time lapse movie. This plug-in was used on brightfield images as well as for qualitative inspection of fluorescent data. For quantitative analysis of onset of fluorescent signals, a background correction algorithms based on the micro-patterned structures was used.

We have developed an in-house, Java-based plug-in called MicroWell analysis (MWA). After the preprocessing, the stack of images was imported to MWA. The plug-in is modularized into three steps: identification of micro-patterns, selection of regions of interests, and tracking of the cells. The first module identifies and locates the position and orientation of the micro-patterns. A preset values for shape and size of patterns ensures is given to increase the recognition algorithm. The patterned structures are then subtracted from the images to keep the focus of following steps of image analysis only on a smaller area with the cells to detect. In the second module, MWA automatically select the occupied micro-wells and awaits the user input for correction of this selection. A manual verification of automatic detection confirmed an 80% accuracy which suggests that in further development this step can also be done without user supervision.

Once the selection is finalized, MWA tracks center of all cells through the time lapse frame, simultaneously. The out-of-focus acquisition was designed to minimize the computational cost of this step. As the final check-point for image processing, the detected trajectory was overlaid on the original movie and a manual inspection can be performed. The output of MWA is a structures raw datafile which include the position of center of each cell and its corresponding micro-well.

The raw trajectory datafile, was imported into a customized MATLAB module for further analysis. The MATLAB module contains several m-files to calculate and extract the desired characteristics of single cells' trajectory. The details required defers for each set of experiment. The extracted properties of cells includes mean square displacement, cusum, onset of adherence, onset of fluorescence, and ....

The final output of MATLAB module is database file which contains all the informations about an individual cell, such as the micro-well number, time-point, position of the center, and .... The databased can then be imported to the desired data-presenting software, i.e. Excel® or OriginPro®, for presentation or possible statistical analysis.

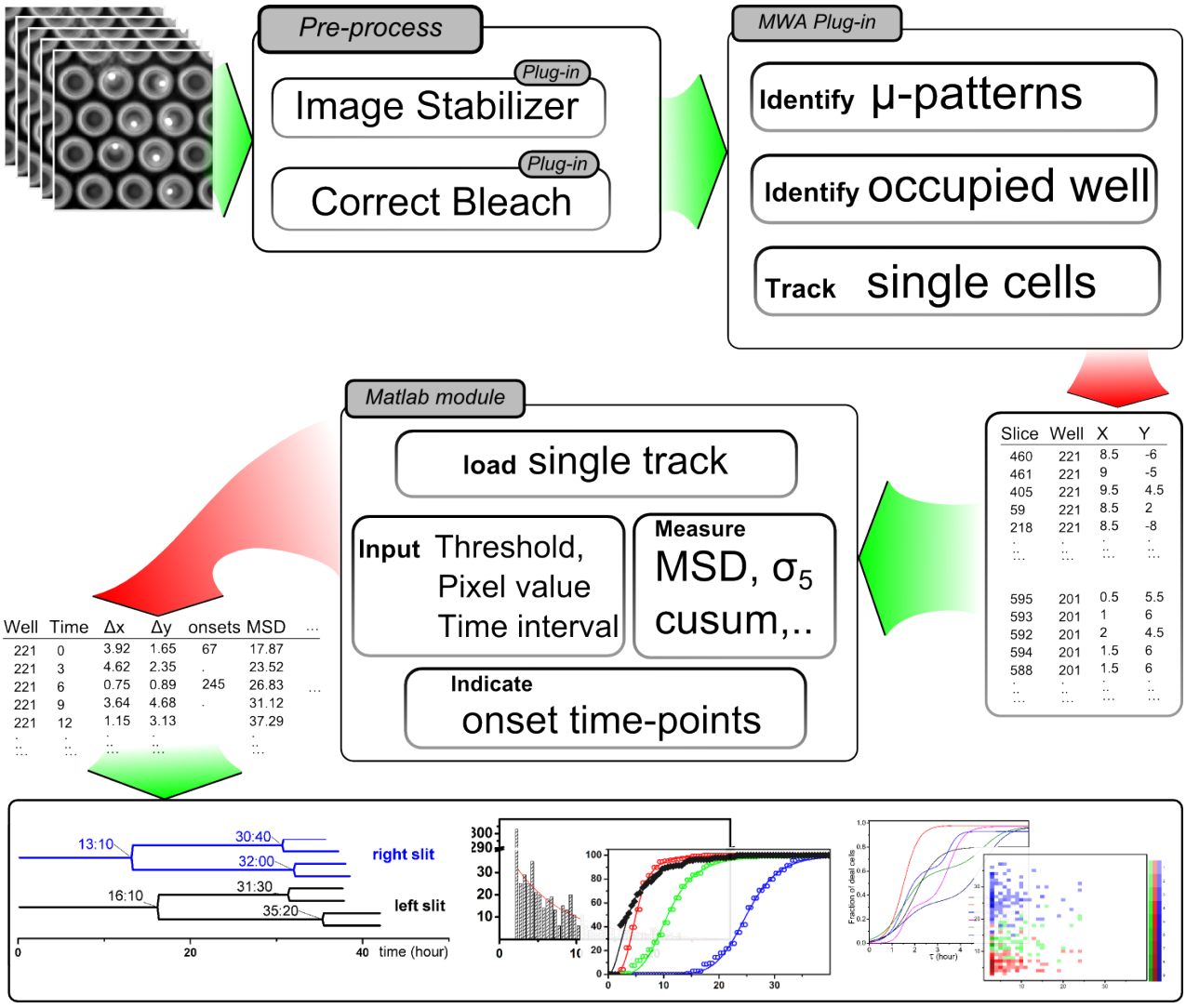

Figure 1.9: Work-flow of image analysis module.
Pre-process: include ImageJ plug-ins called Image Stabilizer [72] and Correct Bleach[73].
MicroWell Analysis (MWA) is our in-house plug-in which is designed to detect and track single cells and gives the trajectories as an output for MATLAB.
Matlab module is a set of m-files which is written to read and extract the relevant properties from the single cell tracks and finally analyze the single cell dynamics. The output is specific for each project.

Chapter 2

The dynamics of progenitor commitment: a Label-free technique*

Differentiation of stem cells is a well controlled fate decision of cells which is highly regulated and maintained. Time lapse single cell microscopy offers platforms and methods to investigate the development of cells [75]. The micro-well array that we have developed is a powerful platform for parallel observation of single cell events. In this chapter we investigate the dynamics of differentiation of granulocyte macrophage progenitors (GMP) to the macrophage lineage.

The first section is the introduction to stem cells, their developmental tree, and the common differentiation detection technique. Furthermore, we discuss the obstacles of fluorescent microscopy in primary cells, and the need for a label free detection method for differentiation. It is known that macrophages adhere to tissue culture plastic plastic (TCP) substrate while their progenitors do not. In our micro-well array we tracks the Brownian motion of single progenitor cells and report their transition to adherent mode as the differentiation marker.

2.1 Stem cells: development and application

A Stem cell is a cell at early stages of body development which divides and gives rise to all types of specialized cells in a body. Stem cell notion is commonly used for whole family of cells with a potential to give rise to two or more specialized cells. Moreover, based on their capabilities they are divided into three categories: totipotent, pluripotent, and multipotent cells. Totipotent stem cells are the ones that differentiate to all types of cells. Pluripotent cells are specific to part of body (Endoderm, Mesoderm, or Ectoderm), while multipotents only give rise to some types of cells within the organ. The intermediate cell types are also known as progenitors or precursors.

*Part of this chapter and figures are adopted from Sekhavati et al. [74] with permission of The Royal Society of Chemistry.

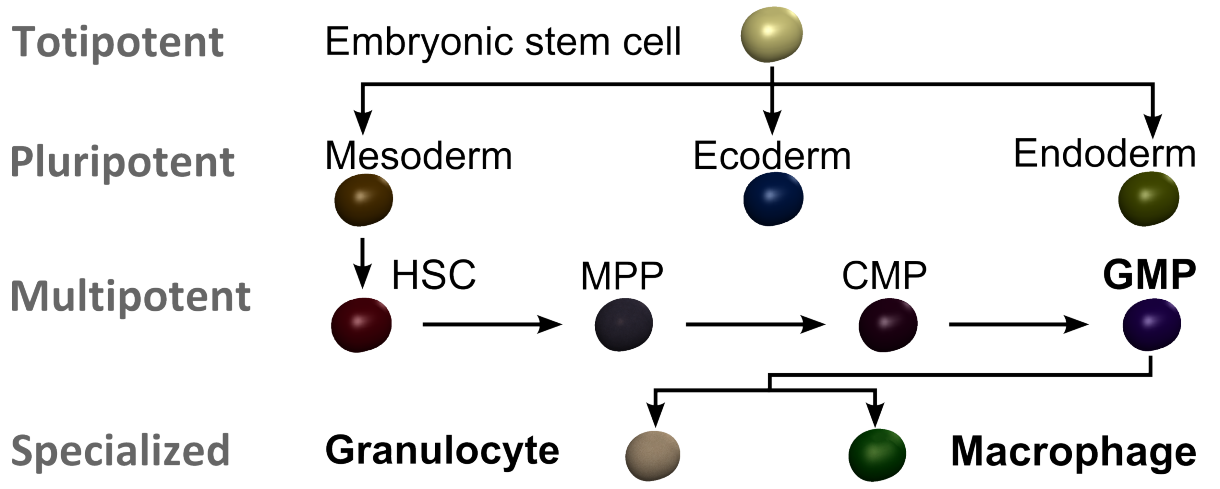

Figure 2.1: The tree shows the main players of stem cell development in HSC branch up to specialized macrophage or granulocyte cells. The titles in left describe the classes of stem cell.

Stem cells are present not only in early development of embryo but also in adult body. During the development, a population of cells stay in the potent stage and become adult stem cells. Adult stem cells can proliferate without differentiating for a long period (long-term self renewal) and when necessary give rise to mature cell types. The specialized cells are identified with their characteristic shape, morphology, and functions.

Figure 2.1 shows an abstract version of stem cell tree with a focus on hematopoietic stem cells (HSC) branch. Hematopoietic stem cells give rise to the lymphoid and Myeloid cells that build up blood systems, such as red, white blood cells, natural killer cells, and B-cells. The biological system that we are investigating in this chapter are types of specialized white blood cells called macrophages. Macrophages are derived from a bipotent cell called granulocyte-macrophage-progenitor (GMP).

The discovery of adult stem cells opened the opportunity for the regenerative medicine. It is the branch of medicine which explores the possibilities to restore the functionality of an organ using the regenerative capability of stem cells of the same person. For example, bone marrow transplant for leukemia treatment substitutes the damaged marrow with a healthy adult HSCs either from the same patient (autologous) or of a donor (allogeneic) [76]. The new HSCs in transplanted bone narrow regenerate and restore the normal functionality of the whole "blood" organ. The stem cell therapy could also lead to the cure for neuro-degenerative diseases such as Alzheimer.

Takahashi and Yamanaka showed [77] that adult stem cells can be re-programmed to become induced pluripotent stem (iPS) cells. This broadens the possibilities of stem cell regenerative properties from a single organ to cross-organs [78].

Any progenitor of a developed cell needs the correct set of conditions and stimuli to commit to one lineage. The key to applying stem cells as regenerative medicine is to understand and control the dynamics of stem cells commitment into specialized cells.

Stem cell development
Differentiation, the commitment of a stem cell to a specialized cell, is a gradual change in gene activation/deactivation leading to variation in the composition of the proteins in a cell and ultimately a new cell type. It is possible to identify some distinct intermediate progenitors based on their morphological and functional characteristics. However, the changes can happen within one or over few generations. On one hand, the time course resolution is not always achievable in population and end-point studies such as FACS, MACS or population gene-sequencing. On the other hand, a population change can result from a single stochastic event in a homogeneous population which is amplified through the intra cellular signaling and leads to a quorum decision for commitment to a specific lineage. A high local and temporal resolution is required to investigate these effects.

Single cell time lapse studies provide the tools to investigate stem cell differentiation [79, 22] and statistical analysis of heterogeneous population provides the models to understand the single cell decision making processes [80]. The time lapse study shines light on underlying mechanism of cell differentiation and the molecular pathways for commitment of a progenitors.

Stem cell differentiation detection techniques
A range of detection techniques for single cell studies of stem cells has been proposed recently, e.g. fluorescent microscopy, or impedance sensing [13]. The common way to identify stem cells and isolate them from a tissue is to use FACS. It uses a detailed information about the cell and sorts them based on the defined markers of stem cells. This markers has been identified for a large part of stem cell family, for example hematopoietic stem cells are selected for $CD34^{+}Thy1^{+}Lin^{-/low}$ [81]. The live cell studies, such as fluorescent microscopy, additionally require a complex preparation steps for a suitable mouse models with the tagged genes. It is desired to have a simpler detection methods with the same properties as fluorescent microscopy.

Here, we proposed a new technique which the difference in the physical motion of non-adherent versus adherent cells to identify the presence or absence of the family of surface proteins. This preserve the advantages of live microscopy, such as time resolution, and eliminate the need for the model mice, which is a complicated and time-consuming step. In the next section we lay out the concepts of our new method.

2.2 Brownian motion for differentiation detection

The motion of a particle is a physical property which is a result of its interaction with the surrounding. This motion can be characterized as diffusive, directional, constraint, ballistic, etc. A living micro-organism can have a random or driven motion. Driven motion is any active directional movement toward a beneficial condition, e.g. chemotaxis in a gradient of nutrient, or moving to a protein coated part of a substrate [82]. In the absence of gradient forces or active motion, cells exhibit a random walk. While adherent cells walk

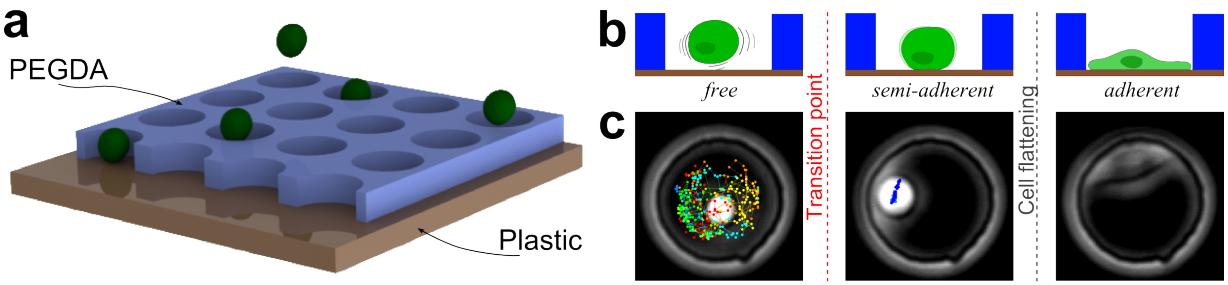

Figure 2.2: Single cell Brownian motion trajectories.
a) Schematic view of cells settling into micro-well arrays under gravity. b) Side view schematic depiction of the three states of adherence: freely mobile, semi-adherent and adherent. c) Corresponding phase-contrast image of a non-adherent GMP which differentiates into an adherent macrophage. The dots indicate the position of the center of cell over a period of 24 h. Elapsed time is coded in color from red to blue.

actively with their cytoskeleton and extra cellular matrices (ECMs), non-adherent cells float freely in the medium.

The characteristics of the motion of the cell can be used as the indicator of their response to the environmental stimuli. Stem cell differentiation results in up-regulation of some proteins which can include membrane proteins responsible to surface adherence. The GMP to macrophage differentiation is one of the instance that this happens. The up-regulation of adherence proteins on the cell surface is used as an indicator of differentiation event. Time lapse microscopy resolves the transition from non-adherent to adherent cells without any fluorescent markers.

Figure 2.2 shows the overview of experimental plan for label free differentiation detection. The population of GMP cells are initially pipetted on the micro-well array substrate as is shown in Figure 2.2.a and settle down individually in separate micro-well with the gravitational forces. Non-adherent GMPs can freely move inside the micro-well. Upon differentiation they adhere to the substrate, but keep their spherical shape, this is called semi-adherent stage (Figure 2.2.b,.c). When the cell is fully developed to macrophage, they flatten on the substrate and start their active motion, adherent stage in Figure 2.2.b.c. The center of cell is automatically tracked over-time and is indicated as the colored dots in Figure 2.2.c, the color code indicates the time going from red to blue.

Considering the limitations of microscopy system and average distance a Brownian particle can travel, we optimized the time-interval of imaging. The parallel data acquisition is then possible by probing the sample with automated microscopy stage.

2.2.1 Mean square displacement

MSD represents the extent of random motion in space, which is commonly used for characterization of the motion of a particle, e.g. diffusive motion, biased diffusive motion, and

confined motion [83]. Diffusion on a surface is modeled as a 2D diffusion of a particle with a slip boundary condition [84]. MSD is analytically derived from probability density function of particles [85]. Experimentally, MSD is directly calculated from the x and y positions of a particle at discrete time-points. If $r_i = r(t_i)$ and Δt is the acquisition interval, the displacement after m time interval is:

$$\Delta r_i(m\Delta t) = |r_{i+m}\vec{} - \vec{r_i}|$$

Where the mean square displacement at each time interval is calculated as:

$$MSD(t_m) \equiv \langle (\Delta r(m\Delta t))^2 \rangle = \frac{1}{n}\sum_{i=1}^{n} \Delta r_i^2(m\Delta t) \tag{2.1}$$

The analytical expression of MSD, on the other hand, is deduced for a specific boundary condition for the particle. Bickel [85] calculated the exact form of 2D diffusion of a Brownian particle in a circular confinement with reflective walls:

$$MSD(t) \equiv \left\langle |\vec{r}|^2 \right\rangle (t) = \frac{L^2}{4}\left\{1 - 8\sum_{m=1}^{\infty} \frac{1}{\alpha_{1m}^2\left(\alpha_{1m}^2 - 1\right)} exp\left(-4\alpha_{1m}^2 \frac{Dt}{L^2}\right)\right\} \tag{2.2}$$

where D is the free diffusion coefficient, α_{nm} is the mth root of Bessel prime function ($J_n'(\alpha_{nm}) = 0$), and L is the maximum distance available for free motion. The available space is defined as $L = d_W - d_C$. Where d_W is the average micro-well diameter and d_C is the average cell diameter. A particle in confinement does not feel the constrains at the short time-scale leading to a free diffusion behavior. When the particle reaches the confining walls at long time-scale, the MSD plot reaches a plateau value, which for 2D motion is equal to $L^2/4$, i.e. Equation 2.2 when $t \to \infty$.

The plot of MSD function gives us two valuable informations, 1) it shows that the motion of cells is indeed a 2D diffusion with a diffusion constant in the expected range, and 2) it gives a value for effective diameter of the non-adherent cells.

We have compared this value to the value extracted from microscopy image of the cell. As it is shown in Figure 2.3 the two values correlate very nicely. The smaller estimation of diameter in microscopy image can be explained by the artifacts that the out-of-focus (blurred) imaging induces on the diameter of the cell.

Assuming the cells as spherical object with average diameter of d=16µm in medium ($\eta = 0.72mPa.s$), the Einstein relation for free diffusion (Equation 2.3) at 37°C leads to free diffusion coefficient of $D = 0.04$ µm^2 s^{-1}.

$$D = \frac{K_B T}{6\pi\eta r} \tag{2.3}$$

A complete scan of microscopy-slide takes 3 minutes. Using Equation 2.2, it corresponds to an average displacement of 3 µm (5 pixels) for cells which can easily be resolved and tracked in microscopy imaging.

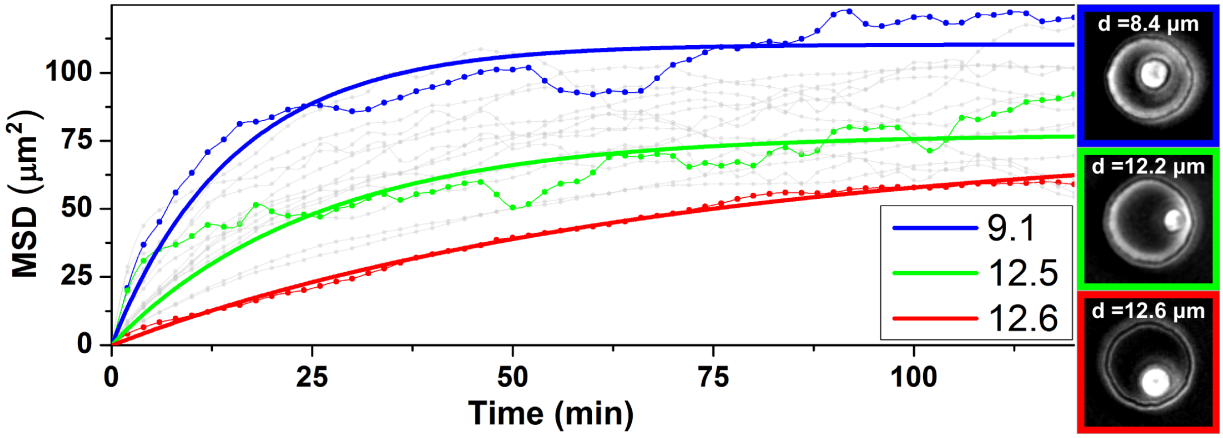

Figure 2.3: Mean square displacement.
Dots are experimental points and the three solid line shows the fit from the theoretical expression. The plateau values reflect the cell diameter. The corresponding phase contrast images of cells for colored solid lines are shown. Diameter calculated from fitted curves are shown in the inset and the diameter calculated from image calibration is shown on the corresponding image

2.2.2 Transition point detection

As we mentioned, the characteristic of the motion of GMP cells varies during their differentiation to macrophages. The commitment to a specialized cell line, i.e. macrophage, changes the course of motion from a confined random particle to a bounded particle. This regime change reflects in the trajectory of individual cells. The displacement of an unbound cell reduces or disappears after the transition to adherent stage. To detect this transition we used two algorithms. First was using a threshold value on the standard deviation of cell motion. Second was applying CUSUM on the displacement trajectory and detect the change point. Figure 2.4 shows a exemplary trajectory of transition of single non-adherent GMP cell to an adherent macrophage.

Local standard deviation of displacement.
The displacement-time graph of a single cell is a noisy random variable as a result either image processing errors or sudden large motion in a cell. Figure 2.4.a shows a single displacement trajectory. In order to analyze this trajectory, we calculated the dispersion of displacement in short temporal window. Local standard deviation (σ_t) measure the local dispersion of t points after each data point, which is calculated as shown in Equation 2.4

$$\sigma_t = \sqrt{\frac{1}{t-1}\sum_{N}^{N+t}(\Delta R_i - \overline{\Delta R}_t)^2} \tag{2.4}$$

We selected local standard deviation over 5 frame, σ_5, for our analysis. A threshold value was set below which the cell is assumed to be adherent. If a cell any apparent motion

for a short period of time, i.e. comes back to the same position after each time-interval, a false positive signal can be reported by the thresholding approach. Therefore, we defined a "consistency" parameter which checks the following values after each transition detection. If there is no cross over to the higher value over the consistency period, the cell has indeed adhered to the substrate at the detected transition point. The consistency parameter is initially set to 5 and increases until only one transition point in detected by the program. Figure 2.4.b shows σ_5 plot where the threshold values is the blue line and the detected transition point is marked with the red circle. We used the second algorithm to confirm the detected transition point called CUSUM .

Cumulative sum

CUSUM is the sum of the difference of each data value from a defined target value. It was first introduced by Page in 1947 [86] and ever since, has been used in variety of fields from market response to health care [87]. When there is only random deviation from the target value, CUSUM is around zero, but once there is a consistent deviation from the target, the CUSUM value will progressively deviate from zero at a finite slope. In our experimental setup the target value varies for each cell, therefore we chose the total time-average of displacement ($\overline{\Delta R}$) as the target value. The value of CUSUM at any step is calculated as in Equation 2.5, for convenience the CUSUM is calculated from end to start.

$$\text{CUSUM}_i = (\overline{\Delta R} - \Delta R) + \text{CUSUM}_{i-1} \tag{2.5}$$

The changes in motion regime in a CUSUM graph can be detected by locating the change in slope. The highest change in slope is expected to be the transition point. Figure 2.4.c shows the corresponding CUSUM graph of the trajectory. The blue lines are locally fitted lines to the graph which enables the automatic detection of slopes. The detected transition point is marked with the red circle. In our analysis, where there is a discrepancy between the transition point detected by σ_5 and CUSUM methods, the final decision was made manually by the user.

The CUSUM algorithm can also be used as an online detection method. The online detection for time lapse studies can be useful in cases that we are able to integrate analysis and data acquisition together. This could be used for example when the fluorescent signal is only needed after the adhesion has occurred.

2.3 Heterogeneity in differentiation

Differentiation of GMPs showed stochastic dynamics [88, 23]. With the help of micro-well arrays we were able to capture and analyze the behavior of many cells in parallel. The trajectory of 789 single cells was detected and the transition point was automatically extracted from them. The exact detail and growth condition of primary cells have already been described [23, 74]. Figure 2.5.a shows the distribution of single cell adherence event per half-an-hour in the time lapse experiment for 30 hours. Transportation of sample,

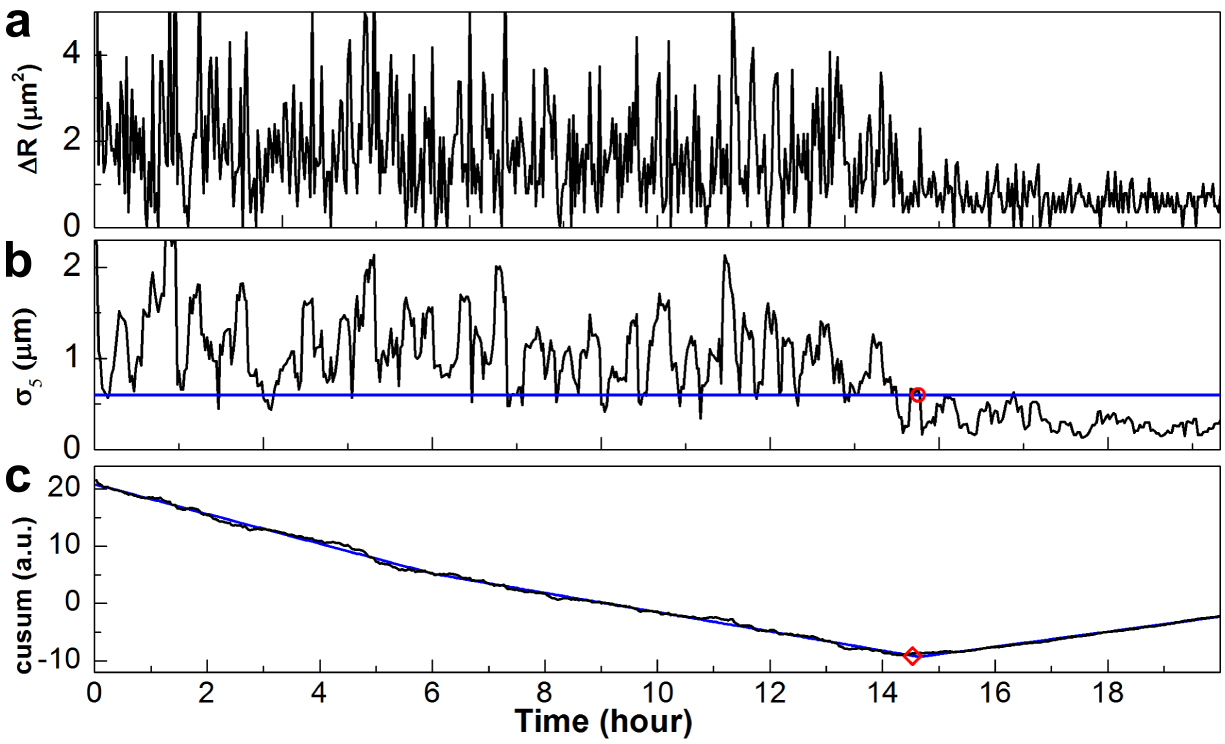

Figure 2.4: Transition point detection.
a) Displacement ΔR of a single cell in each time interval is plotted over time. b) Time course of the local standard deviation over a rolling time window of 5 frames, σ_5. The transition of GMP to macrophage is marked with a red circle, the blue line shows the threshold value. c) CUSUM value for the same track. The transition point is identified by the change in slope of CUSUM (red circle). The blue lines are the fitted lines for automatic detection of slope change

adjustment of focus of ∼100 fields of view on the microscope, and the adjustment of fluorescent acquisition settings takes around 4 hours. Therefore, monitoring began 4 hours after addition of M-CSF cytokine to the progenitors. Around 40% of cells showed adherent trajectory by the start of imaging. The number of adherence events then drops exponentially with time, and 80% of the cells have adhered to the substrate prior to the first division.

The time course of differentiation was investigated via the onset of expression of the EGFP-tagged Lyzosome2 (Lyz2) signal as well as the presence of MacI and F4/80 antibody markers. The Lyzosome2 protein is up-regulated when GMPs commit to a lineage either M or G (see Figure 2.1, Appendix A). The F4/80 and MacI markers are surface proteins and distinct indicators of macrophage lineage. Fluorescent images were analyzed by setting fluorescence thresholds for each marker and counting of the number of MacI and F4/80 positive and Lyz2-GFP expressing cells respectively. Figure 2.5.b shows the percentage of adherent cells (black), together with the time course of MacI positive (red), Lyz2-expressing

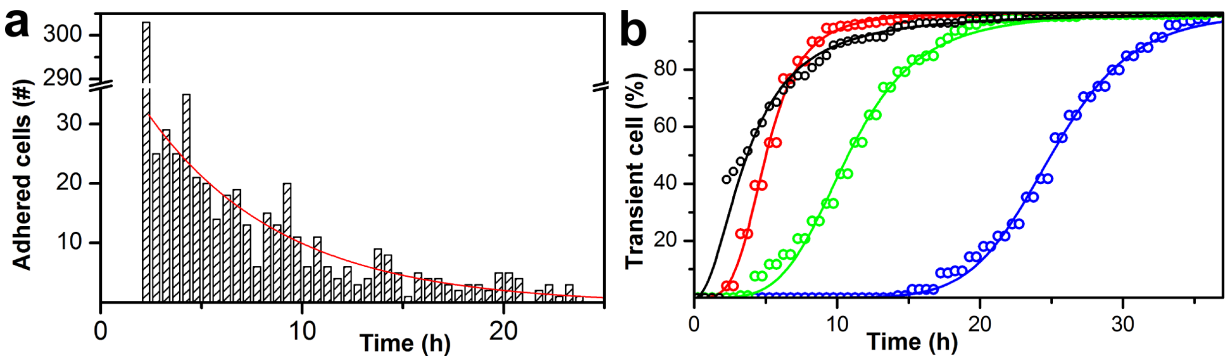

Figure 2.5: Distribution of adherence event.
a) Histogram of the number of adherence transitions in the time course of GMPs differentiation into macrophages (data are from 789 single cells), red line shows a first order exponential fit to the data. b) Percent of cells that adhered (black) and percent of cells that exhibited MacI (red), LzyM (green), and F4/80 (blue) fluorescent signal versus time.

(green), and F4/80 positive (blue) cells over a period of 48 hours.

The time course of the onset of fluorescent signals are in agreement with the literature [23]. The adherence transition shown to happen mainly after the MacI onset and before the onset of the other two markers. The kinetics of the increase of total adherence, however, is weaker than the steep increase of MacI expression. For this reason we calculated the single cell correlations in more details with time correlations between the markers.

2.4 Time Correlation

The correlation of onset time of up-regulation of proteins opens a window into the dynamics of molecular pathways and their interconnections. Combining three fluorescent channels and the label-free adherence detection, we were able to correlate four proteins. The adherence proteins were not classified or marked but their presence was detected with the label-free approach.

Figure 2.6 shows the correlation between all the markers for all cells individually. Figure 2.6.a and .b present the correlation of onset between the fluorescent markers. It is clear that the order of onset of fluorescent markers at single cell level are the same as observations in population studies. The heterogeneity at single cell level is also present at the onset of proteins as well. While the order is preserved, the time-difference between onsets are different in same population.

The colors indicate individual fluorescent markers and the intensity of color indicate the number of cells. Figure 2.6.c shows the correlation of the onset of fluorescent markers with respect to the adherence time points. Adherence occurs before the onset of the differentiation markers as seen by the fact that most data points fall above the isochronic dashed line. However, the correlation between these events are not very strong.

Our study demonstrated that the micro-well arrays enable single cell analysis of the

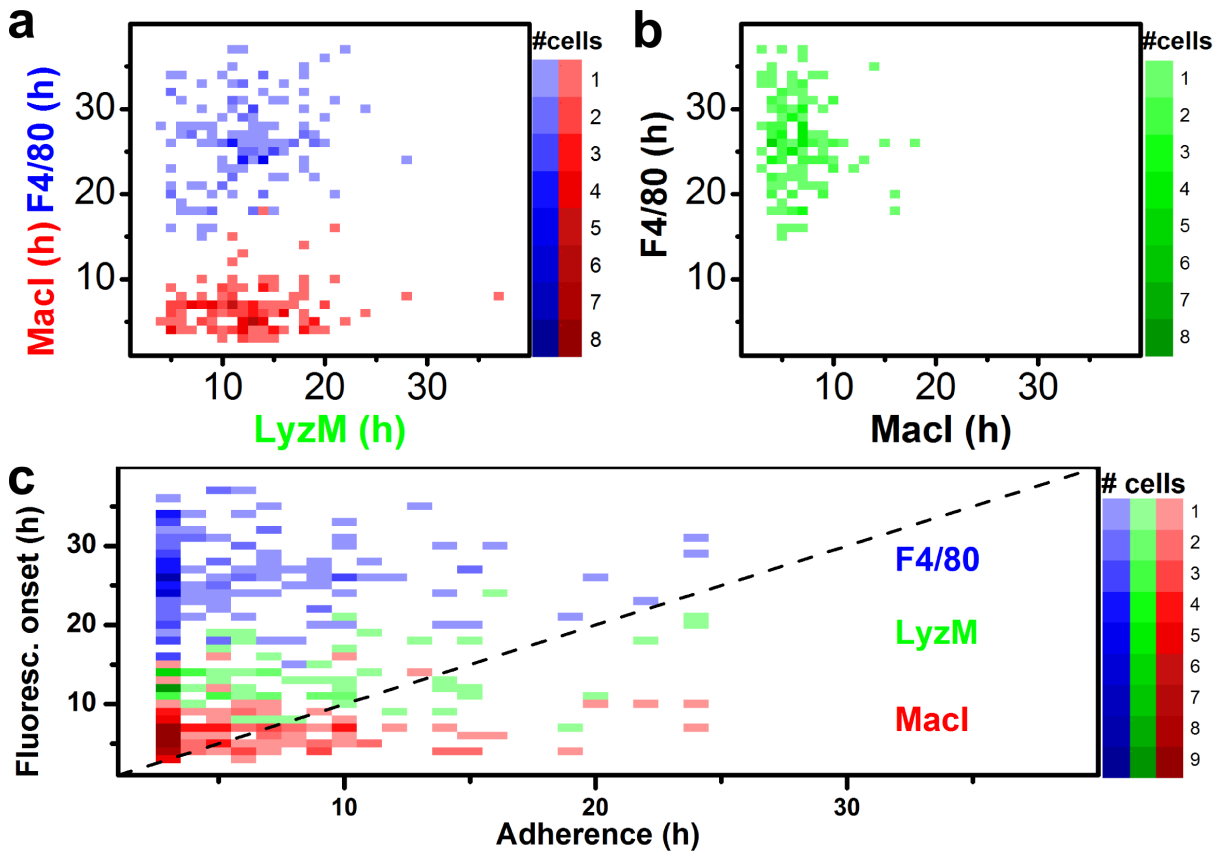

Figure 2.6: Correlation of onset of markers.
a) Fluorescent data correlations with respect to LyzM onset. MacI is the earliest marker while F4/80 expressed at the latest stage. b) The correlation of onsets between MacI and F4/80. c) The single cell data correlations between the onset of fluorescent markers and cell adherence. MacI (red) and F4/80 (blue) are tagged with anti-body, and LyzM (green) is engineered in the cells. Dashed line is the isochronic line.

transition from a non-adherent to an adherent state utilizing Brownian motion as reporter. GMPs exhibit heterogeneity in the timing of both the adhesion transition as well as differentiation at the single cell level. In contrast to manual evaluation, our unsupervised approach allows for high temporal resolution and increased statistical accuracy of the adhesion time point. Clearly adhesion is an early indicator of differentiation. Yet, the statistics of adherence events does not seem to strictly depend on the stage of differentiation. Hence the molecular changes at the cell surface that allow for adhesion do not seem to be directly timed within the differentiation process. Single cell analysis of Brownian motion therefore provides a versatile label-free method for high-throughput detection of the adherence transition. In principle, the only limitation on the observation time in our approach is the point of cell division. We believe that the highly parallel analysis of single cells by monitoring of Brownian motion is a powerful, high-throughput, label-free method,

which is particularly promising for the time-resolved investigation of differentiation and the detection of changes in cell-surface properties of non-adherent cells.

Chapter 3

Dynamics of apoptosis in tumor cells

Cells in the human body constantly grow and replace old and damaged cells, replacing 50 to 70 billion cells a day in an adult human, approximately one body-weight per year [89]. The tightly regulated apoptotic machinery in a cell plays an important role for clean removal of cells to maintain a healthy organ. The cell-fate decision making process that instruct the cells to follow an apoptotic pathway is of high interest.

In cancer treatment with chemotherapy, the goal is to activate the apoptotic pathways of cancerous cells to cleanly remove the tumor from an organ. The complete eradication of cancerous cells are very important, since even a $\sim$2% remains of cells could result in a recurrence of cancer [90]. The cells of a tumor can form several subpopulation which have different sensitivity to the chemotherapy. In order to completely eradicate the cancer, it is necessary to characterize chemosensitive and chemoresistant subpopulations. Single cell studies of cancer cells can shine light on the key components in cell fate-decision making machinery which contribute to the response to chemotherapeutic drugs. The findings can be used to attack the cancer populations at their most susceptible state, hence increasing the efficiency of chemotherapy and reducing the side effects. This goes hand in hand with the selective tumor targeting studies.

In the first two sections of this chapter we introduce the biological background of the apoptosis pathways and cancer treatments. We have developed a microfluidic platform and microscopy setup for single cell time-lapse studies of cancer cells. The properties of this setup is shown in section three.

In the fourth section we report the results of our study on the effects of doxorubicin on the leukemia cells and the single cell correlations. We showed the high correlation between the division of sister cells. We have also provided the evidence that the drug-response in an artificially synchronized population is different from the intact, i.e. non-synchronized, population.

In the final section we introduce the Raman spectroscopy as a label free apoptosis detection technique. We showed that this technique can be used on our high throughput single cell platform and give a reliable detection for apoptotic stages of cells.

3.1 Pathways to cell death

Cells in the human body are constantly regenerated and replaced by new cells. There are two mechanisms that damage a cell, either an external physical or chemical stress, or internal failures in cell machinery. In both cases, the cells response is to adapt, repair, or die depending on the extend of the damage. The internal damages can be a result of accumulation of small damages, e.g. old cell, which in turn can lead to an irregular cell. The highly compromised cell must be removed from the organ to prevent further damage to the tissue and open space for growth of healthy cells. The old and damaged cells go through well regulated death pathways and are removed from the organs.

There are several pathways that each cell chooses or is forced into which leads to a dead cell. The cell death is a well regulated procedure with internal signaling pathways as well as external morphological signatures. The mechanisms are categorized into three major groups based on morphological changes, they are called apoptosis, necrosis, and autophagic [91, 92].

In an **apoptotic cell** the plasma membrane keeps its integrity until the late stages of the process. During apoptosis, cytoskeleton proteins are cleaved and subcellular components collapse, the chromatin condenses and the plasma membrane produce blobs, i.e. apoptosis bodies, which carry the debris out of the cell for disposal [64].

An **autophagic cell** has a high vacuolization of organelles in cytoplasm and no chromatin condensation. This process initially helps prevent cell death due to starvation, by digesting the unnecessary components in the cell, however, if self-digesting, i.e. autophagy, continues for a long time, the cell cannot recover and function anymore and dies [91].

A **necrotic cell** initially opens its plasma membrane channels leading to an influx of surrounding medium. This results in the distinct morphology change such as an increase of cell volume, organelle swelling, and the membrane rupture. Necrosis is also defined as a lack of the features of autophagy or apoptosis death [93, 94].

While apoptotic and autophagic cells are easily cleaned from organs by macrophages, necrotic cells rupture rapidly before macrophages could contain the residue. This can damages the neighboring cells and lead to local inflammation and irritation. The apoptotic pathway to cell death is a complex system with some interconnection to necrotic or survival pathways [95]. We have reconstructed the apoptotic pathway from literature [96, 97, 98, 99] as is shown in Figure 3.1.

Recent finding on molecular pathways of cell death changed our perspective on the cell death mechanism. For an in-depth description of the new realization of different mechanisms please see the works by Broker et al. [98] and Lavrik et al. [100]. A widely accepted phenomenon in early studies of cell death was that necrosis is an “accidental cell death” and there is no regulation. However, recent studies showed that it has indeed a highly regulated pathway [101]. The second widely believed phenomenon was that the caspase molecular system is always present in apoptosis. However, it has been shown that in response to a single death stimulus, more than one death program is accessible. The alternative pathways, e.g. AIF or EndoG in Figure 3.1, can override the caspase pathway and induce a caspase independent cell death (CICD) [98].

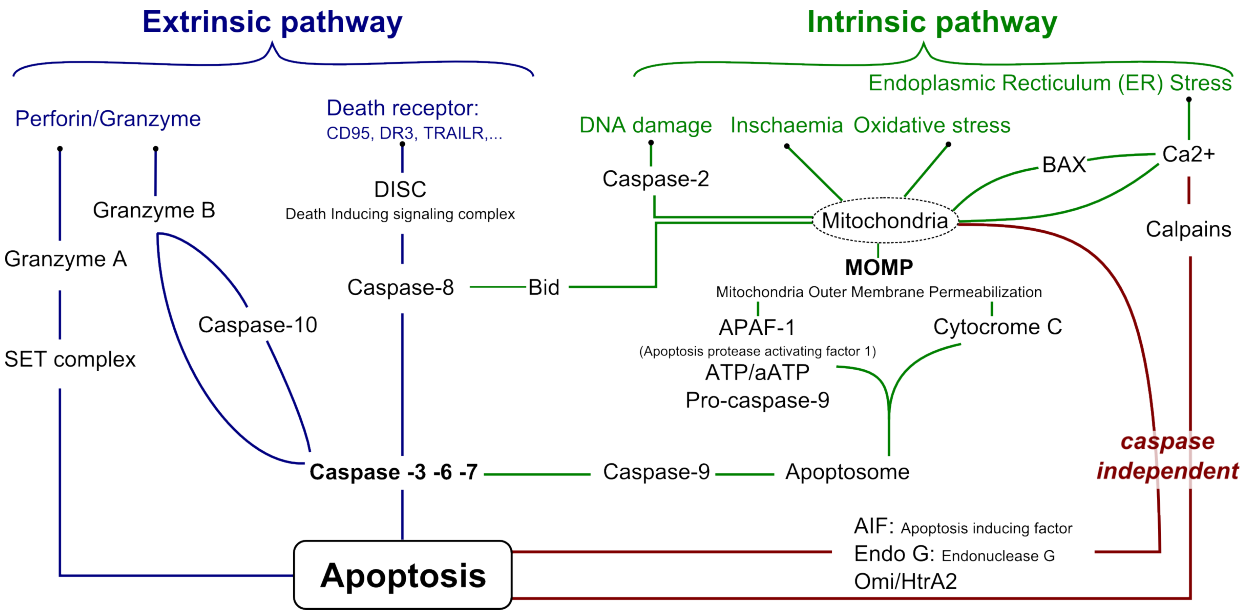

Figure 3.1: A summary of several apoptotic pathways. Extrinsic pathways are either activated by death receptors on the membrane (e.g. CD95, TRAIL) or cytotoxic chemicals from natural killer (NK) cells (e.g. Perforin, Granzyme). Intrinsic pathways are activated through malfunction of the cell system or chemical imbalance in cell (ischaemia, DNA damage, etc.)

3.2 Apoptosis in cancer treatment

Cancerous cells form a tumor generally because they have a malfunctioning growth and turnover pathway. Kerr, Wyllie and Currie [24] coined the term "apoptosis" as a programmed cell death and at the same time proposed that a damaged apoptosis pathways leads to the development of tumors. The subsequent studies showed that Bcl-2 (B-cell lymphoma) family of proteins has a key role in controlling the apoptosis pathway [102]. At the same time, miss-expression of Bcl-2 family was found to be the cause of several types of cancers (e.g. lymphoma) [103]. These findings proved that a malfunction in apoptosis machinery plays a crucial role in cancerous behaviors of cells. Hence identifying and reprogramming the damaged genes in apoptotic pathways can be used to attack tumors.

Cotter's chronological review of apoptosis and cancer research [25] illustrates how repairing the abnormalities in the apoptosis pathway of tumorous cell on the one hand, and targeting the surface triggers of apoptosis, on the other hand, provides two effective ways to attack tumors. For example, reactivating Bcl-2 family of proteins or triggering CD95 family of receptors shrink tumors (see Figure 3.1). Many target drugs for membrane receptors of apoptosis pathways have been developed as chemotherapeutic drugs, e.g. for CD95L receptors [25]. Several other drugs are under development which are targeting outer mitochondrial membrane, P53 and other death receptors. Green and Kroemer [104] investigated the studies on a comprehensive list of targeted chemotherapeutic drugs and

found that the method and applications are indeed promising for future cancer treatments.

3.2.1 Chemotherapy: Inducing programmed cell death

Paul Ehrlich, who coined the term "chemotherapy" defined it as the use of chemicals to treat diseases. Nowadays, chemotherapy is specifically used for the application of chemicals in cancer treatment. The introduction of chemotherapy in cancer treatment has had ups and downs as discussed by DeVita and Chu [105]. The success of chemotherapeutic drugs in cancer treatment in the early 1960s made this technique a standard treatment for cancers. The advances in chemotherapeutic drugs, protocols for its administrations, and its combination with other types of cancer therapy, such as surgery and radiation, increased the success rates in cancer treatment. The cure, i.e. more than 90% success, for acute lymphocyte leukemia and Hodgkin, and high success rates in other types of cancers [105], reinforce chemotherapy approaches.

Cancerous tumors are recognized by the uncontrolled growth of cells, commonly due to abnormality in the cell cycle or growth inhibitory machinery of cells. Normally, cell growth in tissue is controlled by number of extra-cellular chemical and mechanical signal. One of the mechanical signals is the "contact inhibition", which happens when two similar cells come into contact with each other and because of this interaction they stop dividing. When this mechanism is damaged in cells, they keep dividing and grow into the abnormal mass of cells, a tumor. The abnormality in the cycle of growth in tumorous cells suggests a target point for the attack of chemotherapeutic drugs. The drugs can attack the abnormalities in machinery to specifically kill the compromised cell. The efficiency of chemotherapy in this scenario is based on their capability to attack the cell cycle (See Appendix F for brief description of cell cycle).

Two of prominent chemotherapeutic drugs are doxorubicin and chondramide. Doxorubicin is an anthracycline (antitumor antibiotic) drug that interferes with enzymes involved in DNA replication and attacks the cells at any phase and is considered a cell-cycle specific drug. Chondramide, a myxobacterial cyclodepsipeptide, binds to actin cytoskeleton and leads to hyperpolymerization [106] and subsequently arrests the cells in G2/M phase. It has been recently shown that chondramide can specifically target cytoskeleton of tumorous cells [107] and inhibit angiogenesis [108].

3.2.2 Combinatorial chemotherapy

Combinatorial chemotherapy is the combined administration of different drugs at specific time-points according to a defined protocol. One of the main issues in chemotherapy is the relapse, reappearance of cancer from untreated or chemoresistant cancer cells. Miwa et al. [90] showed that in response to chemotherapy some chemoresistant subpopulation of a tumor are only arrested in a cell phase and continue proliferation after drug release. Combinatorial chemotherapy increases the chance of killing the cancerous cells by attacking them at different points in a cell cycle.

On the other hand, a detailed knowledge of behavior of heterogeneous population can be beneficial for chemotherapy. Knowing the dynamics, one can use an initial drug to arrest the chemoresistant cells at a vulnerable cell phase and with a second drug attack and kill the cells at this point. [109] showed that an arrested tumor cell is more susceptible to the TRAIL-induced apoptosis. The use of multiple drugs and at different time-points decrease the chance of drug resistance and untreated cells dramatically and is shown to reduce the relapse probability. Time lapse single cell microscopy is an important approach to reveal the source of underlying heterogeneity and the cancer cell relapse.

3.2.3 Cell-to-cell variability in drug-response

Population heterogeneity in a single type of cell arises from different sources: genetic, epigenetic or temporal variation. **Genetic** variation happens over several generations of cells mainly through mutation and changes in DNA. **Epigenetic** variation is at the level of protein transcription which is inherited by daughter cells and have long term effects. **Cell-to-cell variation**, i.e. temporal variation, is a result of stochastic variation in protein production. It has been shown that inherent stochasticity in cell machinery leads to observable cell-to-cell variability even between two sister cells [110]. The heterogeneity at all levels can result in different responses to chemotherapy, hence the fractional killing of tumorous and future relapse of cancer can occur.

New findings showed that the cell-to-cell variation, rather than genetic or epigenetic variation, plays a more important role in heterogeneity than it was thought before. Spencer et al. [110] showed that the protein level, as well as a single reaction rate in a cell can have a notable effect on the response time to the TRAIL-induced apoptosis. Raychaudhuri [111] applied a Monte Carlo simulations on the *in silico* single cell data and showed that the kinetics of apoptosis is better explained when including a cell-to-cell variation in the analysis.

The heterogeneous tumor population can affect the efficiency of a chemotherapy and result in fractional kills. Albeck et al. [112] used fluorescent single cell microscopy to quantitatively measure the caspase activation dynamics in relation to other components of extrinsic apoptosis pathways, e.g. MOMP or Bcl-2. A more detailed investigation of the effects of population heterogeneity in drug response is needed to design an optimal (combinatorial-) chemotherapy protocol for complete eradication of tumors.

Single cell time lapse studies of cancer population over the course of drug treatment can shine light on the heterogeneity in population and quantitatively measure the drug response dynamics. With time-lapse single cell studies we can address issues like dose dependence, time of drug-administration dependence, effects of intrinsic stochasticity, cell cycle dependency, ... In the next section, we introduce our single-cell time-lapse study of the dynamics of apoptosis under the influence of chemotherapeutic drugs.

3.3 Single cell study of the dynamics of chemotherapy

The study of the effects of chemotherapeutic drugs on the tumor population is a crucial step to find an effective chemotherapy with complete tumor eradication capability. Single cell studies are required to resolve the subpopulations and their heterogeneities in drug response. Single cell studies clarify the interplay between different parameters in tumor development as well its response to drug.

The fluorescent markers are primary method of single cell studies. Molecular markers at different points of apoptotic pathway death has been constructed and used for the detection of cell death [113]. The endpoint single-cell studies such as fluorescence activated cell sorting (FACS) shows the percent of cells at one time point. Time-lapse fluorescent microscopy, on the other hand, is able to resolve the inter cellular dynamics. Time-lapse single cell studies has shown that the speed and response dynamics varies at different points of apoptotic pathways. Time lapse single cell studies are able to evaluate the heterogeneity in response to chemotherapeutic drugs with respect to different dynamics along the apoptotic pathways. We have studied this phenomenon in subsection 3.2.3.

The ability to target, manipulate, or repair cell death pathways depend on the correct understanding the dynamics of molecular machinery. A single cell study of tumor cells can shine light on the key components in apoptotic pathways and dynamics of cancer treatment methods. Time lapse fluorescent microscopy is helpful in identifying the subpopulation and characterizing the type of heterogeneity in drug response.

Here we have developed an *in vitro* system to study the population response to drug at single cell level. A family of cell from a single ancestor is confined to a single micro-slit. This micro-slit arrays have two advantages in single cell studies. By confining the family, we can easily detect the variation between sister cells. Since sister cells are genetically identical, we are able to directly observe the epigenetic and cell-to-cell variabilities in the system. Additionally, the exact division time of each cell is known. The division point is used to achieve a non-invasive synchronized data. This was used to observe the effect of artificial population synchronization on the drug-response characteristics of cells.

3.3.1 Micro-slits: localization of single family of cells

In order to track non-adherent cells over several generations, we have designed and fabricated micro-slits which can accommodate only 4 to 6 cells. Full description of microstructure was already mentioned in chapter 1. These structures can localize cells in a small area and separate single cells from the population. A low-density seeding of cells will give high probability of initial single-cell occupation, hence the possibility to analyze a family of daughter cells from a single ancestor cell. Figure 3.2 shows the schematic of micro-slits and the cell generation tracking. The ratio of the width of micro-slit to the diameter of cell which is around 1.5-2 prevents any confinement stress on the cell while still localizing it. As shown, a single cell can be tracked for two generations while keeping all the daughter cells in one compartment.

As previously discussed, the cell phase have a key role in the efficiency of a chemothera-

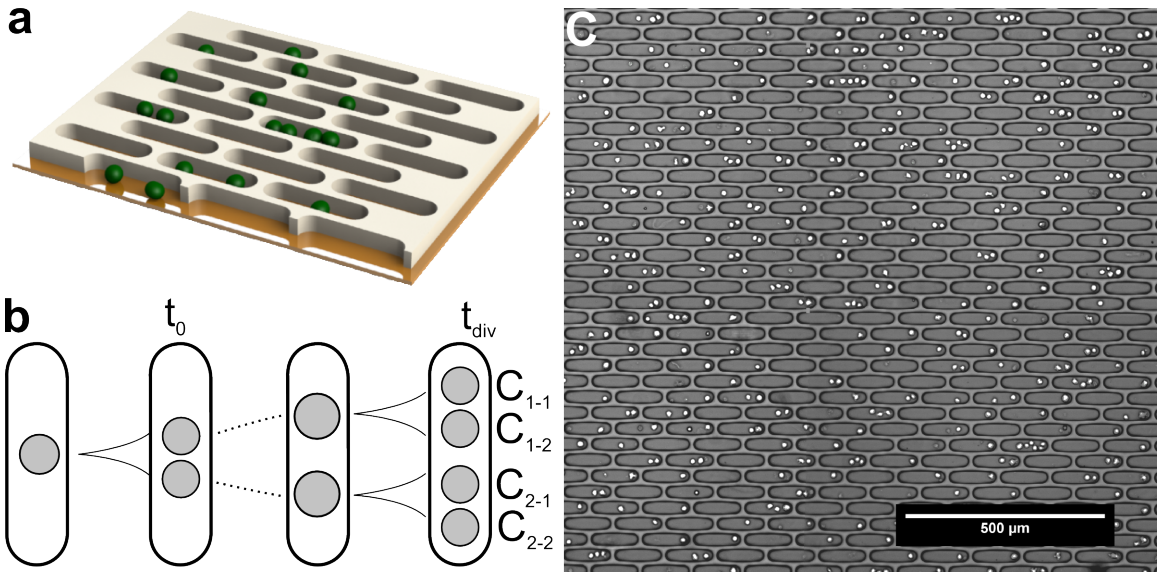

Figure 3.2: Single family micro-slits.
a) 3D model of micro-slit on surface with cells inside. b) Composition of family tree, keeping the identity of all daughter cells. t_0 indicate the first division and t_{div} is the second division. c) An overview of micro-slit structures with the cells seeded.

peutic drug. Hence, an important aspect of chemotherapy studies is to know the cell phase during the experiments. There are three standard methods to identify the phase of a cell: morphological characteristics, fluorescent tagging, and cell synchronization. Each of these methods have advantages and disadvantages.

While the morphology of different phases of a cell is distinguishable for adherent cells, for non-adherent spherical cells it is hard to identify the cell phase solely from the morphology. Fluorescent tags such as FUCCI cell cycle sensor (lifetechnology, Germany) can identify the cell phases [114], however they use two channels in fluorescent microscopy and limits the fluorescent tags to investigate the correlations with for example apoptotic pathway.

The common cell cycle synchronization methods are based on arresting the cells in a specific phase and then releasing all of them at the same time. These methods have two drawbacks. At single cell level all the cells are not in the exact cell phase, but have a distribution around the arrested time point. Additionally, this method affects the natural state of cell, and as it was shown an arrested cell have different susceptibility to the chemotherapy [109].

A non-invasive method of cell cycle detection is desirable. We showed the single family tracking as a reliable label-free technique to identify the cell-cycle. With the single family tracking over two generation, the time after first division (t_0) is known. This time can be used as a proxy, i.e. a label-free indicator, of cell age. Correlating the age and morphological characteristics of the cell, the phase of a cell can be revealed for non-adherent cells. We have compared the responses from this intact, i.e. non-synchronized, population with a

drug synchronized population.

3.3.2 Cell line

The model system is a non-adherent acute leukemia (AML-M5a) cell line called MOLM-13 [115]. They have round shape morphology and grow in suspension. The cell lines used here are grown in RPMI 1640 medium with stable L-glutamin (Biochrom, Germany) and supplemented with 10% Fetal Bovine Serum (FBS). 1mM Sodium pyruvate (c.c.pro, Germany) is added to compensate for low diffusion of CO_2 in channels and act as a CO_2 independent medium [60]. Throughout this report we refer to this composition as *ExpMedium*.

The synchronized population was made according to "double thymidine block" as described by Jackman et al. [116]. The detailed description of method is given in Appendix F. Double thymidine block arrests the cells at the border of G1/S-phase.

3.3.3 Apoptosis detection

Based on the aforementioned discussion in section 3.1, we use the definition of apoptosis based on its morphological classification. The fluorescent signal of apoptosis is from the activation of caspase 3/7 and the signal of necrosis is from the diffusion of PI into the cell. The "caspase 3/7 positive" cells are indicated by a green fluorescent signal of CellEvent™ Caspase 3/7 Green marker (Lifetechnologies, USA). The CellEvent™ substrate has to be cleaved by an activated caspase-3 or -7 to be able to bind to DNA and produce a fluorescent signal. A necrotic/late apoptotic cell is also defined as "PI positive cell", indicated by propidium iodide nucleic acid marker (Novus Biological, CO, USA). PI is membrane impermeable and can only enter the cell and bind to DNA when the membrane is damaged which happen in necrotic cells or late apoptotic cells.

3.3.4 Fluorescent microscopy

We have used the time lapse brightfield images with 5 minutes interval to track individual cells over 48 hours. The raw movie of out-of-focus images was preprocessed using thresholding-based algorithm [11] (built around the maximally stable extremal regions (MSER) [117] algorithm). The processed movie is then imported to TrackMate [118] (an ImageJ plugin) for individual cell tracking over time. The trajectory of individual cells were analyzed for the intensity of fluorescent markers in two fluorescent channels to detect the cell death signal.

A fluorescent image is taken every hour using a Zeiss Axiovert 100M inverted microscope. The CellEvent™ marker is mixed with a ratio of 20 µl per 1 ml of *ExpMedium*. The PI marker is mixed with a ratio of 5 µl per 1 ml of *ExpMedium*. It has been shown that PI presence in medium is not toxic for cells [119]. The fluorescence is detected in green with "Zeiss Filterset-10", with a band pass excitation filter (450-490 nm) and bandpass emission filter (515-565 nm) and in red with "Zeiss Filterset-00", with a bandpass excitation filter (530-585 nm) and longpass emission filter (616 nm).

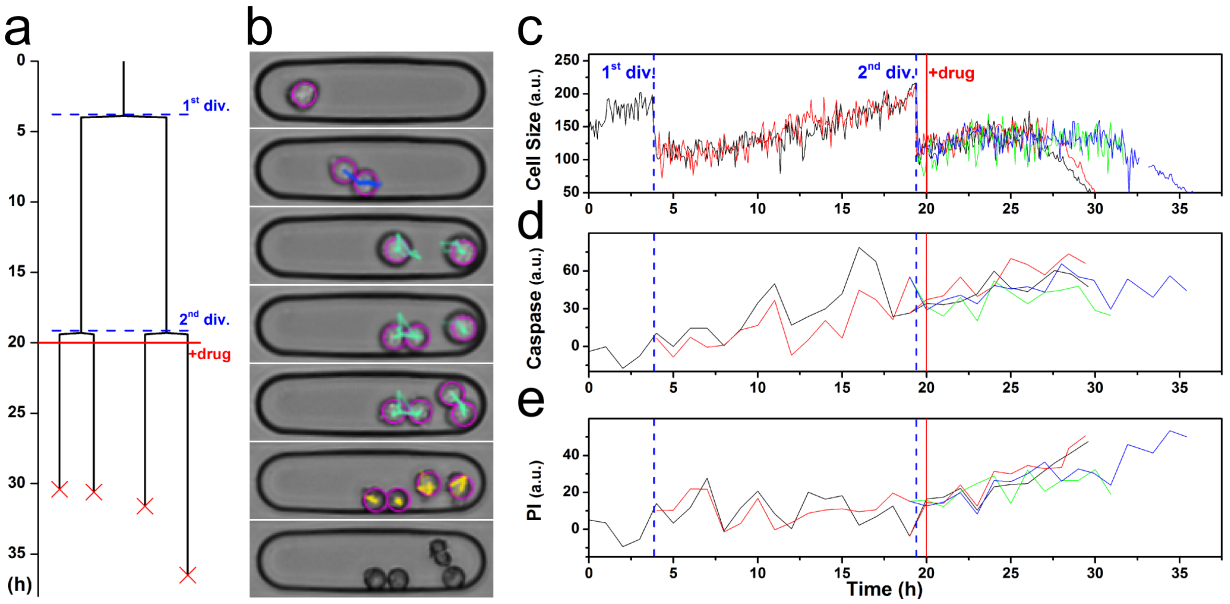

Figure 3.3: Single family tracking in micro-slit.
a) Family tree of four daughters from a single ancestor. b) Corresponding brightfield images. The detected single cells are in purple circles and the trajectory of cells are color coded with the last 10 steps visible in each frame. The properties of single cells are extracted from their tracks. The cell size (c) is estimated from the bright field image. The intensity of fluorescent signal is also obtained for the Caspase 3/7 marker (d) and PI signal (e).

Figure 3.3 shows all the major steps for tracking one family of cells in one micro-slit. Figure 3.3.a is the family tree from a single ancestor in one micro-slit which give rise to four granddaughters as shown in the corresponding brightfield image in Figure 3.3.b. The cell detection and tracking is done automatically and in parallel for the complete array of the micro-slits. Figure 3.3.c-e shows the three signals that are automatically obtained from the samples plotted against time. Cell size is used as a representative of cell morphology (Figure 3.3.c), caspase is the early apoptotic signal (Figure 3.3.d) and PI is the late apoptotic signal (Figure 3.3.e).

The background correction was performed using and in house software based on earlier work in our collaborator's group [120]. After background correction, the signal from the fluorescent channels has been measured as presented in Figure 3.3.c. While both fluorescent signals show an increase at cell death, the intensity was not strong enough for an automatic and decisive indication of cell death. On the other hand, the cell-shrinkage during the apoptosis provides a distinct signature for cell death. Here we used this signal for further analysis.

3.3.5 Chemotherapeutic drug

We have chosen the proposed drug combination from [107] and, in the initial set of experiments, followed the dynamics of cells in response to doxorubicin. The stock concentration of 25 µM of Doxorubicin hydrochloride (VWR, Germany) in PBS is diluted in *ExpMedium* for final drug concentrations in the experiments, i.e. 250 nM. Drug is added at 20 hours after start of imaging to the whole micro-array. This means that for each individual cell, the relative time of drug administration and cell-cycle is different. From the single cell tracking over the first generation, we are able to calculate the exact time from the cell devision, hence we know the cell phase at the time of the administration of the drug.

3.4 Statistical correlation analysis of single cell events

The dynamics of cells and their machinery is a stochastic phenomenon and a simple analysis of microscopy data can not elucidate the process behind it. The statistical models and analysis of data can give us a better understanding of the fate-decision making of cells. Dingli et al. [88] applied a stochastic analysis on the behavior of the tumor cells and proved that including the stochastic dynamic in the analysis can explain both remission and rapid expansion in tumors. A study of heterogeneity in stem cell populations provides clues about the dynamics of differentiation [121]. We have also showed in chapter 2 [74] that the statistical analysis of motion can substitute the fluorescent markers.

Besides the fluorescent signal, single family tracks contain several descriptive features of trajectory and morphology of cells such as their temporal and spatial proximity. Through these data, we are not only able to extract the heterogeneity of population, but also the correlations between the response of unrelated-neighboring cells, sister cells or cells at different cell phase.

3.4.1 Doubling time

In our studies, we followed the family of single ancestors over two generation using micro-slit arrays. This way we could directly resolve the doubling times of cells at single cell level. Figure 3.4.a shows an exemplary track of one cell which gives rise to four cells within the first 30 hours. The doubling times of a cell (t_{div}) was measured from the difference of the first t_0 and second divisions. Without the loss of generality we called the first daughter cell that divides number 1, with doubling time of $t_{div}(C1)$.

The model system, MOLM-13 cells was observed for 40 hours to allow for a minimum of two division. Figure 3.4.b shows the experimental results from a population of 320 cells.

Doubling time distribution

The doubling time of cells is an important factor in prediction and the control of size of a population, e.g. tumor growth [122], therefore, it has been modeled and described.

Gregory et al. [123] has modeled the distribution of tumor doubling time for leukemia tumors.

The base of almost all of mathematical model present is the von Foerster equation for age density function [124]. Von Foerster proposed the model as a way to describe the behaviors of cells in a population. The equation,Equation 3.1, describes the variation of the number of cells $n(a,t)$ at each cell phase in a given time:

$$\frac{\delta(n)}{\delta(t)} + \frac{\delta(n)}{\delta(a)} = -\lambda(a)n \tag{3.1}$$

Here, a is cell age, t is the time, and $\lambda(a)$ is the cell loss factor, which can be due to cell division or death. Assuming that the loss factor λ is only due to division, a probability density function (pdf) $\omega(a)$ can be used to describe doubling time at single cell level. Several studies used a gamma distribution function [125, 126, 127] as pdf. This choice has been suggested by postulating a stochastic birth process in theory [128] and empirically on bacterial populations [129].

On one hand, a gamma distribution can be described as a sum of exponential functions. On the other hand, cell division is a consequence of several inter and intra-cellular steps which in turn can be described by exponential functions. Therefore, as Baranyi et al. [130] also argued, a gamma distribution can better explain the doubling time over other types of distributions. Equation 3.2 shows gamma distribution for a population of N single cells. Where β and α are the rate and the shape parameters of equation, respectively.

$$N\omega(a) = N\frac{\beta^{\alpha}\left(a-a_0\right)^{\alpha-1}}{\Gamma(\alpha)}e^{-(a-a_0)\beta} \tag{3.2}$$

Where in Equation 3.2, the mean value is $\tau_{ave.} = \frac{\alpha}{\beta}$ and the standard deviation $\sigma = \sqrt{\alpha/\beta^2}$.

In Figure 3.4.b the single cell distribution has been fit with the gamma distribution, shown as dashed blue line. The average doubling time here is $\tau_{ave.} = 19.7$ hours which is in good agreement with population average. The standard deviation in this population is $\sigma = 2.6$ hours.

Log-normal or gamma distribution

Some of the population studies on tumor cell propose the log-normal distribution for modeling of doubling time in different colonies [131, 123]. Hosoda et al. [131] also showed that the log-normal distribution is widely present in several fields of science with similar characteristics, suggesting a global model behind it. However, most of these studies lack the comparison to the gamma distribution.

We have included this comparison between gamma distribution and log-normal distribution on our single cell data. In Figure 3.4.b the red dotted line is the fit with log-normal distribution. The statistical tests on both fit did not show any great difference between two functions. The average doubling time from the log-normal fit is $x_c = 19.7$ hours, same as before.

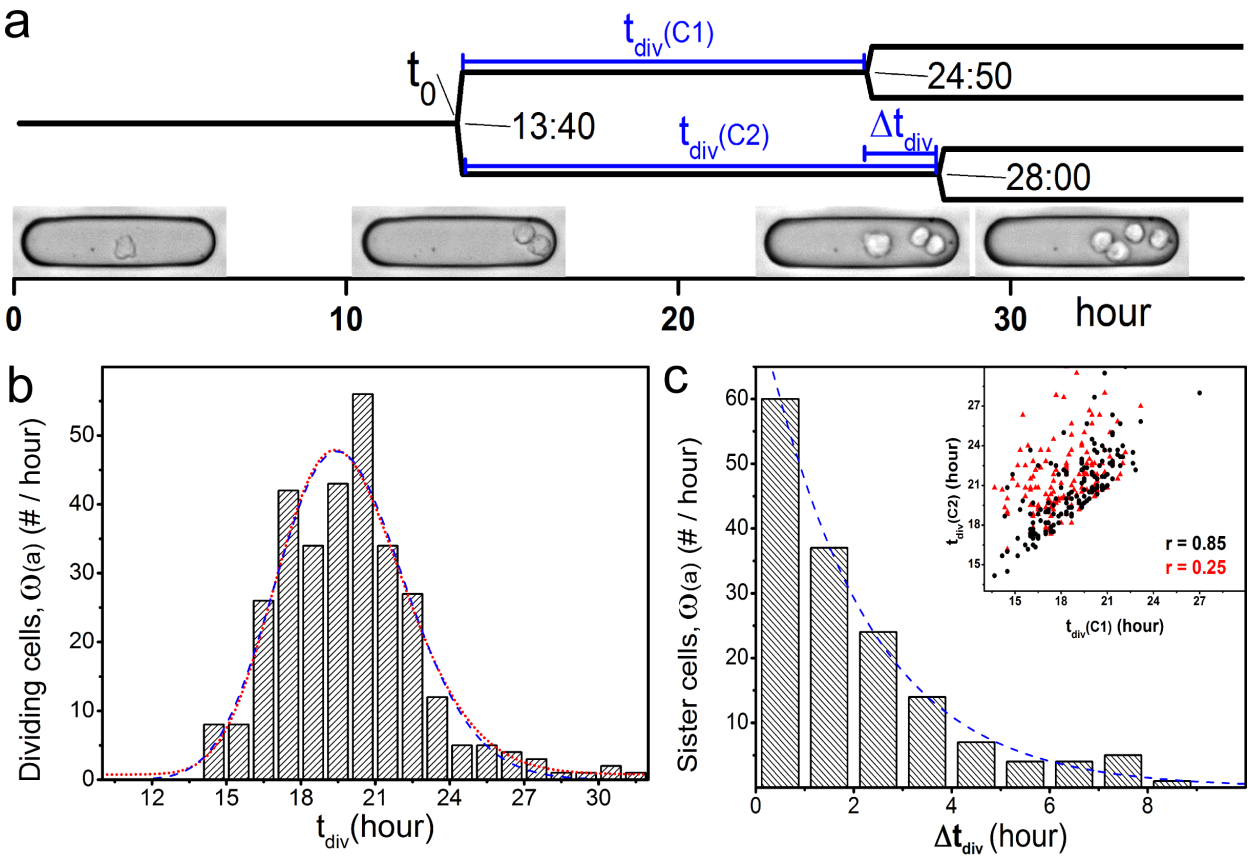

Figure 3.4: Distribution of doubling time of MOLM-13 cells.
a) Exemplary track of a single family of cells with corresponding brightfield images at selected time-points. t_{div} is the doubling time of individual cells. b) Distribution of doubling time t_{div} from 320 cells with an average of 19.7 hours. The log-normal fit is the dotted red line and gamma distribution fit is the dashed blue line. c) Distribution of the difference between doubling time of sister cells Δt_{div}. The dashed blue line shows the gamma distribution with mean value of $\tau_{ave.} = 2$ hours. Inset: Correlation plot of t_{div} for sister cells (black dots) and randomly-paired cells (red triangles). The Pearson Correlation Coefficient for sister cells is r = 0.85, and for random-paired cells is r = 0.25.

The variation in doubling time can be due to genetic mutation of cells as well as a cell-to-cell variation. The sister cells have same genetic background, therefore it is possible to only observe the effects of cell-to-cell variations. In the next section we introduce the correlation between sister cells to investigate whether the distribution arise from the intrinsic stochasticity of cells.

3.4.2 Sister cell correlation

The cell-to-cell variation stemming from non-genetic intrinsic stochasticity of cells. It can be observed by looking at the sister cells in individual micro-slits. Here, we compared the doubling time of the sister cells inside the micro-slits. Figure 3.4.c shows a histogram of the difference of doubling time between 160 pairs of sister cells ($\Delta t_{div} = t_{div}(C2) - t_{div}(C1)$). In order to compare and model this data we looked at the data correlations and a mathematical equation for Δt_{div}.

Definition of correlation

Correlation is a scale that defines the relation between two variables, it is used as an indicator of whether two variables happen at the same time or condition. A common value that described the degree of correlation between two variables is the "Pearson's Correlation Coefficient" or "Pearson's **r**" which was introduced in 1895 [132]. Rogeres et al. described 13 ways that the correlation coefficient can interpret data, e.g. mean values, regression line slope, etc [133]. Here we used the original definition of the Pearson correlation as shown in Equation 3.3

$$\text{Pearson's } \mathbf{r} = \rho_{x,y} = \frac{cov(x,y)}{\sigma_x \sigma_y} = \frac{\sum(x_i - \overline{x})(y_i - \overline{y})}{\sqrt{\sum(x_i - \overline{x})^2 \sum(y_i - \overline{y})^2}} \tag{3.3}$$

Where $cov(x, y)$ is the covariance of the data-sets and σ is the standard deviation of data. To use this correlation, data should come from paired observations and the variables are normally distributed.

Gamma difference diffusion

Assuming the doubling time has a gamma distribution function, the difference in the doubling time between sister cells is a difference of two gamma functions. This difference, called gamma difference distribution (GDD) function, is calculate from the convolution of two gamma distributions functions. Originally Mathai [134] and recently Klar [135] calculated the exact formula of GDD. This complex formula as shown in Equation 3.4 is mixture of several gamma functions. A detailed derivation of formula and applications in our case in done in Appendix G.

$$f(z) = 2^{\alpha-1}\beta^{2\alpha}\frac{\Gamma(1-2\alpha)}{\Gamma(\alpha)\Gamma(1-\alpha)}z^{2\alpha-1} + 2^{\alpha}\beta\frac{\Gamma(2\alpha-1)}{\Gamma(\alpha)^2}, z > 0 \tag{3.4}$$

Stewart et al. [136] showed that the convolution of two gamma functions can be approximated with a new gamma function.

To model our data we approximated the data with a single gamma distribution function. The dashed blue line in Figure 3.4.c shows this fit for Δt_{div} with an average of 2 hours.

To distinguish between the population heterogeneity and intrinsic stochasticity we compared two sets of correlation of doubling time. The first set correlates the doubling time of sister cells with each other. For the second set, we paired two random single cells and

correlate the doubling time of these pairs. In both sets, the condition of $t_{div}(C2) > t_{div}(C1)$ applies. The inset of Figure 3.4.c shows these two correlations. The black dots are comparison of two sister cells with a Pearson's correlation of r = 0.85. The red triangles are from random-pairs with a Pearson's correlation of r = 0.25.

The high Pearson correlation in sister cell doubling time indicates that division happens at approximately same time. However, the variation shows that the non-genetic stochastic variations can already have effects on the first generation. Other studies [137, 138, 139] also confirmed that the intrinsic stochastic variations in protein numbers in sister cells leads to uncorrelated behaviors.

On the other hand, the uncorrelated doubling time (r=0.25) in random-paired cells suggest that the background history of cells has induce a high variability in a seemingly homogeneous population.

3.4.3 Dynamics of response to doxorubicin

The response of MOLM-13 cells to the doxorubicin, a candidate chemotherapeutic drug, is investigated using the cell division as a label-free indicator of cell cycle. Cells are observed for ∼20 hours (approximately one cell cycle) prior to the administration of the drug. This is to assure that the majority of cells have already divided once. The cell mitosis, i.e. division time t_0, is used as the reference point for cell-phase indication. Doxorubicin is added after 20 hours from start of imaging. For each individual cell the age of cell from division to the time of drug administration is noted by T_c. The time it takes for the drug to kill the cell is T_d. See Figure 3.5.a for a schematic of the experimental procedure. The difference between the time of death of sister cells is indicated by ΔT_d.

As explained before (see Figure 3.3.c), T_d is detected with three signals, by Caspase 3/7 marker T_{d-c}, by PI marker T_{d-p}, and by the collapse of cell size T_{d-s}. However, after the experimental data was analyzed we observed a poor fluorescent signal in comparison to the clear signal from the shrinkage of cell upon apoptosis. The manual investigation of these signals show a close time-agreement between the three events, with the sequence as first onset of caspase, second cell shrinkage and finally onset of PI marker.

We have also compared the automatic image processing of the fluorescent signals T_{d-c} and T_{d-p} and the brightfield channels. In both experiments, i.e. synchronized and non-synchronized populations, the morphological changes and degradation of cells were visible much earlier than the presence of detectable fluorescence signal. We believe this is due to the time that the fluorescent markers needs to aggregate on the DNA for a visible signal. This leads us to consider other label-free technique for apoptosis detection. In the automatic detection for statistical analysis, T_{d-s} is used.

Figure 3.5.b shows the scattering of the time to death T_d vs the age of the cell t_c for the single cell events. If the drug would only affect the cells at a specific time in cell cycle, the scatter plot would have concentrated at a specific t_c. The shown scatter plot is evenly distributed at all cell phases. Hence, there is no obvious correlation between the doxorubicin and a cell phase. Spencer et al. [110] observed the similar no-cell-cycle dependency in TRAIL (tumor necrosis factor (TNF)-related apoptosis-inducing ligand)

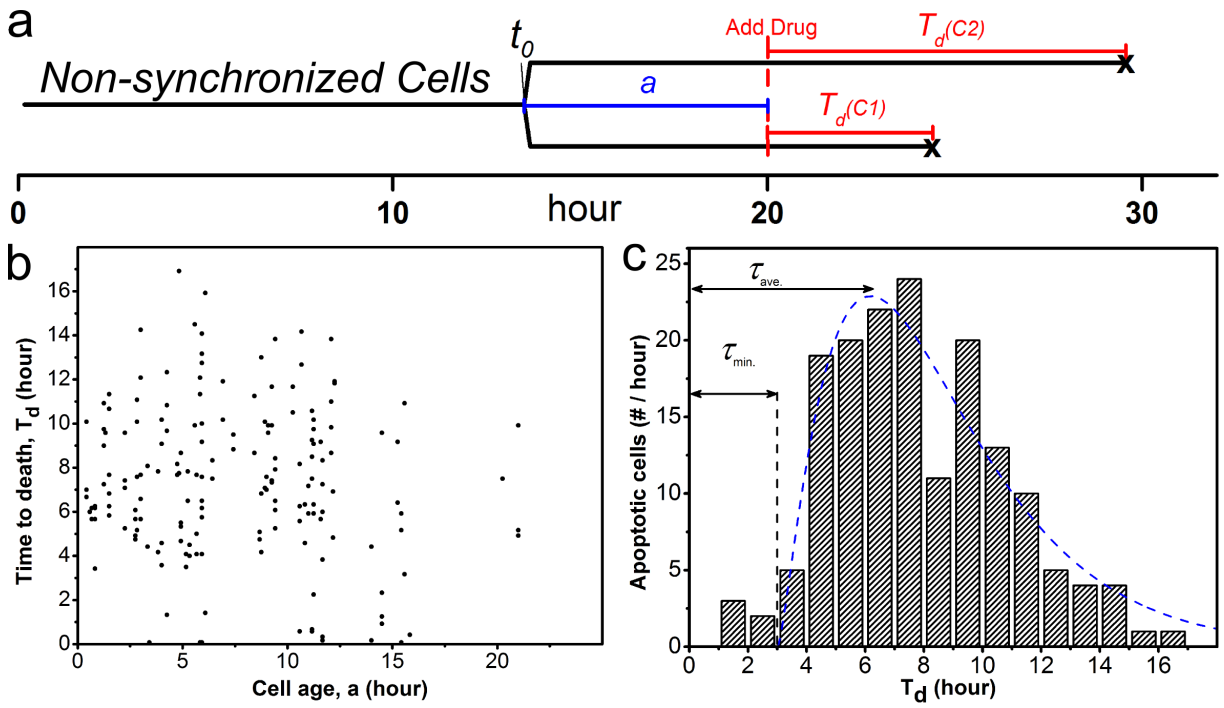

Figure 3.5: Single cell response to doxorubicin.
a) Experimental procedure for drug administration. The chemotherapeutic drug is added after ∼20 hours to let all the cells divide once. The cell age at the time of drug administration is a. The time from the administration of drug to the cell death is T_d. The difference in time to death between sister cells is indicated by ΔT_d. b) Distribution of apoptotic cells in response to drug administration. c) The distribution of time to death (T_d). The minimum lag time for the onset of drug effect on the cells τ_{min} is 3 hours and the maximum killing happens at $\tau_{ave.}$ 5.5 hours.

induced apoptosis of Hela cells.

Figure 3.5.c is the number of death events per hours after the administration of drug. There is an onset time before the effect of drug can be seen on the cells which is indicated as $\tau_{min.}$. The response of MOLM-13 leukemia cells to the doxorubicin in Figure 3.5.c has a 3 hours onset time. The average time to kill the cell $\tau_{ave.}$ corresponds to the mean value of the fitted gamma distribution function which is $\tau_{ave.} = 5.5$ hours. The lag time has been observed in all of the apoptosis studies which depending on the part of apoptosis pathways under investigation can be dose independent or dependent [140].

3.4.4 Dynamics of response to doxorubicin: synchronized population

We have repeated the experiment with exact same conditions on a population of synchronized cells. A “double thymidine block” synchronization [116] was applied to population

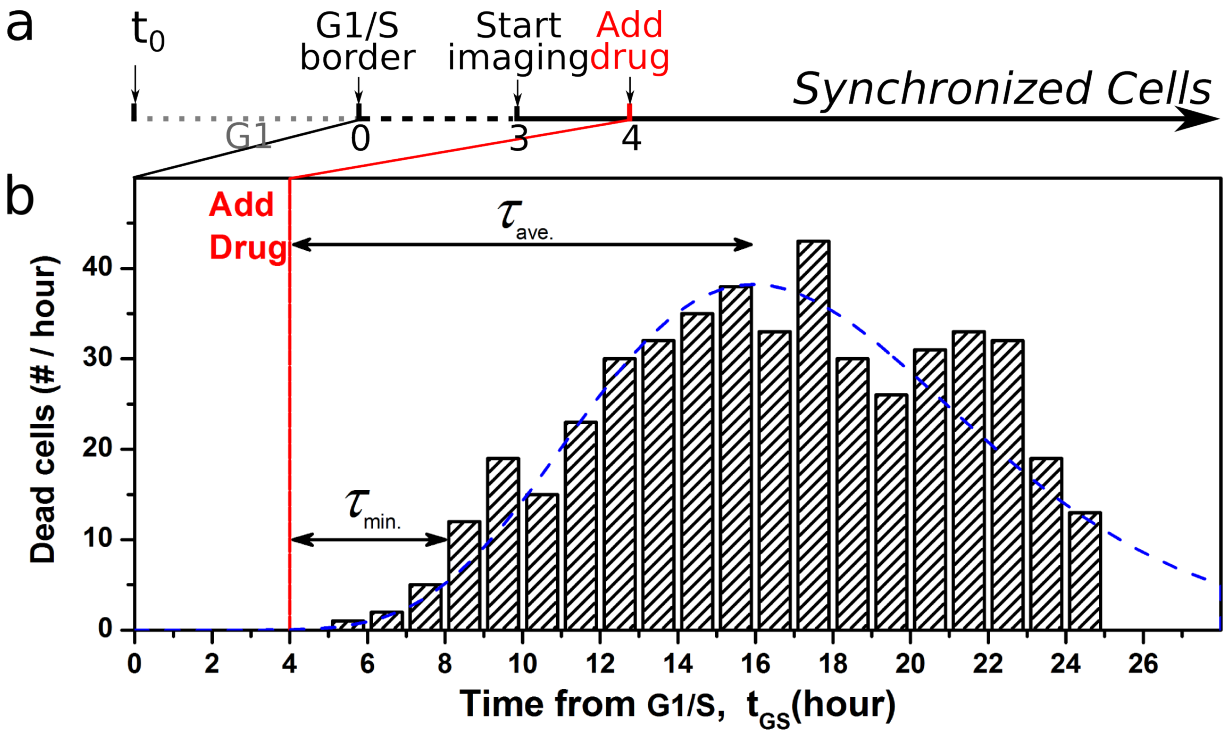

Figure 3.6: The distribution of cell apoptosis from 472 synchronized single cells.
a) Time course of experiment. t_0 is the time of mitosis. Double thymidine block arrest the cells must at G1/S border. The time difference is on average ∼8 hours, i.e. the length of G1 phase. Fluorescent imaging started 3 hours after release and doxorubicin was added at 4 hours time-point. b) The number of apoptotic cells per hour (caspase 3/7 positive cells). The fitted blue line is the gamma distribution with mean value 17.4 hours which results in $\tau_{ave.} = 13.4$. The onset of doxorubicin effect is $\tau_{min.} = 4$ hours.

and then released 3 hours prior to the start of imaging. The synchronized cells are arrested at the border of G1/S-phase. Doxorubicin drug was added 1 hours after the start of imaging.

Figure 3.6.a illustrate the time-line of events and how it is compared to the experiment with non-synchronized cells. The arresting point of synchronized cell, e.g. G1/S border, is later than the division point, t_0, with the length of G1 phase. The length of G1 phase can be ∼8 hours [141]. In Appendix F we have a brief description of cell phases. Hence, the age a for synchronized cell is the time from G1/S border t_{GS} plus ∼8 hours.

Figure 3.6 shows the number of cell death event per hour after adding the drug. In the analysis, we only included the cells that have died within the observation time-window (22 hours) which is around 95% (estimated qualitatively) of all the observed population.

The onset of doxorubicin effect on the synchronized cells, $\tau_{min.}$, is 4 hours. This value is close to $\tau_{min.}$ of non-synchronized cells, suggesting that the onset of drug effect on most susceptible cells is constant. There is a heterogeneity in susceptibility of population, however, it does not have a clear correlation to the cell cycle.

The average killing time for synchronized cells $\tau_{ave.}$ is 13.4 hours. In comparison to the non-synchronized population ($\tau_{ave.}$= 5.5 hours), it takes longer to kill the population of synchronized cells.

The shape of response to drug is also different in two populations. The synchronized cells exhibit broader distribution in response to doxorubicin. The standard deviation of the distribution for non-synchronized cells $\sigma_{non-sync.}$ is 3.6 hours while for synchronized cells $\sigma_{sync.}$ is 5.1 hours.

In order to explain this phenomenon, we must remember two intrinsic characteristics of synchronized cells. First, the synchronized cells are not arrested at a precise moment, but rather have a distribution around the blocking point. Additionally, upon removing the blocking agents and releasing the cells, it is possible that individual cell starts the normal cell cycle at different time-point, which adds another stochastic parameter into the response equation. Both effects can broaden the response distribution.

Miwa et al. [90] showed that in a chemotherapy treatment the arrested cell survive the treatment, and form a chemoresistant subpopulation. In case of delayed release in our MOLM-13 cells, the late cell death can be explain by this phenomenon. The arrested cells, i.e. synchronized but yet not released cells, can survive the attack of doxorubicin. The constant presence of drug in our sample on the other hand assures that onces the cell start their cycle, they will be hit and killed by the drug.

The two aforementioned explanations can explain the broadening and more resistance in the response of synchronized cells, however it does not exclude other artifacts that can be introduced to the population through the synchronization. From our study we could clearly conclude that the synchronization process introduce artifacts in the population response. We believe that our label-free cell cycle detection analysis which uses the division time t_0, do not introduce any artifact in the system and therefor, is closer to *in vivo* conditions.

In the next section we describe a novel idea that come from spectroscopy field and can be used as a label free apoptosis detector.

3.5 Raman spectroscopy & apoptosis signature

The Raman microscopy of a single cell over time can be used to track the development of single cell. The time-lapse fluorescent study of apoptosis has already been shown in previous section, here we propose Raman microscopy as a label free technique to study the response of leukemia cells to the chemotherapeutic drug. Before introducing our apoptosis study, the concept behind Raman spectroscopy and the data analysis is described in the following subsections.

3.5.1 Raman spectroscopy

Raman spectroscopy is based on the inelastic scattering of a monochromatic light. The incident light interact with a molecule to excite it to a virtual energy state, an inelastic photon is emitted when the molecule returns back to a higher energy state (Stokes Raman scattering) or lower energy state (anti-Stokes Raman scattering). The resulted shift in photon frequency is detected for the Raman spectrum (Raman shift). This shift is normally reported as an inverse of wavelength and is called wavenumber. The Raman spectrum of each material has specific signatures corresponding to vibrational and rotational modes of molecule. This is a clear non-destructive signal that is able to identify the composition of materials.

High intensity lasers can nowadays easily be integrated in an optical microscope system and be used to analyze and detect the material composition in micro-particles. It has been extensively used in solid state physics and geology for surface characterization. The coupling of a Raman laser into a confocal microscopy system, enables a raster scan of a bigger area. By selecting for a material and plotting the intensity of their Raman signature on the scanned area, one can produce a micro-graph of distribution of material over a special area, e.g. a cell.

3.5.2 Raman signatures of single cells

Raman micro-graphs is used more and more in cell biology as a label free detection technique. It can identify and map co-localization of bacteria and minerals in magnetotactic bacteria [142], or calcifying bacteria [143, 144].

Klein et al. [15] used the "mutual information" methods on fluorescent image and Raman micro-graph and were able to identify the regions of interest in Raman spectra for cell organelles such as nucleus, mitochondria, cytoskeleton, and ....

The construction of micro-graph takes a long time, from several minutes to hours, therefore the whole-cell averaged spectra is used for live cell imaging. A Raman tweezers is able to trap a cell and collect the Raman spectra from the cell as an ensemble. While the sub-cell spatial resolution is lost, a temporal resolution is achievable. The time-lapse Raman microscopy provides the possibility to investigate the cell development at single cell level. Raman tweezers has already been used to detect cell type in Hodgkin disease

[145], apoptotic versus healthy cells [146, 147], oxygenation cycle in a single blood cells [148], and developmental stages of stem cells [149].

3.5.3 Data analysis: Raman spectra

Raman spectra contains information from individual molecules in the form of intensity and shape of spectrum at each wavenumber. The significance of this information is not immediately visible and a robust analysis and data-interpretation is needed. The multivariable data analysis techniques provide several tools and directions to extract useful information from the Raman spectra.

Background correction

Since all materials, from cell and microfluidic sample, contribute to the Raman signal, the first step is to subtract the background information from the signal of interest. The background correction can either be done by analyzing the spectra with background correction algorithms or use a blanked baseline reference.

The software of our Raman microscopy system, BioRam® (Celltool, Germany), uses an internal background correction algorithm based on Whittaker smoother [150]. The Whittaker smoother is based on a discrete penalized least square algorithm which balances the fidelity of the data and roughness of fitted curve. The Whittaker baseline correction and its implementation on Matlab and R codes are available, e.g. see [151, 152, 153]. Unfortunately, no more detail on the method of implementation of Whittaker smoother in the BioRam® software is given.

The manual background correction uses the raw Raman spectra from empty parts of the sample, e.g. without the cells but including the exact medium and substrate. The empty sample is used as a reference baseline which is subtracted from the raw data.

We tested both background correction on our experimental data and saw no significant difference on corrected spectra and consequently in the output of the multivariable data analysis.

Multivariable analysis

Multivariable analysis is necessary for interpretation of Raman spectra of complex systems especially biological samples [154]. There are two categories for analysis of a composite spectrum: first is to find the linear combination of known spectra to make up the final spectrum of the sample; second is to deduce the original spectra from final spectrum of the sample by training an algorithm with enough exemplary data points. This methods, i.e. inverse least square, need one spectrum per Raman wavenumber, e.g. around 1000 data points for one sample. Advance algorithms can be used to reduce the the number of sample, such as multi linear regression or principal component regression. Here, we introduce two methods that has been used for analysis of biological samples in recent Raman studies: principal component analysis (PCA) and biochemical component analysis (BCA).

Principal component analysis
Principal component analysis method is a non-parametric method which analyze the sets of data and transform them to a new orthogonal set of variables. The new set of variables are uncorrelated and based on statistical variance of initial dataset. The first component is the one with highest variance and the following components has the lowest variance and orthogonal to first set.

The Raman spectra of a cell embeds detail information about the composition of cell material. While the big part of information is identical for every cell only specific parts of data varies in the cells at different conditions. This variation is shown as a change in intensity or position of peaks. The power of PCA analysis can be well used in this situation to reduce the variables, i.e. intensity of wavenumber, to only simple underlying variables (PCs) with significant variance. Plotting the PCs on a x-y coordinate provide a powerful and simple representation for classification of biological samples into the separated, distinguished groups.

PCA has been extensively used in Raman spectroscopy of biological systems, either as a stand alone method or in combination with other analytical methods like neural network learning algorithms [155] or least square analysis [153].

Biochemical component analysis
When working with biomaterial another approach is to use the known set of spectra of pure biochemical components as the basis component for analysis. This is called biochemical component analysis (BCA) [156] or direct classical least-squares (DCLS). The spectra basis for cell consist of spectra of biological components such as DNA, RNA, proteins, and lipids. BCA algorithm looks for a best fit of a linear combination of the basis component that matches the Raman spectrum of sample. The changes in cell components will affect the final spectrum. BCA can directly identify the changes in chemical and biological components of cell. However one has to keep in mind that this analysis is sensitive to the initial choice of basis set.

In comparing PCA and BCA, Ong et al. [157] concluded that there is no significant difference in classification accuracy on apoptosis study. However, if the correct set of initial spectra is available, BCA gives a better insight to the biological changes, while PCA provide no information about the chemical or biological bases of classifications. For our studies, since the complete set of information for a BCA analysis is not ready we chosen the PCA analysis. We borrowed the idea from BCA analysis and chosen the parts of spectra that has already been shown to show a significant changes during the apoptosis.

3.5.4 Label free detection of apoptotic stages with Raman microscopy

It has been shown that the apoptosis and necrotic stages of cells affect the Raman spectrum of cells [147, 14, 158]. The specific Raman peaks can be used as a non-invasive label-free indicator of apoptosis. Here we introduce a structured surface to localize non-adherent

cells for time-lapse investigation apoptosis.

Our model system was doxorubicin induced apoptosis on MOLM-13 leukemia cells. The condition of drug administration and sample is the same as described before. The only difference is the shape of micro-patterns which is similar to those of chapter 2, a circular patterns with diameter of 30 µm and depth of 30 µm.

The Raman spectrum was obtained with a commercially available Raman microscopy system (The BioRam®, Celltool GmbH, Germany) at CellTool company (CellTool GmbH, Bernried, Germany). Raman excitation laser has a 785 nm wavelength. While the BioRam® system includes an automated stage with a standard brightfield microscope, it does not have an on-stage incubation capability, nor the possibility of simultaneous fluorescent microscopy. Therefore, we have to run two separate identical experiments, one time-lapse fluorescent microscopy and one time-lapse Raman spectroscopy. For a comparable results, we used the synchronized population.

Figure 3.7 shows the results of apoptosis detection with Raman spectroscopy. Due to technical limitation, the measurements were done only at tree time-points, before drug (t_0, black), after 3 hours (t_1, red) and after 5 hours (t_2, green). Comparing the spectra of a single cell over time shows a trend in some peaks. Movasaghia et al. [159] extracted the relevant peaks for biological and biochemical components from the literature, we have used their suggestions in defining the range of interest as the apoptosis specific wavenumbers. Here we chose these domains 864-888 cm^{-1}, 1038-1051 cm^{-1}, 1100-1131cm^{-1} which are shown in Figure 3.7.a as blue shaded areas. Some of the other peaks corresponding to the cell components, such as proteins, RNA, and nucleic acid are shown as gray shaded areas in Figure 3.7.a.

PCA scatter plot for PC-1 and PC-2 is shown on the full spectra (Figure 3.7.b) and exemplary apoptosis specific domains (Figure 3.7.c, .d). As it is shown in the PC analysis, Raman spectra can distinguish alive, early apoptosis, and late apoptosis (i.e. secondary necrotic) cells. While the cells are colored based on the time that the Raman spectra is taken, one can see that some of the cells go through the apoptosis stages much faster and already after 3 hours of adding the drug (t_1, red) show the signature of a late apoptotic cell (t_2, green). The corresponding cell morphology for these points from brightfield images confirmed that these cells had already reached a late apoptotic stage after 3 hours.

The higher PC values has also shown the possibility for separation of cells in apoptosis stages. However, PC-1 and -2 cover most of the spectra information, as it is shown by the percentage of data coverage, i.e. the percent value in parentheses of axis headers in Figure 3.7.b-d.

The results showed that Raman spectroscopy can be used as a stand alone label-free apoptosis detection technique. Using micro-well patterns assures the localization of the cells under investigation, hence enabling the automated time-lapse Raman microscopy on single cells. The limiting factor for single cell data collection is the time needed to celled an spectra per cell which now is minimum 30 seconds. This study can be used as a label free detection of cancer cells' response to chemotherapeutic drugs at single cell level. A machine learning algorithm with a well training sets for each type of cells can make the prediction even more precise. Raman Tweezers, a Raman microscopy system combined with optical

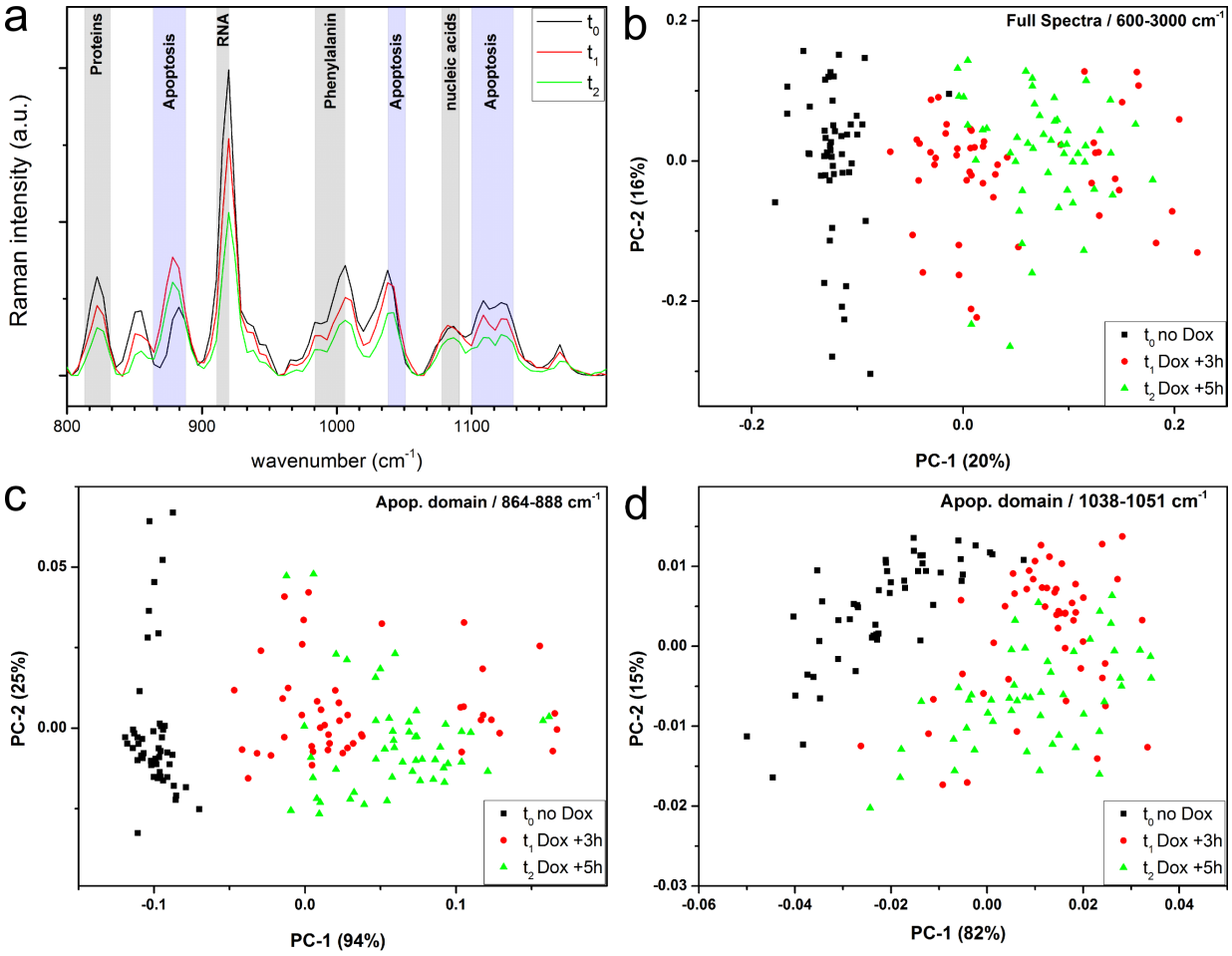

Figure 3.7: A Raman spectrum of 50 single cells is obtained at three time-points: before (t_0, black), after 3 hours (t_1, red) and after 5 hours (t_2, green) of the administration of doxorubicin. a) The biologically significant part of the spectra of an exemplary cell, the domain of apoptosis (blue shade) and other cell components (gray shade) are obtained from literature [159, 145]. The principal component analysis (PCA) of Raman spectrum is calculated and the PC-1 and PC-2 is plotted in for b) full spectra, c) spectra in range of 864-888 cm^{-1}, and d) spectra in range of 1038-1051cm^{-1}. The percentages show the part of spectrum that is used in that PC value.

tweezers, [155] can be used as an online detection system to sort and classify the cells. Next chapter introduces the optical tweezers and the possible cell sorting capabilities.

Chapter 4

Optical tweezers for cell sorting

Laser based techniques have been used in clinical context in wide range of applications. In single cell studies, an optical tweezers can be used to select and move individual cells. We used this tools to develop a lab on a chip device for single cell sorting. The single cell sorting can be used for a detailed analysis of special cells in a population. For example a drug resistant cancer cell or a non-differentiating adult stem cell.

In this chapter we introduce two aspect of laser application in biology: 1) Actuator/Detector; 2) Cell sorting. We used an optical tweezers to grab and move single cells. This was used in The first section describes the application of optical tweezers as a tool for cell adhesion detection. In the second section a drag-and-release of single cells with optical tweezers was used for a cell sorting device. We designed and fabricated a chip which integrated our micro-well arrays platform with a flow system and enables us to track hundreds of cells in parallel and at any time select and extract individual cells from the population for off-chip analysis.

We showed that an automated lift-and-release of cells with optical tweezers can be used as a label-free detection for adherence of cells in micro-well arrays. Based on this lift-and-release approach, we designed and perform the preliminary experiments on the single cell sorting device.

4.1 Optical tweezers: Manipulation and measurement at nano-scale

Laser, light amplification by stimulated emission of radiation, is an intense spatiotemporally coherent beam. The first functional laser was introduced by Maiman in 1960 [160]. The unique properties, like high intensity and monochromatic light, became a powerful tool in solid state and quantum physics. These properties with the intrinsically sterile properties of light lead to the extensive application of lasers in medical and clinical platform. Main application includes the use of intense light as a minimal damage scalpel, wound cauterization, or removal of kidney stones.

In 1970 Ashkin [161] introduced the possibility of confining and moving a micron-size particles with a laser beam. The idea of micromanipulation grow rapidly in the coming years by introducing a single beam optical trap, i.e. optical tweezers [162]. The optical tweezers can confine a micro-particle in a minimum of the potential force field. The principle of a single beam optical trap is based on a focused Gaussian laser beam, which induces balanced scattering and reflecting optical forces on a transparent spherical-particle which consequently holds it in the center of focal point of laser. An optical tweezers can have sub-nanometer resolution with forces ranging from sub-piconewton to nanonewton [163, 164]. The force measurement of optical tweezers rely on the interplay between properties of laser beam and sensitivity of detector.

The technical definition of optical tweezers refers only to the optical traps that are achieved by a single laser beam, however as it is widely common in literature we used the terms "optical tweezers" and "optical trap" interchangeably.

4.1.1 Forces and displacement in an optical tweezers

In his original paper [161] Ashkin showed that a transparent microparticle with higher refractive index than surrounding medium is pulled toward the center of a zero mode laser. This laser has a beam with a cross section profile of a single peak 2D Gaussian, which is the lowest order of transverse electromagnetic (TEM) mode called TEM_{00}. The main characteristics of an optical tweezers is defined by the mode, wavelength and intensity of laser beam, the shape and size of trapped particle, and optical characteristics of surrounding medium. An optical tweezers can be approximated with a Hookean spring with a spring constant representing the strength of electromagnetic well. The resolution and accuracy of the force and displacement measurement relies on the interplay between properties of laser beam and sensitivity of the detector.

There are two categories of optical forces on a transparent particle in the trap, scattering and gradient. Scattering forces are due to reflection of light from the interfaces which pushes the particle away in direction of light. Gradient forces are due to the changes in momentum of the light passing through the particle which pulls the spherical particle to the high intensity regions. Figure 4.1.a and .b shows the vector representation of the forces and how the resultant force guide the bead to the center of focal point. Both types of forces are present in all optical regimes and depending on the ratio of microparticle's diameter (d) to wavelength of laser (λ) an analytical calculation is available. The optical system can be in Rayleigh ($d \ll \lambda$), ray-optics ($d \gg \lambda$), or Mie ($d \approx \lambda$) regimes. Ashkin [162] showed the detailed calculation for the forces in ray-optic regime which are valid for particle diameters at least 10 times larger that the wavelength of laser ($d > 10\lambda$).

The analytical solution in Rayleigh regime is possible when assuming the particle as a dipole in inhomogeneous electric field of laser. Measuring the electromagnetic forces on the dipole [165] and the effect of gradient and scattering forces on sphere [166] results in a

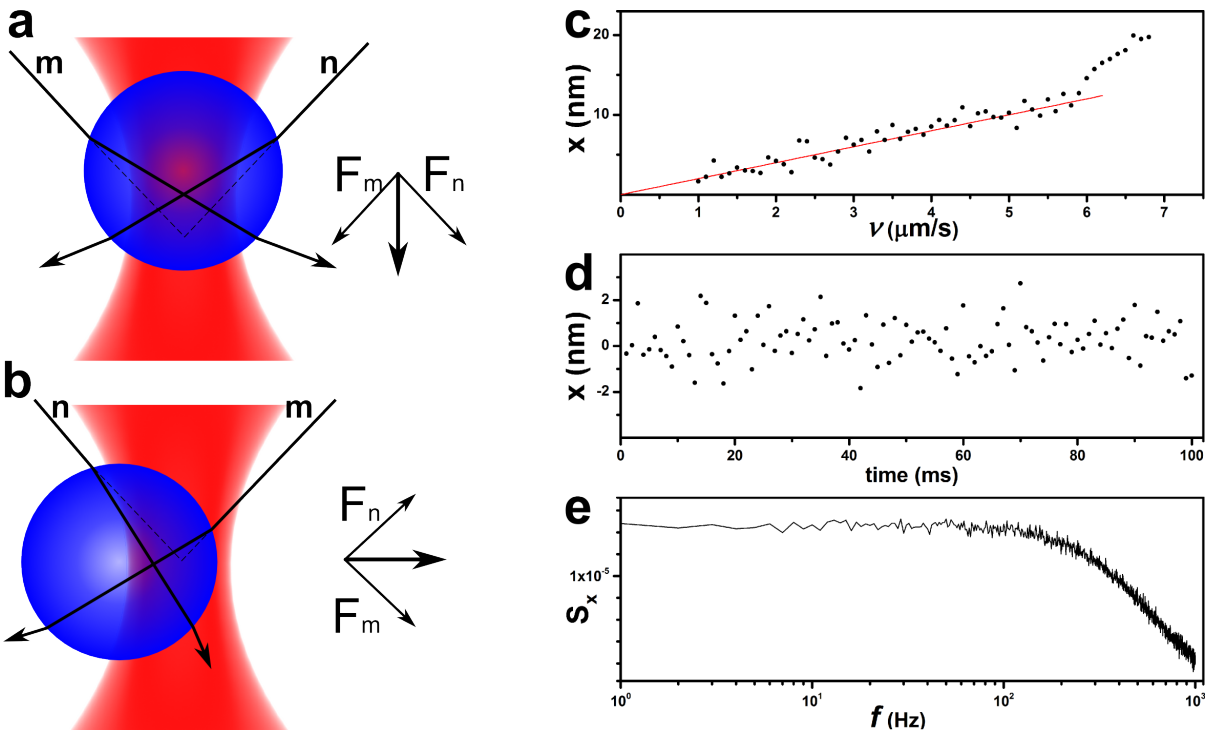

Figure 4.1: The forces in optical tweezers and the trap stiffness calibration.
In (a) and (b), the exemplary rays **m** and **n** go through the focal point of laser beam. The transparent bead deflect the rays when a) beads displaced in direction of the beam b) bead is displaced in across the beam. This results in a net force which pushed the bead back to the center of focal point (adopted from [162]). In (c), (d), and (e) the different methods for measuring the trap stiffness is shown. These are all exemplary data-points for a) a bead deflected with a known laminar flow with speed v, b) thermal fluctuation of bead in the center of trap, c) Power spectrum S_x of the Brownian motion of trapped bead.

simple Lorenz force on dipole as in Equation 4.1.

$$\vec{F} = q\left(\vec{E_1} - \vec{E_2} + \frac{d(x_1 - x_2)}{dt} \times \vec{B}\right) \tag{4.1}$$

Where the change of electric field long the dipole is $\vec{E_1} - \vec{E_2} = ((x_1 - x_2) \cdot \nabla)\,\vec{E}$ and dipole moment $\vec{p} = q(x_1 - x_2) = \alpha\vec{E}$. This leads to Equation 4.2.

$$\vec{F} = \alpha\ \nabla\left(\frac{1}{2}E^2\right) \tag{4.2}$$

For the Mie regime which the particle size and wavelength are close, Nieminen et al. developed a Matlab toolbox based on Lorenz-Mie theory [167].

While the analytical and numerical calculation is now available for an accurate computational model of a trap, the force measurement and calibration must always be done

empirically as a step before the experiment starts. The quality of optical instruments as well as environmental conditions such as temperature and electrical instability affect the shape and intensity of laser beam. For example, The minimum size of the focal point of laser in TEM_{00} mode is theoretically equals to the wavelength of the beam, however, it changes depending on optics (change in mode, divergence) or environmental distortion (temperature). The (bio-)chemical composition and temperature can also affect the refractive index of medium hence changing the gradient and scattering forces.

For empirical calibration, the optical tweezers is approximated by a Hookean spring and the trap stiffness κ is measured from the calibration. The trap stiffness sums up the effect from parameters such as NA of microscope objective, wavelength of the laser, laser power at the focus, laser-beam profile and polarization, refractive index of particle and medium, and shape and size of the particle. Several ways has been suggested to calibrate the stiffness of the trap [168, 169, 170]. The calibration can be done with one of these methods: 1) Stokes drag force. 2) Thermal fluctuations. 3) Power spectra.

1) Stokes drag force

This method records the displacement of spherical microparticle under the influence of a known laminar flow. At different speed the bead has different deflection from the center of optical tweezers which in short-distance has a linear dependency (see Figure 4.1.c). If the particle radius (r) and flow velocity (v) is known, the trap stiffness (κ) can be easily derived from the Stokes' law for frictional force shown in Equation 4.3.

$$\kappa x = 3\pi\mu dv \tag{4.3}$$

2) Thermal fluctuations

The thermal fluctuation, or Brownian motion, of the bead in a steady state condition is compensated by trap forces (see Figure 4.1.d). This equilibrium can be shown by a simple formula as Equation 4.4. This method does not need prior knowledge about the fluidic system. However, it is prone to error induced to the system from other vibrational sources or inaccuracy in positioning resulting is positional drifts.

$$\kappa = \frac{K_B T}{\langle x^2 \rangle} \tag{4.4}$$

3) Power spectra

This method investigate the characteristics of Brownian motion in frequency domain. Berg-Sørensen et al. [171] showed that the power spectra density $S_x(f)$ of a Brownian particle can be approximated by a Lorentzian as Equation 4.5

$$S_x(f) = \frac{K_B T}{2 * \pi^2 \gamma_0 (f^2 + f_c^2)} \tag{4.5}$$

where f is the frequency, $f_c = \kappa/(2\pi\gamma_0)$ is the corner frequency, and γ_0 is the friction coefficient of Brownian particle. By fitting the equation to the power spectra, corner frequency gives the trap stiffness. One important note here is the consideration for fitting algorithm. The power spectra points are distributed exponentially about the theoretical value. On the other hands, the least-square fitting algorithm assumes a Gaussian-distribution about theoretical value. Using "blocking" of data points, as suggested by Berg-Sørensen et al. [171], transforms the exponential distribution to a Gaussian distribution (see Figure 4.1). The new set of data then is fitted using least square algorithm.

All of the mentioned methods have advantages and disadvantages based on the available components on the optical setup. While drag coefficient calculation is straight forward, controlling the flow velocity and avoiding the wall effects on the bead motion need a careful microfluidic design. On the other hand the other two techniques rely on a fast and accurate detection of Brownian motion of a particle. This requires a sensitive CCD camera or four quadrant diode sensor.

The polystyrene bead is a prime candidate for a trapped particle in optical tweezers because of its shape and refractive index. It is used as a trapped object with linkers to the bio-molecules which are involved in interactions, this way the forces and displacements can be measured and applied indirectly. However, recently it was shown that some biomaterials also have similar refractive index, hence can be confined and manipulated by optical tweezers, see Table 4.1 for some examples [172]. In the next section we introduce the application of optical tweezers in biology and single cell studies.

4.1.2 Optical tweezers on biological samples

With the introduction of transparent microfluidics and single molecule studies, the optical tweezers was used to investigate cellular and molecular properties of biological samples. It has been used to move macromolecule and proteins and measure the interaction forces precisely. For example the forces and motion of myosin [173] and kinesin [174] motors was characterized by an optical tweezers. However, one always has to keep the photo-damages from laser intensity in mind. The adverse effect can be high even at some hundred mili-Watt intensity. The bio-molecules are linked to the trapped polystyrene beads to prevent the direct photo-toxicity effect from a high intensity beam.

As it was mentioned the physical properties of biomaterials (refractive index, shape, etc)

Material	η
polystyrene sphere	1.59
proteins	1.51
lipids	1.48
mitochondria	1.42

Table 4.1: Refractive index (η) of some common material in biological research.

is close to the polystyrene and can in principle be directly trapped. Recently the research studies showed that, with correct considerations, it is possible to directly trap a cell. The most prominent effect is the absorption of laser that results in heating and destroying the tissue. Water is the major absorbent medium in this system, hence avoiding the maximum absorption peaks of water reduces the heating effects. The 1064 nm and 760 nm lasers meet the minimum absorption criteria, and has been successfully used in tissues and single molecule studies [175]. The 760 nm trap showed low photo-damage in the cell and cell organelles, e.g. mitochondria [176].

Non-adherent spherical shaped cells are good candidates for a direct cell-trapping in an optical tweezers. In the next section we used MOLM-13 cells line with spherical shape and average diameter of 20µm and trapped them in an optical tweezers built on a 1064 nm laser.

4.1.3 Optical tweezers to detect the cell adherence

We used the optical tweezers to identify whether a cell is adhered to surface. The MOLM-13 cells are naturally non-adherent spherical cells. It is possible to attach MOLM-13 cells to a functionalized substrate. Here, we used Poly-L-Lysin (PLL) coated surface to immobilized cells.

Our optical tweezers is built with an Nd:YAG laser with 1064 nm wavelength (DPY 301 II OEM, Coherent, Germany) on a Zeiss 100M inverted microscope. The laser is connected to the computer through an Arduino Uno board and the whole microscopy and optical setup is controlled through a custom written program on the MicroManager platform [6]. A simplified schematic of laser beam path is shown in Figure 4.2.a. A short pass filter is set in front of camera to block the scattering signals of high-intensity laser to prevent the saturation of brightfield image. The beam expander in Figure 4.2.a increase the diameter of laser beam in-order to fill the backplane of objective which results in a better focused optical trap.

At the current state of setup, the trap cannot be calibrated, however, the qualitative measurement of strength of cell adherence is possible. We were able to trap and move polystyrene beads with diameter of 15µm, as well as, MOLM-13 cells with average diameter of 20 µm. Figure 4.2.b shows a successful trapping and moving of a single cell. The stage motion and image acquisition was automatically adjusted. The stationary bead on the left side was used here as a reference for motion of the cell.

The viability of the cells under the exposure of laser light has been tested using experimentally relevant exposure times. In four separate experiments, cells were trapped for 10 or 20 seconds every 10 or 20 minutes for total of 2 hours. A brightfield image was taken on each trapping time as well as after 2, 4 and 6 hours after exposure. The viability of the cells was measured based on their morphology. It was shown that for the experiments with 10 seconds exposures, more than 80% of cells survived. At 20 seconds exposure only $<$50% of cells were viable.

The automatic cell adherence detection which is described in chapter 2 can detect an adhered cell on a time-lapse movie. However, Brownian motion detection is not able to

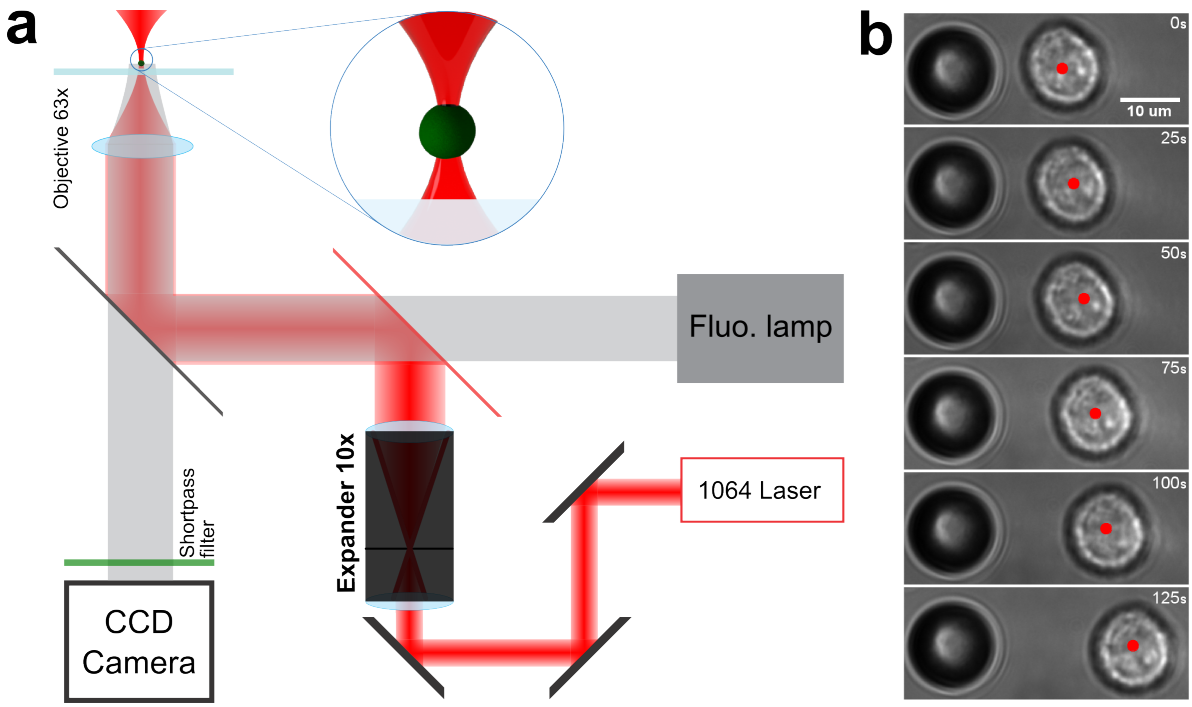

Figure 4.2: Optical tweezers' setup.
a) This is a schematic of beam path for an optical tweezers microscopy system which is coupled to a fluorescent microscope. b) Trapping and moving a cell on the glass substrate, the red circle indicate the position of laser center, Bead is used as a reference for the motion.

show the strength of adherence forces or deduce the adherence at a single time point. Here we proposed a lift-and-release of cell with optical tweezers to indicate the adherence. A non-calibrated OT can indicate whether a cell is bond to surface and do so for hundreds of cells in parallel. A fully calibrated optical tweezers is able to measure an exact force needed to detach a cell.

In the adherence experiments, we seeded the cells on a micro-well array substrate. Figure 4.3 shows the experimental steps for an automatic detection of cell adhesion in micro-wells. We have imaged the cells for 2 hours, on an uncoated and a PLL-coated substrate. Four images are taken per lift-and-release of a cell. The position of focal planes are shown in Figure 4.3 with FP#. The initial detection was done manually by comparing FP1 and FP3. If the cell is lifted up it will be out of focus in FP3 while in focus in FP1. This process can easily be integrated in an automated image analysis by correlating images of FP1 and FP3.

The percent of successful lift-up cells over time is shown in Figure 4.3 for uncoated substrate (.d) and coated substrate (.h). The error bars are the standard deviation of mean of two separate experiments. The imaging started 30 minutes after the cells were seeded on the substrate, this time is needed for the cells to settle down and transfer the

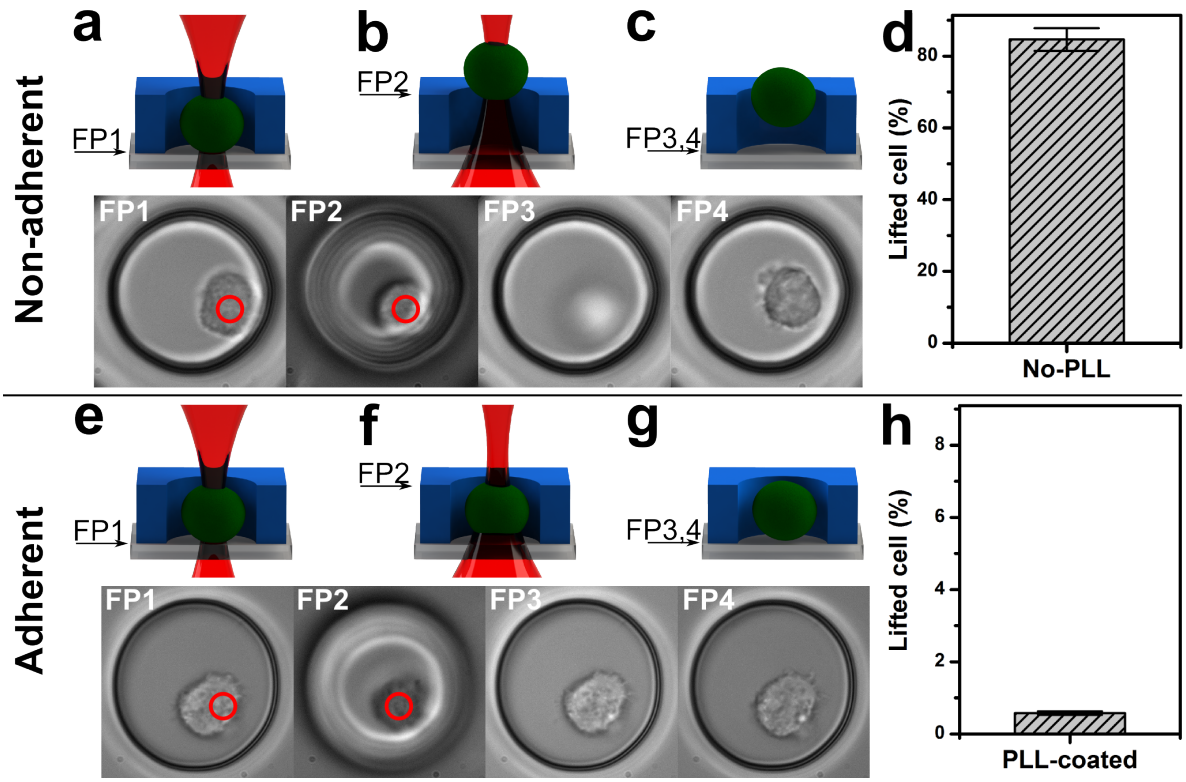

Figure 4.3: The experimental procedure for single cell adherence test with optical tweezers. Four brightfield images are taken per single cell, focal planes (FP) indicate the planes that the images are taken. FP4 is taken 4 seconds after FP3 so the cell can settle down. The procedure is as follow: Optical tweezers grabs the cell inside the micro-well (a,e), then trap moves upward (b,f) and at the highest point laser is turned off (c,g). Non-adherence cell follows the trap and falls back to the well (a,b,c) while adherent cell cannot follow the trap and stays in the same position (e,f,g). The microscopy images are exemplary bright-field images corresponding to the FPs. The results is shown as the percent of successful lift-up of cells by optical tweezers for uncoated substrate (d) and PLL coated substrate (h). The error bar is from 2 individual experiments. Notice that in (h) the y axis shows only to 9%.

sample to the microscope. The non-adherent MOLM-13 cells start to adhere to the PLL coated substrate almost immediately after seeding the cells.

Cells on uncoated substrate remain non-adherent for the whole duration of experiment with an average of 80% success rate. However, we also observed a 20% unsuccessful lift-and-release events. These events can be explained considering two aspects, one is the mis-alignment of optical tweezers on the time-lapse, two is the non-specific binding of cells to the substrate.

The mis-alignment of OT happens because of the random motion of cells in micro-well. The diameter of the micro-well (35µm) was chosen with the criteria described in chapter 1, which allows the cells to move around inside the micro-well. The random motion of cell

could push them out of the focal point of the optical trap which is a always a defined point at each scanning position of the stage. Choosing a smaller micro-well will fix this problem for a short term time-lapse studies. However, the effect of the small micro-well on the cell behavior, e.g. proliferation rate, has to be investigated.

The non-specific bindings was shown to occur for the cells that are attached to the micro-well walls (PEGDA polymers). The characteristics of these cells is that they fail in lift-and-release in one step but succeed in the following step, hence no specific binding. The non-specific binding can be either due to the surface roughness or interaction with PEG polymers. A similar affect was observed for adherent cells, it was shown that they can partially adhere to a PLL-PEG coated surfaces which has brushed PEG layers [177].

Here we have shown a simple label-free technique based on optical tweezers to detect the cell adherence characteristics. The optical tweezers could distinguished an artificially bond population from a non-adherent population. In future work, with combination of surface functionalization and optical tweezers calibration, it will be possible to quantitatively measure the development of surface proteins on the cell membrane.

4.2 Cell sorting: an integrated microfluidic system.

The time lapse study of cell decision making process with fluorescent markers provides an insight on the developmental dynamics of cells based on the tagged genes. In diagnostics and therapeutic studies it is also important to the overall composition of genes in a target cell. The cell of interest or target cell can be a cancer resistance cell, a cancer stem cell, or a differentiated stem cell. The gene composition analysis can reveal new candidate genes for drug targets. To achieve this goals, it is required to sort and collect the target cells from the microchip.

The isolation of sub-population and scarce cells from a blood sample, such as stem cells, progenitors, or white blood cells, is the first step in many diagnostic and therapeutic methods. The flow cytometry methods (e.g. FACS) is used for large populations. For single cell studies, similar methods has been developed in microfluidic devices. For example, Baret et al. [178] developed a fluorescent activated droplet sorting (FADS) microfluidic system. The single cells were trapped in droplets and sorted using dielectrophoresis forces. They were able to reach a with a speed of 300 droplet per second and accuracy of <1 per 10^4.

In recent years both active (e.g. droplet microfluidics [179]) and passive (e.g. microwell arrays [180]) microfluidic systems has been developed to sort and separate cells. Bhagat et al. [181] reviewed a variety of microfluidics devices. These devices sort the cells using the biophysical characteristics of single cells such as size, shape, surface properties, surface and bulk proteins, or polarity. Detection and classification of cells was done using both fluorescent signals and label free methods such as gravitational, electrodynamic, acoustic, or hydrodynamic forces [182]. All of the active microfluidics serially separate the cells based on a single selection signal. However, in micro-well arrays it is possible to use both spatial and temporal information to select the cells.

The optical manipulation of cells is another way to select and sort the cells.The use of

optical tweezers for cell sorting was first proposed by Buican et al. [183] soon after the first report on trapping of cells [184]. The optical forces can either push the cells to a collecting compartments [185, 186] or pick them completely with optical tweezers. One single cell drag and drop microchip was developed by Wang et al. [180]. They have successfully move two individual cell in one micro-well and diffused them together. Some other studies also used optical force to push a cell into the the constant flow on top of microwells and collect them down stream [187, 57].

Here, we have developed a chip to combine the principle of simple collecting methods from an active microfluidic channels with the temporal resolution from long term observation in micro-well arrays. This provides the possibility of further interrogations of cells off-chip or in combination with other Lab-on-chip (LoC) devices. The review by Huang et al. [188] provide an invaluable reference for combination possibility to analyze the selected cells. The off-chip analysis could range from a simple FACS analysis, to colony formation capability, or applying different condition for a reverse evolution of a stem cell. A genome sequencing in normal PCR (polymerase chain reaction) or micro-chip based PCR [189] can also be integrate at the out-put of our micro-chip for genome investigation. This bring the possibility to correlate the dynamic behavior of the cell to possible intrinsic changes on the cell not only in the fluorescently marked genes, but also on the other genes.

We have used the combination of a microfluidic system, a micro-well array, and an optical tweezers for a "cell sorting" device for long term experiments. The microfluidic has three channel with separate inlet-outlet. Figure 4.4.a shows an overview of the micro-chip design. The center channel, "culture channel", is for the long-term observation of cells and in the micro-well arrays on the substrate (see Figure 4.4.b & .c). Cells are seeded only to culture channel and captured by the micro-wells. The design of micro-wells prevent the captured cell to flow out (See simulation in chapter 1). This way a constant flow of medium can be used to initially wash away loose cells and further provide nutrients for a long term experiment.

The two side-channels, "collection channels", are used for collecting the cells and transporting them out of microfluidic system. Figure 4.4.d shows the cross section of the channels, each channel has a width of 100 µm and a hight of 70 µm. There is a hanging wall between the channels (with the width of 50 µm) which reduces the cross flow between the channels while providing a narrow opening in the bottom. This 30 µm opening is used for cell transport from the culture channel to the collection channels. An optical tweezers is used to drag-and-release the cell of interest from the micro-well into the collection channel.

We have checked the flow rate in the channels. Figure 4.5 shows an example of flow in the intersection of three channels, the fluorescent dye is used in the center channel to visualize the flow lines. The proper combination of flow rate in all the channels is essential to have a stable system for delivery and extraction of single cells. We have tested several flow-rate and concluded that the equal values with maximum flow-rate of 10 $\mu m\,min^{-1}$ for all the channels gives the best result.

The cell-sorting microfluidic device is developed as a highly integrated manipulation, detection and treatment LoC system. This device is capable of hosting cells for long-term time-lapse investigation and select the candidate cells for further off-chip investigation. All

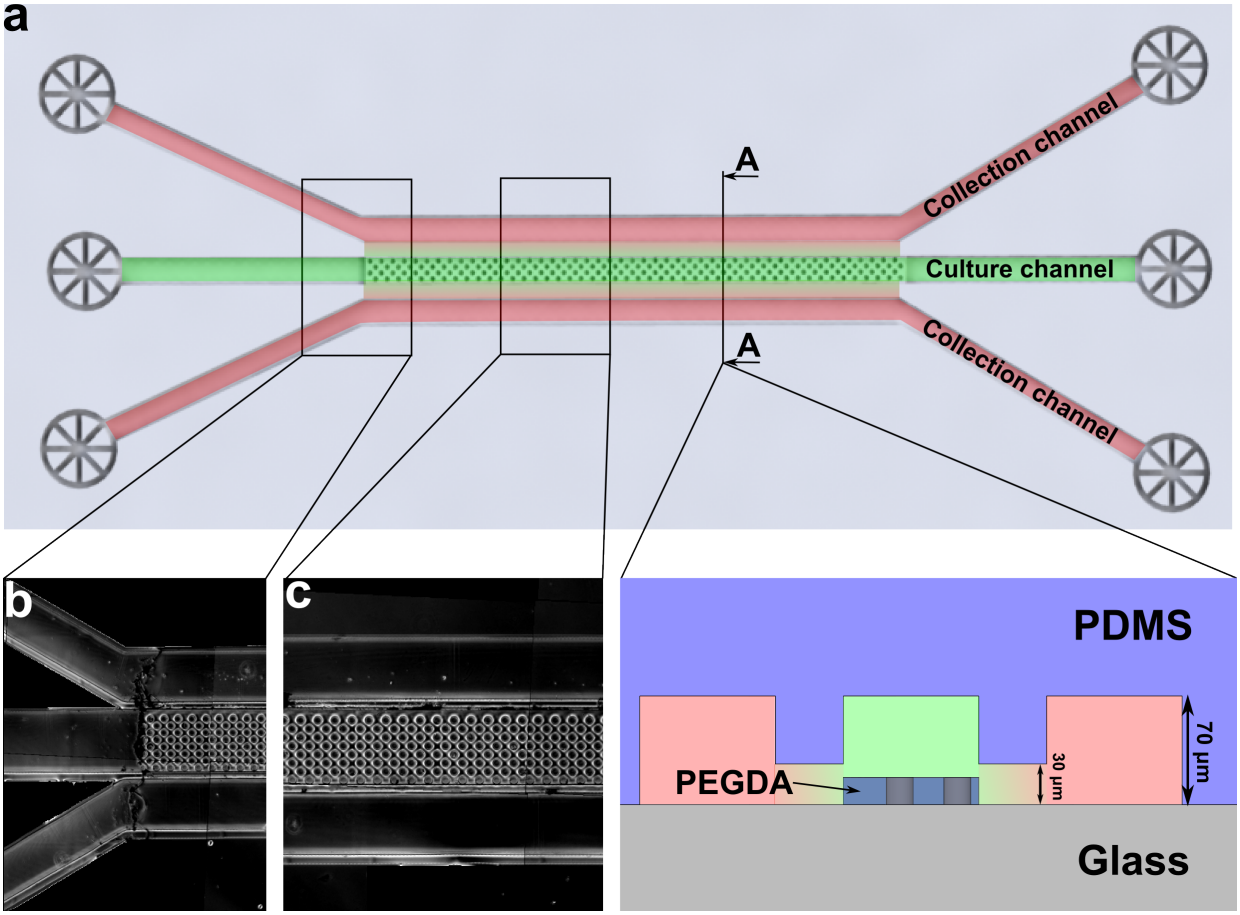

Figure 4.4: Cell sorting micro-chip.
a) A three channel microfluidic for cell sorting. The center channel (green) has micro-well substrate to hold and analyze the cells, i.e. culture channel. The two side channels (red) are separate sorting channels for two types of cells, i.e. collection channel. Cells are selected based on fluorescent signal, Raman signal (as in 3.5.4), or label-free motion technique (as in 2) and moved using optical tweezers. b) Phase contrast image of junction of three channels. c) Phase contrast image of the middle part of the channels showing the center patterned channels and two sorting side channels. d) Cross section of micro-channels. The half walls separates the channels to reduce the possibility that a sorted cell goes back to the micro-wells down stream the channel.

the observation, detection, and selection process can be automatized hence minimizing the user involvement and increasing the single cell data analysis. This microfluidic system has a promising capability to study the dynamics and genetics of a drug resistant cancer cell and the final selection mode for a PCR analysis.

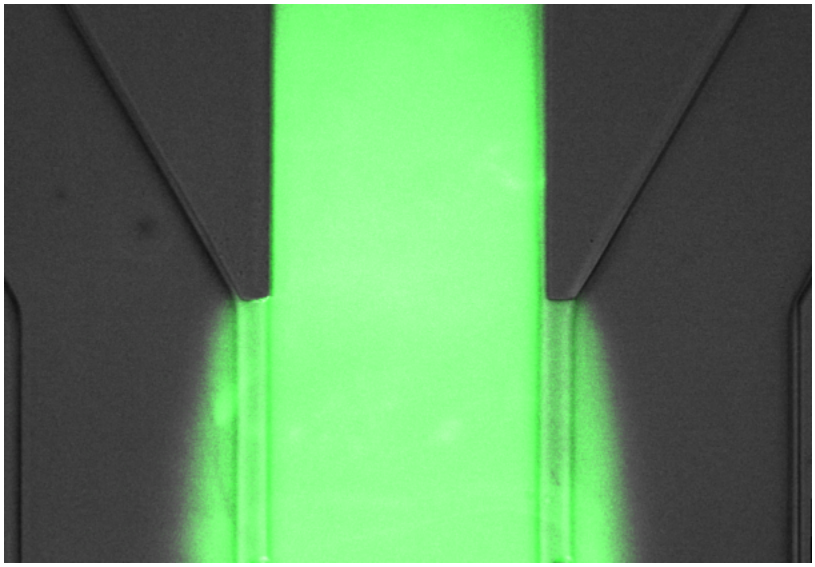

Figure 4.5: The experimental flow profile inside the cell sorting LoC device. The flow speed in the center channel and side channels are the same. The green fluorescent dye is added in the center channel for visualization.

Appendix A

Published paper

Marker-Free Detection of Progenitor Cell Differentiation by Analysis of Brownian Motion in Micro-wells

Farzad Sekhavati, Max Endele, Susanne Rappl, Anna-Kristina Marel, Timm Schröder, and Joachim O. Rädler

published in
Integrative Biology, 2015(7), pp.178—183

Integrative Biology

PAPER

View Article Online
View Journal | View Issue

Cite this: *Integr. Biol.*, 2015, 7, 178

Marker-free detection of progenitor cell differentiation by analysis of Brownian motion in micro-wells†

Farzad Sekhavati,[a] Max Endele,[b] Susanne Rappl,[a] Anna-Kristina Marel,[a] Timm Schroeder[b] and Joachim O. Rädler*[a]

Received 7th July 2014,
Accepted 27th November 2014

DOI: 10.1039/c4ib00158c

www.rsc.org/ibiology

The kinetics of stem and progenitor cell differentiation at the single-cell level provides essential clues to the complexity of the underlying decision-making circuits. In many hematopoietic progenitor cells, differentiation is accompanied by the expression of lineage-specific markers and by a transition from a non-adherent to an adherent state. Here, using the granulocyte-macrophage progenitor (GMP) as a model, we introduce a label-free approach that allows one to follow the course of this transition in hundreds of single cells in parallel. We trap single cells in patterned arrays of micro-wells and use phase-contrast time-lapse movies to distinguish non-adherent from adherent cells by an analysis of Brownian motion. This approach allowed us to observe the kinetics of induced differentiation of primary bone-marrow-derived GMPs into macrophages. The time lapse started 2 hours after addition of the cytokine M-CSF, and nearly 80% of the population had accomplished the transition within the first 20 h. The analysis of Brownian motion proved to be a sensitive and robust tool for monitoring the transition, and thus provides a high-throughput method for the study of cell differentiation at the single-cell level.

Introduction

Single-cell studies are increasingly being used in the biological and biophysical characterization of living cells. In contrast to population studies, which uncover only the average behavior of many cells, single-cell studies examine the underlying dynamics of the responses of individual cells to external triggers.[1,2] Such experiments shed light on phenomena ranging from early signaling and responses at the level of protein synthesis to cell division and cell fate choices.[3] Single-cell analysis has also revealed phenotypic heterogeneity in isogenic populations.[4,5] Stem cell fate decisions are prominent examples of heterogeneous system responses. The unique ability of stem cells to give rise to many kinds of differentiated cells makes them prime candidates for regenerative medicine. Thus, single-cell analysis of hematopoietic stem cell (HSC) decision-making promises to further our understanding of the regulatory factors underlying fate decisions, with potential impact on clinical medicine.

In recent years it has been recognized that, for single-cell analysis of stem cells in particular, there is a need for microscopy platforms that allow isolated cells to be cultured under conditions that enable precise control over the mechanical and chemical properties of their micro-environment.[3,6] This is because population studies have shown that the signaling molecules present[7] and the mechanical properties of the environment[8,9] can have a marked impact on stem-cell fates.[10] Microfluidic devices offer a highly accurate and flexible platform for this purpose, allowing both cell screening and micro-patterning.[11,12] However, for most primary cells, and for non-adherent cells generally, isolation and tracking is difficult and time-consuming.[13,14] Various microfluidic approaches have been developed to hold cells in place and facilitate long-term experiments. Active systems use *e.g.* hydrodynamic forces to create single-cell traps at the ends of microchannels[15] or cell-sized, semi-circular barriers,[16] while passive systems such as micro-arrays of 3D micro-wells topologically trap the cells on the surface.[17,18] In such devices, single-cell observations require the availability of fluorescent markers for the properties of interest. Fluorophore instability, bleaching, background noise and phototoxicity limit the application of fluorescence microscopy.[6] A label-free technique, which bypasses these limitations, is therefore highly desirable for time-lapse imaging of cells.

Here, we introduce a novel approach to follow the fate of isolated cells over time without the need to label them. The technique monitors the Brownian motion of single non-adherent

[a] *Faculty of Physics and Center for NanoScience, Ludwig-Maximilians-University, Munich, Germany. E-mail: raedler@lmu.de; Fax: +49-89-2180-3182; Tel: +49-89-2180-2438*
[b] *Department of Biosystems Science and Engineering (D-BSSE), ETH Zurich, Mattenstrasse 26, 4058 Basel, Switzerland*

† Electronic supplementary information (ESI) available. See DOI: 10.1039/c4ib00158c

cells to determine the timepoint at which they attach to the surface. Brownian motion of spherical objects is well understood and has been used as a sensitive probe for particle–substrate interaction in the case of microbeads.[19–21] We used image-based fluctuation analysis to resolve the heterogeneity of adherence transition times at the single-cell level. Cells are confined to arrayed micro-wells and their motion is tracked over time using phase-contrast microscopy. As a proof of principle, we investigated the differentiation of granulocyte-macrophage progenitors in response to the cytokine M-CSF. During hematopoiesis, multipotent HSCs give rise to several lineage-restricted progenitors, which ultimately produce all the different mature blood-cell types.[22] Thus the bipotent granulocyte-macrophage progenitor (GMP) population gives rise to the monocyte/macrophage (M) and the granulocyte (G) lineages.[23] *In vitro*, GMPs can be instructed to adopt the Ms or Gs fate by exposure to the cytokines macrophage colony-stimulating factor (M-CSF) or granulocyte colony-stimulating factor (G-CSF), respectively.[24] Of these three types of cells, Ms are adherent while GMPs and Gs are non-adherent. We compare the timing of adherence of macrophages with the up-regulation of Lysozyme 2 (Lyz2), F4/80, and MacI, myeloid commitment/differentiation markers. We find that the adherence transition precedes the up-regulation of MacI, Lyz2 and F4/80 expression, hence following the general behavior observed by Rieger *et al.*[24] We demonstrate that the label-free technique is capable of robustly detecting the adherence transition, and discuss its potential for studying the kinetics of differentiation.

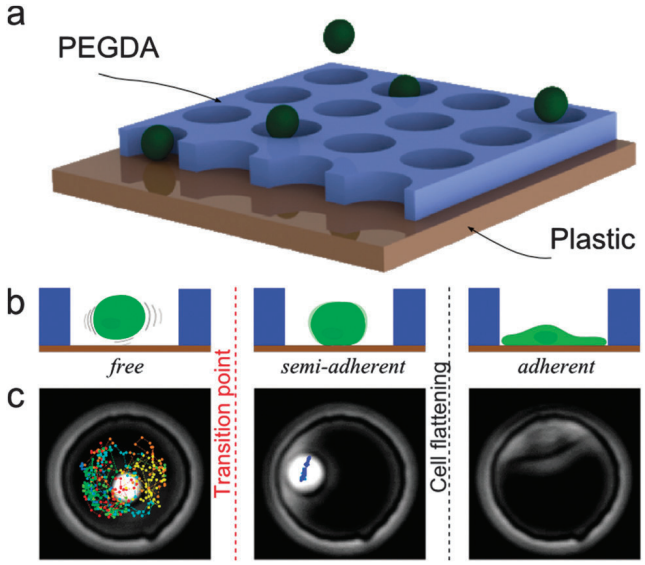

Fig. 1 (a) Schematic view of cells settling into micro-wells under gravity. (b) Schematic depiction of the three states of adherence: freely mobile, semi-adherent and adherent. (c) Corresponding phase-contrast image of a non-adherent GMP which differentiates into an adherent macrophage. The dots indicate the position of the center of cell over a period of 24 h (elapsed time is coded in color from red to blue; see Fig. 2c). The transition point is the time at which the cell enters a semi-adherent state.

Results

Micro-structure fabrication

We fabricated micro-structured patterns on a tissue-culture plastic (TCP) substrate, which was then attached to the underside of a bottomless slide (I-Luer sticky slide; ibidi, Germany) to form the floor of a channel with walls 400 μm high. The pattern consists of an array of 3D micro-wells whose walls are 12 μm high. We tested different well diameters ranging from 15 to 50 μm and selected for the best single-cell coverage and maximum space for free diffusion. For GMPs (mean diameter 15 μm), micro-wells with a diameter of 35 μm were resulted in 90% viability and 60% single coverage. The micro-array pattern is fabricated from cell-repelling PEGDA polymer on a tissue culture plastic substrate.[25] Each slide carries an array of 45 × 750 micro-wells. Compared to conventional cell-culture flasks, the limited depth of the channel and the thinner layer of medium on top of the cells results in reduced background fluorescence, while still supplying enough nutrients for up to two days.

Cells in micro-wells

GMPs carrying an EGFP-tagged Lyz2 gene (see Methods) were induced to differentiate into macrophages by adding M-CSF as previously described.[24] Cells were pipetted into the channel and allowed to settle into the micro-well arrays (Fig. 1a). Three distinct states in the differentiation of GMPs into macrophages could be distinguished: a freely diffusive state subject to Brownian motion, a semi-adherent state, and a fully adherent state (Fig. 1b).

Non-adherent cells diffuse freely, ranging over the whole area of a micro-well. Semi-adherent cells attach to the surface and become immobile. Fully adherent cells spread out on the substrate and display active, crawling motion. Fig. 1c shows phase-contrast images of a representative cell going through each of the three states. For the purpose of differentiation detection, we followed the positions of cells until just before division or until the transition to the fully adherent state. While the former breaks the symmetry in label-free detection, the latter is characteristic for a late stage of differentiation. The adherent state was observed to confirm that the cell had successfully reached the fully developed macrophage state, which could occur either in the same generation or after division.

Most of the cells in the non-adherent state ranged over the whole well area. In others, a tendency to remain close to the wall was observed. These latter cells show less difference in motion between the two states, but the switch to the adherent state is still distinguishable.

Time-lapse imaging

Time-lapse microscopy was performed using an inverted Axiovert 100M Zeiss microscope, taking advantage of the out-of-focus phase-contrast image, in which cells have bright centers. This accelerates cell recognition in image processing. Each sample is imaged at 3 min intervals for 24 h, producing a time-lapse sequence of cell motion (Fig. 2a). An interval of 3 min allows a cell of 15 μm diameter to be displaced by ~3 μm, which equals the ~5 pixel resolution in our microscopy setup.

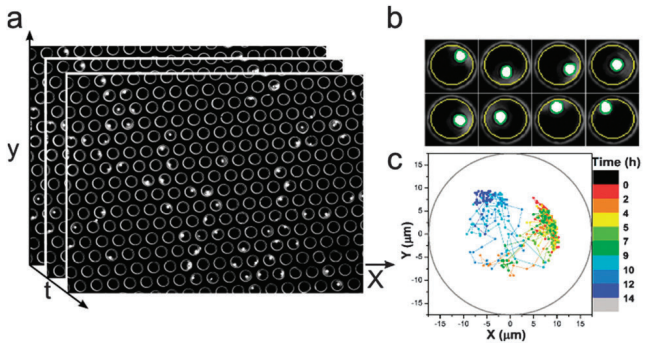

Fig. 2 (a) Three frames from a time-lapse sequence of phase-contrast images of a single field at 10× magnification. The field contains ~250 wells and 50 single cells. (b) Selected frames from a time-lapse sequence of phase-contrast images of a single well. Contours are detected automatically, the yellow contour indicates the micro-well and green contour indicates the center of the cell. (c) Trajectory of the center of cell over a period of 14 h, (elapsed time coded in color as indicated), This cell adheres to the surface after around 12 h.

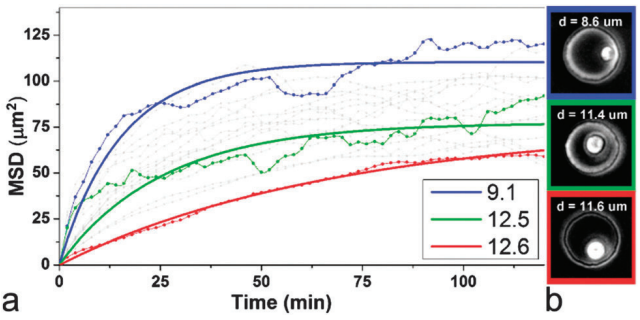

Fig. 3 (a) Mean square displacement of cell center. The dots are experimental points and the solid line shows the fit from the explicit expression (See ESI†). The different plateau values reflect differences in cell diameter. (b) The corresponding phase contrast images of cells for solid lines are shown. Diameters calculated from fitted curves are shown in the inset and the diameter calculated from image calibration is shown on the corresponding image.

Cell centers were tracked with an in-house ImageJ[26] plug-in. The software locates the micro-well array and automatically tracks the center of the cell until cell division or differentiation. For more details of the recognition algorithm see the ESI.† Fig. 2b shows an example of one cell in a micro-well (red) and the cell contour (green) as detected by the software. Fig. 2c is the resulting trajectory of the center of the cell. All tracking data were processed simultaneously, decreasing the time required for analysis.

Confined Brownian motion in micro-wells

We used the mean square displacement (MSD) of cell position to characterize Brownian motion in confinement. As shown in Fig. 3, the plot of MSD *vs.* time is linear at short time-scales, indicating free diffusion with a defined diffusion coefficient. In the case of confinement, as with cells in micro-wells, the MSD reaches a plateau value at large time-scales. As explained in more detail in the ESI,† we used an explicit expression for the MSD for 2D diffusion in a circular confinement.[27] The plateau value (P) in this case is given by $P = L^2/4$, where L denotes the clearance $L = d_{\mathrm{well}} - d_{\mathrm{cell}}$ between a cell with diameter d_{cell} and the wall of a micro-well with diameter d_{well}.

Fig. 3a shows the MSD for 10 individual GMPs exhibiting the characteristic shape of MSD for confined Brownian motion with the plateau value corresponding to the clearance. Three individual MSDs shown in color are compared to the theoretical expression (fits shown as lines). The cell diameters derived from the plateau of the MSD graphs (inset of Fig. 3a) and the images (values in Fig. 3b) are compatible with each other, as the out-of-focus image shrinks the apparent diameter of the cells, which accounts for the difference between the two values.

Transition point from non-adherent to adherent state

The transition from the non-adherent to the adherent state serves as a marker for the timepoint of GMP differentiation. To detect it, we monitored the Brownian displacement of cells

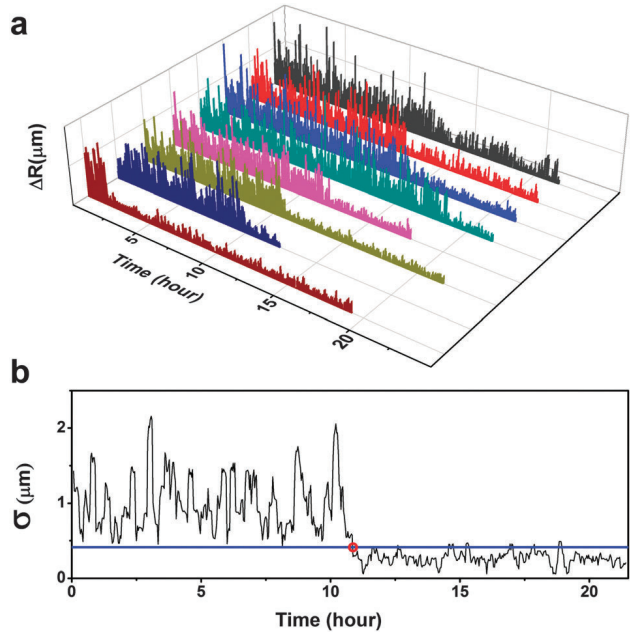

Fig. 4 (a) Graph of cell displacement *vs.* time for a set of 8 single cells, showing how a non-adherent GMP cell differentiates into an adherent macrophage. (b) Evolution of the local standard deviation σ over a rolling time window of 5 frames.

between successive frames ($\Delta R = |R_{i+1} - R_i|$) (Fig. 4a). This displacement depends on the diffusion coefficient and the physical constraints on motion. A non-adherent cell diffuses freely within the well, and thus shows a larger displacement per unit time than adherent cells, which are no longer subject to Brownian motion. Fig. 4a shows representative displacement records for 8 cells and the difference between the non-adherent state in the beginning and the adherent state at the end. For high-throughput parallel investigation of single cells, it is important that this transition point be automatically detectable.

The standard deviation of displacement over a rolling time-window of 5 frames, σ_5, was used for automatic determination of the transition point. The standard deviation σ is an indicator

of the degree of variation in the motion of a particle over the course of the time-window. A threshold value was chosen in such a way that σ_5 value drops below it after adherence. This value is manually chosen for one cell and used for the whole experiment. The time-point at which σ persistently drops below this threshold is taken as the transition point (red circle in Fig. 4b). Monitoring of the persistence of the transition to the low-motion regime permits one to distinguish the actual transition to adherence from short-term fluctuations in Brownian motion.

The cumulative sum (cusum) algorithm was used to confirm detection of the transition point. The cusum algorithm checks the global behavior of a system at each time-point and reports if there is a persistent regime change in the system.[28,29] The algorithm yields transition points in agreement with the values obtained by the standard deviation approach. Both the cusum and standard deviation algorithm are described in detail in the ESI.†

Heterogeneity in time to adherence

Differentiation of GMPs shows stochastic dynamics,[24,30] with each individual cell behaving differently (*e.g.* Fig. 4a). With the help of micro-well arrays we are able to capture and analyze the behavior of many cells in parallel. The transition point detection technique was used to identify the adherence of 789 cells in parallel. This represents a physical marker of differentiation of non-adherent GMPs into adherent macrophages. Fig. 5a shows the temporal distribution of single-cell adherence over a period of 30 h. All the cells were cultured under the same conditions. Monitoring began 4 h after addition of M-CSF to the progenitors. Around 40% of cells were adherent by the start of imaging. The number of adherence events then drops exponentially with time, and 80% of the cells have adhered to the TCP substrate prior to the first division.

The time course of differentiation was investigated *via* the onset of expression of the EGFP-tagged lyz2 signal as well as the presence of MacI and F4/80 antibody markers. Fluorescent images were analyzed by setting fluorescence thresholds for each marker and counting of the number of MacI and F4/80 positive and Lyz2-GFP expressing cells respectively. Fig. 5b shows the percentage of adherent cells (black), together with the time course of MacI positive (red), Lyz2-expressing (green), and F4/80 positive (blue) cells over a period of 48 h. It can be clearly seen that Lyz2 and F4/80 expression follows the expression of MacI. In contrast most adherence events occur slightly before MacI expression. The kinetics of the increase of total adherence, however, is weaker than the steep increase of MacI expression. For this reason we show the single cell correlations in more detail. Fig. 5c shows the correlation between the adherence timepoints and the onset of the differentiation markers for all cells individually. Again there is a clear order in the expression of the differentiation markers, while their correlation with the adherence time points is weak. Adherence typically occurs before the onset of the differentiation markers (as seen by the fact that most data points fall above the dashed line indicating the isochronic events). However, there are individual cells that show MacI or even Lyz2 expression before the onset of adherence.

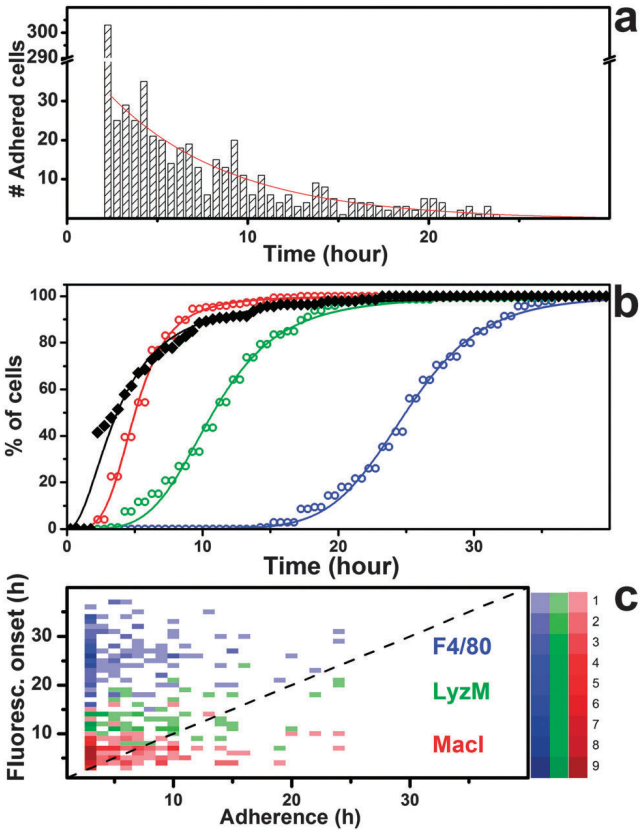

Fig. 5 (a) Histogram of the number of adherence transitions in the time course of GMPs differentiation into macrophages (data are from 789 single cells), red line shows a first order exponential fit to the data. (b) Percent of cells that adhered (black) and percent of cells that exhibited MacI (red), LzyM (green), and F4/80 (blue) fluorescent signal *versus* time. (c) Correlation between the timepoint of cell adherence and the onset of the fluorescent signals. The dashed line indicates simultaneous events. The color intensity map indicates the number of cells.

Discussion

Our study demonstrates that arrays of micro-wells enable single-cell analysis of the transition from a non-adherent to an adherent state utilizing Brownian motion as reporter. GMPs exhibit heterogeneity in the timing of both the adhesion transition as well as differentiation at the single-cell level. Rieger *et al.*[24] previously observed by manual cell tracking and classification of adherence that the transition to the adherent state precedes up-regulation of the Lyz2 marker protein in most cases. Our study reproduces these data quantitatively. In contrast to manual evaluation, our unsupervised approach allows for high temporal resolution and increased statistical accuracy of the adhesion time point. In addition we observe the temporal sequences of differentiation markers MacI, Lyz2 and F4/80. However, the correlation of these markers with the time-point of adherence is weak. Clearly adhesion is an early indicator of differentiation. Yet, the statistics of adherence events does not seem to strictly depend on the stage of differentiation. Hence the molecular changes at the cell surface that allow for adhesion do not seem to be directly timed within the differentiation process. In future studies with surface functionalized micro-wells more refined

adhesion studies can be carried out. Single-cell analysis of Brownian motion therefore provides a versatile label-free method for high-throughput detection of the adherence transition. In particular, in future work the micro-wells could be functionalized with specific antibodies in order to detect the expression of surface molecules and selectively modify adherence of cells to the micro-well surface. In this case, time-resolved studies on single cell surface protein expression could be carried out without the adverse effects of intense illumination for fluorescence imaging. The time interval chosen for phase-contrast imaging in our study was several minutes, but could be further reduced. Potentially, Brownian motion analysis is capable of resolving single molecule binding as shown by Wong *et al.* for latex particles.[31] Hence, single-cell adhesion arrays open up the possibility of single-surface-molecule studies on living cells for protein and membrane characterization[31–33] and quantitative evaluation of numbers of adhesion sites. In principle, the only limitation on the observation time in our approach is the point of cell division. We believe that the highly parallel analysis of single cells by monitoring of Brownian motion is a powerful, high-throughput, label-free method, which is particularly promising for the time-resolved investigation of differentiation and the detection of changes in cell-surface properties of non-adherent cells.

Methods

Device fabrication

Our microfluidics devices are based on inert PEGDA (polyethyleneglycol diacrylate).[34] The template for the micro-well array is fabricated on a standard plastic tissue-culture (TCP) foils, which is attached to the underside of an I-Luer sticky slide (ibidi, Munich, Germany). The slide as supplied is patterned with a cut-out 400 μm deep channel that can be accessed from each end. The attached template thus serves as the floor of the channel.

The fabrication process has been described previously.[25] In short, the PDMS precursor is mixed with curing agent at a 10 : 1 (Sigma-Aldrich) ratio. The mixture is degassed for 15 min and then poured onto a patterned silicon wafer. After a subsequent degassing step for 15 min, PDMS is cured for ~3 h at 50 °C in an oven. The PDMS mold is peeled from the wafer and cut along the structures to form an open network. PDMS and TCP substrate are exposed to argon plasma for 30 sec, then brought into contact with each other. A drop of PEGDA polymer (polymer solution containing 2% of photoinitiator 2-hydroxy-2-methylpropiophenone (v/v) (Sigma-Aldrich, Germany)) is placed at the open end of the PMDS mold. The empty space of the mold is filled with PEGDA by capillary force-induced flow. The polymer is then cured under UV light for 15 min. The PDMS mold is removed and the patterned PEGDA substrate is cured overnight at 50 °C. The substrate is then sonicated in ethanol for 10 min, followed by a 10 min sonication in deionized water. Afterwards, it is blow-dried and attached to the ibidi I-Luer sticky slide and stored under sterile conditions.

Cell preparation

FACS purification of GMPs[23] from LysM:EGFP mice[35] was performed as described.[24] Briefly, femora, tibiae, humeri, hip bones and vertebrae were dissected from 8- to 12-week-old mice, crushed in ice-cold 2% FCS/PBS, and cells were isolated by passage through a 40 μm filter (BD). All experiments were performed according to Swiss federal law and institutional guidelines of ETH Zuerich and approved by local animal ethics committee of Basel-Stadt (license number 2655).

For erythrocyte lysis, cells were resuspended in ACK buffer (Lonza) for 2 min. Cells were then stained with biotinylated antibodies against lineage-specific markers (B220, CD3e, CD19, CD41, CD11b, Gr-1, Ter119 (all eBioscience)) followed by incubation with streptavidin-coated magnetic beads (Roth). After magnetic depletion of labeled lineages, cells were stained with streptavidin-APC-eFluor780, c-kit-PE-Cy7, CD34-eFluor660 (all eBioscience), Sca-1-Pacific Blue (Biolegend) and CD16/32-PE (BD) for at least 30 min on ice. Cell sorting was done on a FACSAriaIII (Becton-Dickinson). Sorted GMPs were resuspended in SFEM (Stem Cell Technologies) containing 20 μg ml^{-1} of M-CSF, 10 ng ml^{-1} F4/80 and 10 ng ml^{-1} MacI after markers. Time-lapse imaging was initiated 2 h after sorting and addition of cytokine, this time is necessary for transportation, seeding cells into micro-well arrays, and preparation of image acquisition setting.

The microscopy slide incubated at 37 °C in an ibidi heating system chamber with 5% CO_2 and high humidity (ibidi, Munich, Germany). The chamber is mounted on an inverted microscope and a phase-contrast image is taken every 3 min and a fluorescent image every 3 h. Image acquisition is programmed to take a fluorescence picture of a subset of positions for each interval of phase-contrast imaging. Hence, we have fluorescent data at every time-point.

Acknowledgements

We thank Christian Meggle for developing the image processing software. This work was funded by the Deutsche Forschungsgemeinschaft (DFG) *via* SFB1032, the Nanosystems Initiative Munich (NIM) Excellence Cluster, the International Doctorate Program in NanoBioTechnology (IDK-NBT), and the Graduate School of Quantitative Biosciences Munich (QBM).

References

1 P. S. Hoppe, D. L. Coutu and T. Schroeder, *Nat. Cell Biol.*, 2014, **16**, 919–927.
2 T. Schroeder, *Nature*, 2008, **453**, 345–351.
3 D. G. Spiller, C. D. Wood, D. A. Rand and M. R. H. White, *Nature*, 2010, **465**, 736–745.
4 M. A. Walling and J. R. E. Shepard, *Chem. Soc. Rev.*, 2011, **40**, 4049–4076.
5 K. Chung, C. A. Rivet, M. L. Kemp and H. Lu, *Anal. Chem.*, 2011, **83**, 7044–7052.
6 S. Kobel and M. Lutolf, *Biotechniques*, 2010, **48**, ix–xxii.

7 C. J. Flaim, D. Teng, S. Chien and S. N. Bhatia, *Stem Cells Dev.*, 2008, **17**, 29–39.
8 I. Kurth, K. Franke, T. Pompe, M. Bornhäuser and C. Werner, *Integr. Biol.*, 2009, **1**, 427–434.
9 J. M. Karp, J. Yeh, G. Eng, J. Fukuda, J. Blumling, K.-Y. Suh, J. Cheng, A. Mahdavi, J. Borenstein, R. Langer and A. Khademhosseini, *Lab Chip*, 2007, **7**, 786–794.
10 A. J. Engler, S. Sen, H. L. Sweeney and D. E. Discher, *Cell*, 2006, **126**, 677–689.
11 X. Mu, W. Zheng, J. Sun, W. Zhang and X. Jiang, *Small*, 2013, **9**, 9–21.
12 H. Yin and D. Marshall, *Curr. Opin. Biotechnol.*, 2012, **23**, 110–119.
13 K. D. Kokkaliaris, D. Loeffler and T. Schroeder, *Curr. Opin. Hematol.*, 2012, **19**, 243–249.
14 T. Schroeder, *Nat. Methods*, 2011, **8**, S30–S35.
15 A. C. Rowat, J. C. Bird, J. J. Agresti, O. J. Rando and D. A. Weitz, *Proc. Natl. Acad. Sci. U. S. A.*, 2009, **106**, 18149–18154.
16 S. L. Faley, M. Copland, D. Wlodkowic, W. Kolch, K. T. Seale, J. P. Wikswo and J. M. Cooper, *Lab Chip*, 2009, **9**, 2659–2664.
17 H. Kim, R. E. Cohen, P. T. Hammond and D. J. Irvine, *Adv. Funct. Mater.*, 2006, **16**, 1313–1323.
18 V. Lecault, M. Vaninsberghe, S. Sekulovic, D. J. H. F. Knapp, S. Wohrer, W. Bowden, F. Viel, T. McLaughlin, A. Jarandehei, M. Miller, D. Falconnet, A. K. White, D. G. Kent, M. R. Copley, F. Taghipour, C. J. Eaves, R. K. Humphries, J. M. Piret and C. L. Hansen, *Nat. Methods*, 2011, **8**, 581–586.
19 D. C. Prieve and N. A. Frej, *Langmuir*, 1990, **6**, 396–403.
20 J. Raedler and E. Sackmann, *Langmuir*, 1992, **8**, 848–853.
21 V. Heinrich, W. P. Wong, K. Halvorsen and E. Evans, *Langmuir*, 2008, **24**, 1194–1203.
22 S. H. Orkin and L. I. Zon, *Cell*, 2008, **132**, 631–644.
23 K. Akashi, D. Traver, T. Miyamoto and I. L. Weissman, *Nature*, 2000, **404**, 193–197.
24 M. M. A. Rieger, P. P. S. Hoppe, B. B. M. Smejkal, A. C. Eitelhuber and T. Schroeder, *Science*, 2009, **325**, 217–218.
25 A.-K. Marel, S. Rappl, A. Piera Alberola and J. O. Rädler, *Macromol. Biosci.*, 2013, **13**, 595–602.
26 M. D. Abramoff, P. J. Magalhaes and S. J. Ram, *Biophotonics International*, 2004, **11**, 36–42.
27 T. Bickel, *Phys. A*, 2007, **377**, 24–32.
28 E. S. Page, *Biometrika*, 1954, **41**, 100–115.
29 G. A. Barnard, *J. R. Stat. Soc. Ser. B-Stat. Methodol.*, 1959, **21**, 239–271.
30 D. Dingli, A. Traulsen and J. M. Pacheco, *Cell Cycle*, 2007, **6**, 461–466.
31 W. P. Wong, V. Heinrich and E. Evans, *Mater. Res. Soc. Symp. Proc.*, 2004, **790**, P5.1.1.
32 A. Kusumi, Y. Sako and M. Yamamoto, *Biophys. J.*, 1993, **65**, 2021–2040.
33 A. Sonnleitner, G. J. Schütz and T. Schmidt, *Biophys. J.*, 1999, **77**, 2638–2642.
34 A. Khademhosseini, J. Yeh, S. Jon, G. Eng, K. Y. Suh, J. A. Burdick and R. Langer, *Lab Chip*, 2004, **4**, 425–430.
35 N. Faust, F. Varas, L. M. Kelly, S. Heck and T. Graf, *Blood*, 2000, **96**, 719–726.

Supplementary Information:

Marker-Free Detection of Progenitor Cell Differentiation by Analysis of Brownian Motion in Micro-Wells

Optimization of micro-well dimension

We chose the diameter of micro-wells in order to minimize double occupancy of micro-well and at the same time maximize space for free diffusion inside the well. A set of wells with diameters of 15 to 50 was examined. We concluded that 35 µm diameters of the well is optimal for GMP cell line. In these micro-wells, cells showed 90% viability and 60% occupancy of single-cell per well. Given an average diameter of 16 for GMPs the clearance between cell diameter and well diameter (L) is 19 µm.

Mean square displacement (MSD)

Mean square displacement is commonly used to characterize random motion of a particle and the diffusion coefficient and confinement. In our setup, there is no flow and gravitational forces cancel random motion in z direction in our time-intervals. In our analysis, we have decoupled the z-motion from the random motion in x and y, while, cells exhibit an almost constant distance from the substrate at all time. Hence, as in many other studies on colloids at the surface, we can treat the x-y motion as effective 2D diffusion. The MSD for free diffusion in 2D is given by:

$$<|\vec{x}|^2>=4Dt \qquad \text{SI.Eq.1}$$

Confinement affects the diffusion of particle[1], we have used the MSD equation derived by Bickel [2] for 2D diffusion in circular domain. Since the diameter of cell is comparable to diameter of micro-well, we have substituted the diameter of micro-well with the clearance L (Fig.SI.1).:

$$<|\vec{r}|^2>=\frac{L^2}{4}\left(1-8\sum_{\mathrm{m}=1}^{\infty}\frac{1}{\alpha_{1\mathrm{m}}^2\left(\alpha_{1\mathrm{m}}^2-1\right)}\exp\left\{-4\alpha_{1\mathrm{m}}^2\frac{Dt}{L^2}\right\}\right) \qquad \text{SI.Eq.2}$$

Here $\alpha_{\mathrm{nm}}^2>0$ mth root of Bessel prime function, $J_n'(\alpha_{nm})=0$. We have used the first two expression of summation and fitted the MSD values from experiment with the equation SI.Eq.2. D is the free diffusion coefficient, from Einstein relation for spheres:

$$D=\frac{K_bT}{6\pi\eta r} \qquad \text{SI.Eq.3}$$

assuming T=37℃ and approximating viscosity of medium with water at 37℃, $\eta=0.7225\,\mathrm{mPa.s}$ and average diameter of cell r=8µm, we derive the diffusion constant: $D=0.04(\mu m^2/s)$.

Image acquisition

The image acquisition was perform with 10x objective on Zeiss Axiovert 100M microscope equipped with a sensicam (PCO imaging) camera. The configuration has a resolution of 0.65 µm/pixel. Image acquisition was done in a multi-position mode collecting 120 fields of views in sequence using macros within the image software MicroManager[4]. A complete scan takes 3 minutes. Hence in the time-lapse

series cells typically exhibit an average displacement of 3 μm (5 pixels) within the scanning time intervals (from SI.Eq.2). The setting is good compromise between acquisition of a large number of cell data and a reasonable time resolution for tracking individual cells inside micro-wells.

To facilitate image processing, we have adopted a technique by Buggenthin et al.[5] and used out of focus images. While cells show a bright halo in the periphery when imaged in the focal plane by phase-contrast microscopy, in an out of focus image cells exhibit a bright center spot.

The microscope setup and heating system was turned on for at least 2 hours prior to experiment to equilibrate the temperature which minimizes the z drift. We observed a 1-2 μm z-shift over 3 days experiment which does not affect the image quality and cell-tracking.

Image processing

For cell tracking and image analysis, we have developed an in-house Java-based plug-in for ImageJ called MicroWellAnalysis (MWA). First module of MWA identifies the micro-well array, intensity threshold and micro-well size are given as inputs and software fit a smooth circle to the boundaries of micro-well. The second module automatically detects the wells with only single cell inside. An "Image stabilizer", a freely available plug-in[6] of ImageJ[7] software, corrects for scanning positioning errors by realigning all frames with respect to the micro-well pattern. In these wells, using a threshold value and average cell size, software tracks the position of the center of the cell with respect to the center of the well. The cell-recognition algorithm has an online threshold-value update and circularity check parameter to eliminate temporary changes in phase-contrast signal due to small morphological changes in cell. Trajectories of cells is exported into a customized Matlab code for change point analysis.

Change point analysis

Two separate methods were used to automatically detect the time point when cell change from non-adherent state to adherent. The displacement of cells by diffusion is analyzed by either Local standard deviation or a CUSUM analysis in order to determine the change point.

1- Local standard deviation

In our data-set, local standard deviation (σ_t) indicates the dispersion of displacement values for a defined number of steps (t) and is calculated from SI.Eq.4:

$$\sigma_t = \sqrt{\frac{1}{t-1}\sum_{N}^{N+t}(\Delta R_i - \overline{\Delta R}_t)^2} \quad \text{SI.Eq.4}$$

where N is the N^{th} data point and $\overline{\Delta R}_t$ is the local average of selected displacement (ΔR) values from N to N+t. We have selected an arbitrary number of 5 data-points to automatically find change point in the displacement data. In non-adherent state, cells more freedom in motion, hence their displacement values have higher deviation from mean, while in adherent state this deviation is much smaller.

Threshold value is defined for each experiment separately by user. It is possible that σ_5 drops temporarily below the threshold before the actual transition point. To discard these points, we introduced persistency criterion which checks if values below the threshold stays below the threshold for specific number of steps. If the algorithm finds more than one transition point, it automatically

increases the persistency steps. The point with longest persistence crossover of σ_5 from a threshold value to a lower value is reported as the transition point.

2- Cusum

Cusum[8] indicates the deviation of data from a global target value. In our data-set cusum cumulatively sums the difference of displacement of cell and its time-average, SI.Eq.5.

$$\text{cusum}_i = (\overline{\Delta R} - \Delta R) + \text{cusum}_{i-1} \qquad \text{SI.Eq.5}$$

displacement ΔR is the distance cell moves at each time-interval. The global time-average of displacement $\overline{\Delta R}$ was chosen as the reference value. Each state of motion has distinct distance from average value resulting in a constant slope for each state. A partial linear fit was fitted to the cusum data and all the changes in slopes were flagged. We select the prominent change in slope as the change point.

The cusum outcome confirmed that of σ_5 in most cases, and where discrepancies arose, the final decision was made manually by the user.

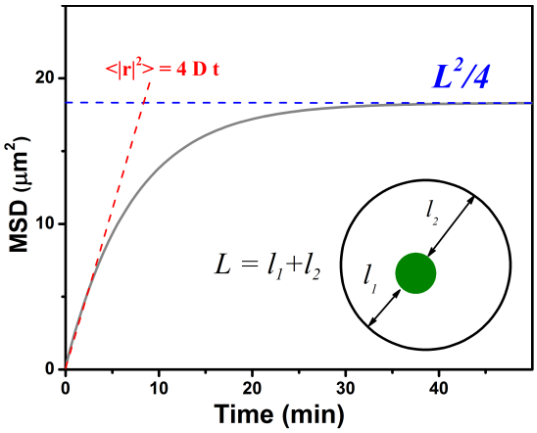

Fig.SI.1. Schematic of mean square displacement of a spherical particle confined inside a circulars domain. The red line is the fit to short time-scale values indicating the free diffusion coefficient and the blue line indicates the plateau value.

References of supplementary information

1. T. Benesch, S. Yiacoumi, and C. Tsouris, *Phys. Rev. E*, 2003, **68**, 021401.
2. T. Bickel, *Phys. A Stat. Mech. its Appl.*, 2007, **377**, 24–32.
3. A. Kusumi, Y. Sako, and M. Yamamoto, *Biophys. J.*, 1993, **65**, 2021–2040.
4. A. Edelstein, N. Amodaj, K. Hoover, R. Vale, and N. Stuurman, *Curr. Protoc. Mol. Biol.*, 2010, **Chapter 14**, Unit14.20.
5. F. Buggenthin, C. Marr, M. Schwarzfischer, P. S. Hoppe, O. Hilsenbeck, T. Schroeder, and F. J. Theis, *BMC Bioinformatics*, 2013, **14**, 297.
6. K. Li, 2008.
7. M. D. Abramoff, P. J. Magalhaes, and S. J. Ram, *Biophotonics Int.*, 2004, **11**, 36–42.
8. E. S. Page, *Biometrika*, 1954, **41**, 100–115.

Appendix B

Photolithography of SU-8 wafer

The pattern is designed according to guidelines and suggestions for microfluidic fabrication foundry of Harvard and softlithography fabrication [48]. All the photolithography steps are done in our in house cleanroom. The lithography step is done by ProtoLaser LDI (LPKF Laser & Elektronika, Naklo, Slovenia), with a laser with 375 nm wavelength and 1 µm spot diameter. The exposure time per spot and the distance between each exposed spots must be chosen, which was selectd with a dose-test pattern.

B.1 Single layer SU8 structure

The fabrication protocols for structures of ∼25 µm height is as follows:

1. Spin coat TI-prime:

Spin speed	Acceleration	Time
500 rpm	100 rpm/s	10 s
5000 rpm	1000 rpm/s	30 s

2. Bake at hotplate 120°C 2 min

3. Spin coat SU8 10:

Spin speed	Acceleration	Time
500 rpm	200 rpm/s	10 s
1000 rpm	300 rpm/s	30 s

4. Let the wafer rest on bench for ∼7 min.

5. Softbake on hotplate: @65°C for 3 min. :: @95°C for 7 min.

6. Follow the steps for ProtoLaser LDI, with this exposure parameters:
   600 mJ/cm^2 :: Coarse tool :: 0.3 point distance.

7. Postbake on hotplate: @65°C for 1 min :: @95°C for 3 min

8. Let the wafer cool down on bench for ∼2 min.

9. Develop in SU8-Dev 600 for 3 min. Divide the developer into two beakers with equal time.

10. Hardbake on hotplate:
    @65°C for 2 min. :: @95°C for 2 min. :: @160°C for 15 min. :: @65°C for 5 min. :: Cool down for 5 min.

B.2 Double layer SU8 structure

For cell sorting structures we used two thickness of SU-8 on two layers to make multi-thickness structures. The important issue in multi-layer structures are the baking temperature of SU8 layers, since too much or too low baking time could lead to cracks on the structure or layer lift off respectively. below is the complete protocol that worked for our sample.

First layer with SU8 10 (∼25 µm thickness)

1. Spin coat TI-prime:

Spin speed	Acceleration	Time
500 rpm	100 rpm/s	10 s
5000 rpm	1000 rpm/s	30 s

2. Bake at hotplate 120°C 2 min

3. Spin coat SU8 10:

Spin speed	Acceleration	Time
500 rpm	200 rpm/s	10 s
1000 rpm	300 rpm/s	30 s

4. Let the wafer rest on bench for ∼ 7 min.

5. Softbake on hotplate: @65°C for 3 min. :: @95°C for 7 min.

6. Follow the steps for ProtoLaser LDI, with this exposure parameters:
   500 mJ/cm^2 :: Fine tool :: 0.3 point distance.

7. Postbake on hotplate: @65°C for 50 s. :: @95°C for 2 min.

Second layer with SU8 100 (∼75 µm thickness)

1. Spin coat SU8 100:

Spin speed	Acceleration	Time
500 rpm	200 rpm/s	10 s
5000 rpm	1000 rpm/s	40 s

2. Let the wafer rest on bench for $\sim$ 10 min.
3. Softbake on hotplate: @65°C for 4 min. :: @95°C for 10 min.
4. Follow the steps for ProtoLaser LDI, with this exposure parameters:
   500 mJ/cm^2 :: Fine tool :: 0.3 point distance.
5. Postbake on hotplate: @65°C for 1min.. :: @95°C for 5 min.
6. Let the wafer cool down on bench for $\sim$2 min.
7. Develope in SU8-Dev 600 for 10 min. Devide the developer into two beakers with equal time.
8. Hardbake on hotplate:
   @65°C for 2 min. :: @95°C for 2 min. :: @160°C for 15 min. :: @65°C for 5 min. :: Cooldown for 5 min.

Appendix C

Softlithography and micromolding in capillary

PDMS was used to replicate the structures on the wafer and use them as the master for micromolding in capillaries (MIMIC) fabrication of PEGDA replica. PDMS is used in ratio of 10:1 of polymer:curing agent. Normally a less than 1 mm layer of PDMS is casted on top of the structured wafer and cured for more than 5 hours in 50°C convection oven.

The micro-pattern structures from PEGDA polymer is fabricated either on topas or glass substrates. Topas substrate (ibidi, Germany), are bio-compatible and durable under cell-culture medium condition. The glass slides with two thickness has been used for different sample preparation; 1mm thick glass are normal microscope slides (Roth, Germany), 180 µm thick glasses are typical microscopy cover slips (Roth, Germany). The dimensions of all of the substrates are $\sim 75 \times 25$ mm.

After the PDMS cured, follow below steps for MIMIC fabrication of PEGDA micropatterns on the substrate.

Important note: work under the hood or cleanroom environment as much as possible, it gives you cleaner final structure.

1. Clean substrates before use:
   Sonicate 10 min with 70% ethanol
   Sonicate 10 min with distilled water
   Blow dry with Pressurized air gun

2. Peal off PDMS from the silicon wafer, place it on cutting mat with structures up, cut the extra PDMS up to the edge of structurs.

3. Plasma treat surfaces of both PDMS and substrare (skip for glass substrates):
   Argon, 5 , 20mW for 30s

4. Prepare PEGDA by mixing 2% photo-initiator (2-Hydroxy-2-methylpropiophenone (Sigma-Aldrich, Germany)) to PEGDA monomer.

5. Place the plasma treated surfaces of PDMS on the substrate and add a drop of PEGDA precursor on the side of structure. Wait until it diffuses into the whole

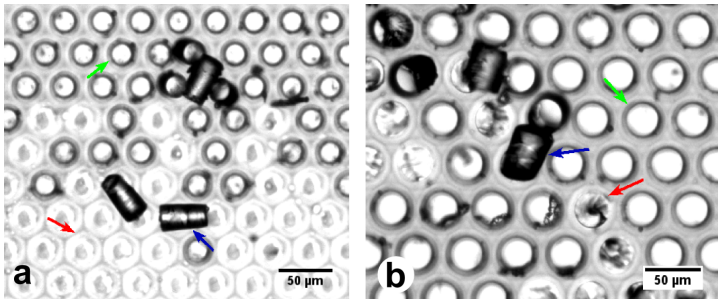

Figure C.1: a) A brightfield image of detached pillars from a PDMS stamps with 25 µm. b) Pillars on a 35 µm PDMS stamp was detached with force using tweezers. The arrows point to an example of intact pillar (green), place that a pillar is missing (red), and a detached pillar (blue).

structure.

6. Put the sample under UV light for 15 min to polymerize PEGDA.
7. Remove PDMS master from the structure and let it fully polymerize in the 50°C convection oven for another 6 hours.
8. Clean the structure as step 1 again, or do a plasma treatment as step 3.
9. Attach the ibidi sticky slide on top of the structures and let it cure in the the 50°C convection oven overnight.
10. Sample is ready, add the medium at least 2 hours before the experiment and make sure there is no bubble in structures. If you see the bubble, sonicate the sample for 2-3 min.

The glass substrates has to be silanized before PEGDA could adhere to it [36]. For silanization, put a drop of TMSPMA (3-(Trimethoxysilyl)propyl methacrylate) on a small tissue in a petri-dish together with the glass and let is rest under the hood overnight. Plasma treatment could harm the silanization, however it is good to do the plasma treatment after PEGDA polymerization is finished.

Reuse of PDMS master stamps

We has tested the reuse of PDMS master stamps after curing PEGDA and detaching the stamp from the substrate. The reusing was tested for up to 5 times, while the master with bigger structures (>35 µm) showed very little to no sign of wear, the smaller structures showed large scale fractures. After the 3rd reuse of 25 µm micro-wells, some of the stamps showed a visible irregularity in the structures. Light-microscopy inspection of patterns showed that PDMS pillars had been torn off from the PDMS (see Figure C.1). We speculate that this wearing is due to fatigue and micro-fractures in the micro-pillar over several use. It has been confirmed that PDMS has a low fatigue resistance [59].

We recommend that the PDMS not be used more than 3 times, especially with small patterns. However, a stamp with higher elastic modulus (lower than 10:1 base:linker ratio) could result in more robust stamps. While we observed some improvement in 5:1 PDMS ratio, we did not systematically check this properties.

Appendix D

Cell Fixation for SEM imaging

D.1 Buffer and fixture preparations

Phosphate buffer

For a pH of 7.2, have 72.6 % of buffer B and and 27.4 % of buffer A.

A) Potassium dihydrogen phosphate (KH_2PO_4): 9.078g per 1L of destilled water.

B) Disodium hydrogen phosphate ($Na_2HPO_4 \cdot 2\,H_2O$): 11.876g per 1L of destilled water.

Prepare this buffer with double concentration (mix with 500 ml instead of 1L) to be used in diluting the stuck of Glutaraldehyde.

Glutaraldehyde fixative

Normally the Glutaraldehyde vials are 25% concentrated but we need 2.5% concentration which is achieved by mixing:

- 1 ml of Glutaraldehyde stuck (25%).
- 4 ml of distilled water.
- 5 ml of Phosphate buffer (double concentration).

D.2 Fixation protocol

Aceton and HMDS (Hexamethyldisiloxane $C_6H_{18}OSi_2$) is corrosive for plastic, so you have to switch to ethanol step-dehydration and glass substrate.

To exchange the medium or wash the samples in ibidi-channels, we have followed the "Three times rule":

- Aspirate medium from the reserviors of channel, only leave medium inside the channel to cover the substrate.
- Add 100 µl of new medium from one reserve and discard 100 µl from the other side.
- Add 100 µl of new medium again. wait for minimum 30 second (or start with the next channels), then discard the 100 µl.

- Add enough new medium (80-100 ul) to fill the reservoirs till half of them.

Follow these steps to fixate and de-hydrate your cells properly, keep in mind that samples should never dry-out untill the final step.

1. Exchange medium with the buffer solution.
2. Exchange the buffer with Glutaraldehyde solution. 1×30 mins.
3. Exchange the solution back to buffer solution. 1×10 mins.
4. Wash with distilled water. 3×10 mins.
5. Wash with Ethanol 25%. 1×10 mins.
6. Wash with EtOH 50%. 1×10 mins.
7. Wash with EtOH 75%. 1×10 mins.
8. Wash with EtOH 95%. 1×10 mins.
9. Wash with EtOH 100%. 2×10 mins.
10. Use a sharp diamond cutter, scratch the sample from bottom: right before first channel, between 3rd and 4th and right after the last channel.
11. Put the whole sample under 100% EtOH and break the glass in that 3 lines (1 mm glass slides worked very nicely). Detach the sticky slide glued on top of structure with the help of your tweezers.
12. Still under EtOH, once the glass slides are free, remove the rest of the glue from glass (it should come off very easily).
13. Aspirate EtOH until there is only a thin film left on the slide.
14. Pour HMDS solution in a glass petri dish, and transfer the slides quickly into this dish.
15. Leave the sample overnight to slowly dry-out.
16. Store the sample in vacuum oven.

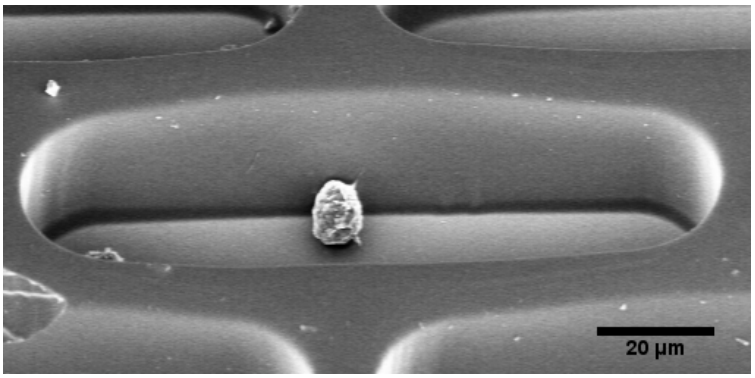

Figure D.1: SEM image of a single MOLM-13 suspension cell fixed by Glutaraldehyde inside a micro-slit structure.

Appendix E

Finite element analysis conditions

Elmer .sif file:

```
Header
  CHECK KEYWORDS Warn
  Mesh DB "." "."
  Include Path ""
  Results Directory ""
End

Simulation
  Max Output Level = 5
  Coordinate System = Cartesian
  Coordinate Mapping(3) = 1 2 3
  Simulation Type = Transient
  Steady State Max Iterations = 200
  Output Intervals = 2
  Timestepping Method = BDF
  BDF Order = 2
  Timestep intervals = 400
  Timestep Sizes = $ 40/400
  Solver Input File = case.sif
  Post File = case.ep
End

Constants
  Gravity(4) = 0 -1 0 9.82
  Stefan Boltzmann = 5.67e-08
  Permittivity of Vacuum = 8.8542e-12
  Boltzmann Constant = 1.3807e-23
  Unit Charge = 1.602e-19
```

```
End

Body 1
  Target Bodies(1) = 1
  Name = "Body 1"
  Equation = 1
  Material = 1
End

Solver 1
  Equation = Navier-Stokes
  Variable = Flow Solution[Velocity:2 Pressure:1]
  Procedure = "FlowSolve" "FlowSolver"
  Exec Solver = Always
  Stabilize = True
  Bubbles = False
  Lumped Mass Matrix = False
  Optimize Bandwidth = True
  Steady State Convergence Tolerance = 1.0e-5
  Nonlinear System Convergence Tolerance = 1.0e-7
  Nonlinear System Max Iterations = 200
  Nonlinear System Newton After Iterations = 3
  Nonlinear System Newton After Tolerance = 1.0e-3
  Nonlinear System Relaxation Factor = 0.5
  Linear System Solver = Iterative
  Linear System Iterative Method = BiCGStab
  Linear System Max Iterations = 500
  Linear System Convergence Tolerance = 1.0e-7
  Linear System Preconditioning = ILU0
  Linear System ILUT Tolerance = 1.0e-3
  Linear System Abort Not Converged = False
  Linear System Residual Output = 1
  Linear System Precondition Recompute = 1
End

Equation 1
  Name = "Navi"
  NS Convect = False
  Active Solvers(1) = 1
End

Material 1
  Name = "Air (room temperature)"
```

```
  Viscosity = 1.983e-5
  Heat expansion Coefficient = 3.43e-3
  Heat Conductivity = 0.0257
  Sound speed = 343.0
  Heat Capacity = 1005.0
  Density = 1.205
End

Boundary Condition 1
  Target Boundaries(1) = 1
  Name = "walls"
  Velocity 1 = 0.0
  Velocity 2 = 0.0
End

Boundary Condition 2
  Target Boundaries(1) = 2
  Name = "inlet"
  Velocity 1 = 200
  Velocity 2 = 0.0
End

Boundary Condition 3
  Target Boundaries(1) = 3
  Name = "outlet"
  Velocity 2 = 0.0
End
```

Appendix F

Cell Synchronization

F.1 Cell phases

Each individual cell goes through several stages to growth and divide to two daughter cells. The time from the birth of a single cell until it divides to two cells called cell cycle. The cell cycle consist of several phases:

G0 the resting phase where cells do neither divide nor grow;
G1 once the cell receives a signal to divide, it goes to this phase and starts growing;
S phase is when the chromosome (with DNA) is duplicated;
G2 phase is when the cell performs the final checks of DNA and prepares for division;
M phase is when the cell actually divides into two identical daughter cells.

These phases are shown in Figure F.1.

F.2 Protocol: Double Thymidine Block

In a normal cell population, each single cell can be at different cell phase. In order to bring all the cells in a specific cell phase, a process called cell synchronization is done. In our experiments we used a cell synchronization method based on thymidine drug. The

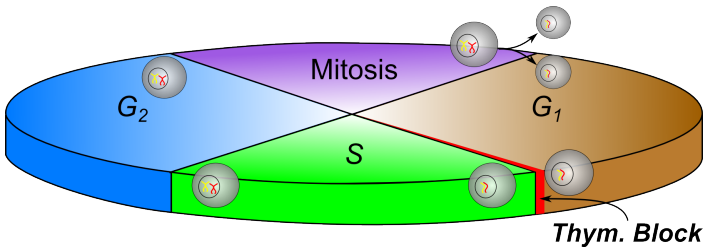

Figure F.1: Cell phases in one cell cycle.

double thymidine block which is used here follows the suggestions from Jackman et al.'s [116] methods report.

Medium

- Normal medium: RPMI 1640 (Lifetechnology, US) with stable glutamine. This supplements are added: 10% FCS, 1 mM Sodium Pyruvate.
- Blocking medium: Normal medium plus 2 mM Thymidine.

Thymidine stock
Prepare Thymidine stock solution with 100 mM concentration from powder (CAS 50-89-5, Calbiochem) by adding 242.2 mg of powder in 10 ml of PBS, after steering the solution, filter it using 0.22 µm filter.

1. First Block: Centrifuge an exponentially growing cell population and resuspend them in blocking medium. Incubate them for 24 hours.

2. Release: Centrifuge the medium, get rid of the medium as much as possible and resuspend in normal medium for 7-8 hours.

3. Second Block: Centrifuge and resuspend the cells in the blocking medium for 12 hours.

4. Synchronized population: Centrifuge and resuspend the cells in normal medium.

Appendix G

Gamma Convolutions

G.1 Gamma difference distribution

The difference of two gamma distributions is in principle a convolution of two gamma distributions. Mathai [134] and Klar [135] derived the solution for this distribution. The final equation can be either represented as an integral of exponential or with respect to Whittaker's W function. The below derivation is adopted from [134, 135].

X1 and X2 are two independent random variable with gamma functions $\Gamma(\alpha_1, \beta_1)$ and $\Gamma(\alpha_2, \beta_2)$, respectively. The difference is X = X1 - X2, the distribution of which is called gamma difference distribution (GDD) and to be derived here.

The sum of two variables is the convolution of their density functions. In this case f_{X1} and f_{-X2} where f_X is the gamma distribution function as in Equation G.1. Equation G.1 is the general form of Equation 3.2.

$$f_{X1}(x) = \frac{\beta_1^{\alpha_1} x^{\alpha_1 - 1} e^{\beta_1 x}}{\Gamma(\alpha_1)} \tag{G.1}$$

Same equation applies for f_{-X2} substituting x with $-y$. The covariance is calculated as:

$$f_X(z) = \int_{\infty}^{\infty} f_{X1}(x) f_{X2}(x - z) dx \tag{G.2}$$

Inserting the Equation G.1 in Equation G.2 and simplifying the equations will give us the final form in integral representation, this is equation 4 in [135]. Here $c = \beta_1^{\alpha_1} \beta_2^{\alpha_2} / (\Gamma(\alpha_1)\Gamma(\alpha_2))$:

$$f(z) = \begin{cases} c e^{\beta_2 z} \int_z^{\infty} x^{\alpha_1 - 1} (x - z)^{(\alpha_2 - 1)} e^{-(\beta_1 + \beta_2)x} dx & z > 0 \\ c e^{-\beta_1 z} \int_{-z}^{\infty} x^{\alpha_2 - 1} (x - z)^{(\alpha_1 - 1)} e^{-(\beta_1 + \beta_2)x} dx & z < 0 \end{cases} \tag{G.3}$$

Using the integral relation 3.383(4) (Equation G.4) from Gradshteyn et al. [190] the

integral equations can be written in Whittaker's W function (Equation 5 in [135])

$$\int_0^u x^{v-1}(x-u)^{\mu-1}e^{-\beta x}dx = \beta^{-\frac{\mu+v}{2}}u^{\frac{\mu+v-2}{2}}\Gamma(\mu)exp\left(-\frac{\beta u}{2}\right)W_{\frac{v-\mu}{2},\frac{1-\mu-v}{2}}(\beta u) \tag{G.4}$$

$$f(z) = \begin{cases} \frac{\tilde{c}}{\Gamma(\alpha_1)}z^{\frac{\alpha_1+\alpha_2}{2}-1}e^{\frac{\beta_2-\beta_1}{2}z}W_{\frac{\alpha_1-\alpha_2}{2},\frac{1-\alpha_1-\alpha_2}{2}}((\beta_1+\beta_2)z) & z>0 \\ \frac{\tilde{c}}{\Gamma(\alpha_1)}(-z)^{\frac{\alpha_1+\alpha_2}{2}-1}e^{\frac{\beta_1-\beta_2}{2}(-z)}W_{\frac{\alpha_1-\alpha_2}{2},\frac{1-\alpha_2-\alpha_1}{2}}((\beta_1+\beta_2)(-z)) & z<0 \end{cases} \tag{G.5}$$

where $\tilde{c}$

$$\tilde{c} = \frac{\beta_1^{\alpha_1}\beta_2^{\alpha_2}}{(\beta_1+\beta_2)^{(\alpha_1+\alpha_2)/2}} \tag{G.6}$$

We assume some simplifying conditions to get to an analytical expression for GDD. Since we are dealing with the sister cells, it is reasonable to assume that the initial gamma distributions has same parameters, hence $\beta_1 = \beta_2 = \beta$ and $\alpha_1 = \alpha_2 = \alpha$. With this, $\tilde{c} = \beta^\alpha/2$ and Equation G.5 for $z > 0$ becomes:

$$f(z) = \frac{\beta^\alpha}{2\Gamma(\alpha)}z^{\alpha-1}W_{0,\frac{1}{2}-\alpha}(2\beta z), z>0, z>0 \tag{G.7}$$

And approximating the Whittaker W function at $z \to 0$ for $\alpha > 0$ with:

$$W_{\kappa,\mu}(z) = \frac{\Gamma(2\mu)}{\Gamma\left(\frac{1}{2}+\mu-\kappa\right)}z^{\frac{1}{2}-\mu} + \frac{\Gamma(-2\mu)}{\Gamma\left(\frac{1}{2}-\mu-\kappa\right)}z^{\frac{1}{2}+\mu} + O(z^{\frac{3}{2}-\mu}) \tag{G.8}$$

For the case of similar distributions $\kappa = 0$ and $\mu = \frac{1}{2} - \alpha$:

$$W_{0,\frac{1}{2}-\alpha}(2\beta z) = \frac{\Gamma(1-2\alpha)}{\Gamma(1-\alpha)}(2\beta z)^\alpha + \frac{\Gamma(2\alpha-1)}{\Gamma(\alpha)}(2\beta z)^{1-\alpha} \tag{G.9}$$

The GDD equation becomes:

$$f(z) = 2^{\alpha-1}\beta^{2\alpha}\frac{\Gamma(1-2\alpha)}{\Gamma(\alpha)\Gamma(1-\alpha)}z^{2\alpha-1} + 2^\alpha\beta\frac{\Gamma(2\alpha-1)}{\Gamma(\alpha)^2}, z>0 \tag{G.10}$$

G.2 Gamma-normal distribution

Assuming the distribution of synchronized cells to be a normal distribution around the point of synchronization. We showed that the single cell response to chemotherapeutic drug has a gamma distribution. We proposed that in case of synchronized cell the drug-response curve would be a convolution of normal and gamma function.

There is no analytical solution for this convolution. However, Plancade et al. [191] showed a numerical approximation based on the Fast Fourier Transform of the data. The

convolution and it's representation with respect to Kummer's special function (kum) is shown in Equation G.12

$$f^{ng}_{\mu,\sigma,\alpha,\beta}(x) = \int f^{gam}_{\alpha,\beta}(t) f^{norm}_{\mu,\sigma}(x-t)dt \tag{G.11}$$

$f^{gam}_{\alpha,\beta}$ is the gamma distribution function and $f^{norm}_{\mu,\sigma}$ is a normal distribution function with parameters μ and σ

$$f^{ng}_{\mu,\sigma,\alpha,\beta}(x) = 2^{(1+\alpha/2)} \left(\frac{\sigma}{\beta}\right)^{\alpha} f^{norm}_{\mu,\sigma}(x) \left[\Gamma\left(\frac{\alpha}{2}\right) kum\left(\frac{\alpha}{2}, \frac{1}{2}, \frac{y^2}{2}\right) - \sqrt{2}y\Gamma\left(\frac{\alpha+1}{2}\right) kum\left(\frac{\alpha+1}{2}, \frac{3}{2}, \frac{y^2}{2}\right)\right] \tag{G.12}$$

$$y = \frac{\sigma^2 + \beta(\mu - x)}{\sigma\beta} \tag{G.13}$$

Symbols & Abbreviations

BCA	Biochemical component analysis
CFD	Computational fluid dynamics
DCLS	Direct classical least-squares
FACS	Fluorescence activated cell sorting
GDD	Gamma difference distribution
GMP	Granulocyte macrophage progenitor.
HSC	Hematopoietic stem cell.
iPS	induced pluripotent stem
LoC	Lab on a chip
MACS	Magnetic activated cell sorting
MEL	Murine erythroleukemia
MIMIC	Micromolding in capillaries
MOMP	Mitochondrial outer membrane permeabilization
MSD	Mean square displacement
MWA	MicroWell Analysis software
NA	Numerical aperture
NK	Natural killer cells
PCA	Principal component analysis
PCR	Polymerase chain reaction
pdf	Probability density function
PDMS	Polydimethylsiloxane
PEGDA	Polyethyleneglycol diacrylate
PEGDMA	Polyethyleneglycol dimethacrylate
PI	Propidium iodide
PLL	Poly-L-Lysine
TCP	Tissue culture plastic
TRAIL	Tumour necrosis factor (TNF)-related apoptosis-inducing ligand
CUSUM	Cumulative sum algorithm
Δt	Image acquisition interval
η	Refractive index

γ_0	Friction coefficient of a Brownian particle
κ	Stiffness of the optical trap
$\lambda(a)$	Loss factor of cell, due to division or death.
μ	Dynamic viscosity
σ	Standard deviation
σ_t	Local standard deviation of displacement of t steps
$\tau_{ave.}$	Average time it take for drug to kill cells.
$\tau_{min.}$	Onset of effect of drug.
a	Cell age, time from the division.
$cov(x, y)$	Covariance of the set of x and y data
D	Free diffusion coefficient
d	Particle diameter
d_C	Average diameter of single cell
d_W	Diameter of micro-well
L	Available distance of free motion
n	Cell number density
r	Pearson Correlation Coefficient
r_i	Position at time-point i
T_{d-c}	Onset of Caspase 3/7 marker for cell death.
T_{d-s}	Onset of cell size as a marker for cell death.
t_{div}	Doubling time of a cell
T_d	Time for drug to kill a cell.
v	Flow velocity

List of Figures

Acknowledgments

My heartfelt gratitude goes to my supervisor, **Prof. Dr. Joachim Rädler** who has been a wonderful mentor with illuminating inputs and invaluable guidance throughout my studies.

I am very thankful to **Susanne Rappl** who was essential part of the development of micro-patterning techniques. My special thanks goes to **Gerlinde Schwake** who patiently answered all my questions.

I would like to thank our external collaborators **Timm Schröder, Max Endele, Carsten Marr,** and **Felix Buggenthin** for their contribution and inputs on biological and statistical analysis of the data.

I am really thankful to my friends who over the years I enjoyed both their company as well as their insights and constructive criticism on my research: Athena R., Brian T. Carolin L., Ellisavet C, Matthias Z., Peter R., Rafal K., Tina M.

I am extremely grateful for the unconditional love and support of my family who always encouraged me to pursue my passions and follow my dreams around the world.

Bibliography

[1] Timm Schroeder. Long-term single-cell imaging of mammalian stem cells. *Nature methods*, 8(4 Suppl):S30–5, April 2011.

[2] Rainer Pepperkok and Jan Ellenberg. High-throughput fluorescence microscopy for systems biology. *Nature reviews. Molecular cell biology*, 7:690–696, 2006.

[3] Akiko Mammoto and Donald E Ingber. Cytoskeletal control of growth and cell fate switching. *Current Opinion in Cell Biology*, 21(6):864–870, December 2009.

[4] David G Spiller, Christopher D Wood, David A Rand, and Michael R H White. Measurement of single-cell dynamics. *Nature*, 465(7299):736–45, June 2010.

[5] Timm Schroeder. Imaging stem-cell-driven regeneration in mammals. *Nature*, 453(7193):345–51, May 2008.

[6] James C W Locke and Michael B Elowitz. Using movies to analyse gene circuit dynamics in single cells. *Nature reviews. Microbiology*, 7(5):383–92, May 2009.

[7] Diane Longo and Jeff Hasty. Dynamics of single-cell gene expression. *Molecular systems biology*, 2:64, 2006.

[8] Alejandro Colman-Lerner, Andrew Gordon, Eduard Serra, et al. Regulated cell-to-cell variation in a cell-fate decision system. *Nature*, 437(September):699–706, 2005.

[9] Erik Meijering, Oleh Dzyubachyk, and Ihor Smal. Methods for cell and particle tracking. *Methods in enzymology*, 504(February):183–200, January 2012.

[10] Simon Youssef, Sebastian Gude, and Joachim O Rädler. Automated tracking in live-cell time-lapse movies. *Integrative biology : quantitative biosciences from nano to macro*, 3(11):1095–101, November 2011.

[11] Felix Buggenthin, Carsten Marr, Michael Schwarzfischer, et al. An automatic method for robust and fast cell detection in bright field images from high-throughput microscopy. *BMC Bioinformatics*, 14(1):297, 2013.

[12] Eric Stern, Erin R Steenblock, Mark A Reed, and TM Tarek M Fahmy. Label-free electronic detection of the antigen-specific T-cell immune response. *Nano letters*, 8(10):3310–3314, September 2008.

[13] Pierre O Bagnaninchi and Nicola Drummond. Real-time label-free monitoring of adipose-derived stem cell differentiation with electric cell-substrate impedance sensing. *Proceedings of the National Academy of Sciences*, 108(16):6462–7, April 2011.

[14] Masaya Okada, Nicholas Isaac Smith, Almar Flotildes Palonpon, et al. Label-free Raman observation of cytochrome c dynamics during apoptosis. *Proceedings of the National Academy of Sciences of the United States of America*, 109(1):28–32, January 2012.

[15] Katharina Klein, Alexander M Gigler, Thomas Aschenbrenner, et al. Label-free live-cell imaging with confocal Raman microscopy. *Biophysical journal*, 102(2):360–8, January 2012.

[16] Charles H Camp, Siva Yegnanarayanan, Ali a Eftekhar, and Ali Adibi. Label-free flow cytometry using multiplex coherent anti-Stokes Raman scattering (MCARS) for the analysis of biological specimens. *Optics letters*, 36(12):2309–11, June 2011.

[17] Huabing Yin and Damian Marshall. Microfluidics for single cell analysis. *Current opinion in biotechnology*, 23(1):110–9, February 2012.

[18] Xuan Mu, Wenfu Zheng, Jiashu Sun, Wei Zhang, and Xingyu Jiang. Microfluidics for manipulating cells. *Small (Weinheim an der Bergstrasse, Germany)*, 9(1):9–21, January 2013.

[19] Adrian Ranga and Matthias P Lutolf. High-throughput approaches for the analysis of extrinsic regulators of stem cell fate. *Current opinion in cell biology*, 24(2):236–44, April 2012.

[20] Michal Polonsky, Irina Zaretsky, and Nir Friedman. Dynamic single-cell measurements of gene expression in primary lymphocytes: Challenges, tools and prospects. *Briefings in Functional Genomics*, 12(2):99–108, 2013.

[21] Ina Kurth, Katja Franke, Tilo Pompe, Martin Bornhäuser, and Carsten Werner. Hematopoietic stem and progenitor cells in adhesive microcavities. *Integrative biology*, 1(5-6):427–34, June 2009.

[22] Konstantinos D Kokkaliaris, Dirk Loeffler, and Timm Schroeder. Advances in tracking hematopoiesis at the single-cell level. *Current opinion in hematology*, 19(4):243–249, July 2012.

[23] MA Michael A Rieger, PS Philipp S Hoppe, BM Benjamin M Smejkal, Andrea C Eitelhuber, and Timm Schroeder. Hematopoietic cytokines can instruct lineage choice. *Science*, 325(5937):217–218, July 2009.

[24] J F Kerr, A H Wyllie, and A R Currie. Apoptosis: a basic biological phenomenon with wide-ranging implications in tissue kinetics. *British journal of cancer*, 26(4):239–57, August 1972.

[25] Thomas G Cotter. Apoptosis and cancer: the genesis of a research field. *Nature reviews. Cancer*, 9(7):501–7, July 2009.

[26] Lisa Bouchier-Hayes, Cristina Muñoz Pinedo, Samuel Connell, and Douglas R Green. Measuring apoptosis at the single cell level. *Methods (San Diego, Calif.)*, 44(3):222–8, March 2008.

[27] A. Gonzalez, Stevan. Timing is everything: stochastic origins of cell-to-cell variability in cancer cell death. *Frontiers in Bioscience*, 16(1):307, 2011.

[28] David C Duffy, J Cooper Mcdonald, Olivier J A Schueller, and George M Whitesides. Polydimethylsiloxane (PDMS) on SU-8 Mold. *Emergency Medical Services*, 73246(617):2–4, 1998.

[29] Enoch Kim, Younan Xia, and GM Whitesides. Micromolding in capillaries: Applications in materials science. *Journal of the American Chemical ...*, 7863(Figure 1):5722–5731, 1996.

[30] L E Dike, C S Chen, M Mrksich, et al. Geometric control of switching between growth, apoptosis, and differentiation during angiogenesis using micropatterned substrates. *In vitro cellular & developmental biology. Animal*, 35(8):441–8, September 1999.

[31] M. a. Unger. Monolithic Microfabricated Valves and Pumps by Multilayer Soft Lithography. *Science*, 288(5463):113–116, April 2000.

[32] Klaus Eyer, Phillip Kuhn, Conni Hanke, and Petra S Dittrich. A microchamber array for single cell isolation and analysis of intracellular biomolecules. *Lab on a chip*, 12(4):765–72, February 2012.

[33] George M Whitesides. The origins and the future of microfluidics. *Nature*, 442(7101):368–373, July 2006.

[34] Jason P Mazzoccoli, Donald L Feke, Harihara Baskaran, and Peter N Pintauro. Mechanical and cell viability properties of crosslinked low- and high-molecular weight poly(ethylene glycol) diacrylate blends. *Journal of biomedical materials research. Part A*, 93(2):558–66, May 2010.

[35] Michael P Cuchiara, Alicia C B Allen, Theodore M Chen, Jordan S Miller, and Jennifer L West. Multilayer microfluidic PEGDA hydrogels. *Biomaterials*, 31(21):5491–7, July 2010.

[36] Hannes-Christian Moeller, Matthew K Mian, Shamit Shrivastava, Bong Geun Chung, and Ali Khademhosseini. A microwell array system for stem cell culture. *Biomaterials*, 29(6):752–763, February 2008.

[37] Ali Khademhosseini, Judy Yeh, Sangyong Jon, et al. Molded polyethylene glycol microstructures for capturing cells within microfluidic channels. *Lab on a chip*, 4(5):425–30, October 2004.

[38] Jeffrey M Karp, Judy Yeh, George Eng, et al. Controlling size, shape and homogeneity of embryoid bodies using poly(ethylene glycol) microwells. *Lab on a chip*, 7(6):786–94, June 2007.

[39] Vicki I. Chin, Philippe Taupin, Sandeep Sanga, et al. Microfabricated platform for studying stem cell fates. *Biotechnology and bioengineering*, 88(3):399–415, November 2004.

[40] Jeffrey C Mohr, Juan J de Pablo, and Sean P Palecek. 3-D microwell culture of human embryonic stem cells. *Biomaterials*, 27(36):6032–42, December 2006.

[41] Anna-Kristina Marel, Susanne Rappl, Alicia Piera Alberola, and Joachim Oskar Rädler. Arraying cell cultures using PEG-DMA micromolding in standard culture dishes. *Macromolecular bioscience*, 13(5):595–602, May 2013.

[42] Chang Mo Hwang, Woo Young Sim, Seung Hwan Lee, et al. Benchtop fabrication of PDMS microstructures by an unconventional photolithographic method. *Biofabrication*, 2(4):045001—-, 2010.

[43] Lifeng Kang, Matthew J Hancock, Mark D Brigham, and Ali Khademhosseini. Cell confinement in patterned nanoliter droplets in a microwell array by wiping. *Journal of biomedical materials research. Part A*, 93(2):547–57, May 2010.

[44] Seung Hwan Lee, Won Gu Lee, Bong Geun Chung, Jae Hong Park, and Ali Khademhosseini. Rapid Formation of Acrylated Microstructures by Microwave-Induced Thermal Crosslinking. *Macromolecular rapid communications*, 30(16):1382–1386, June 2009.

[45] Chad I Rogers, Jayson V Pagaduan, Gregory P Nordin, and Adam T Woolley. Single-monomer formulation of polymerized polyethylene glycol diacrylate as a nonadsorptive material for microfluidics. *Analytical chemistry*, 83(16):6418–25, August 2011.

[46] Sandro Cesaro-Tadic, Gregor Dernick, David Juncker, et al. High-sensitivity miniaturized immunoassays for tumor necrosis factor alpha using microfluidic systems. *Lab on a chip*, 4(6):563–9, December 2004.

[47] Kenneth R Hawkins and Paul Yager. Nonlinear decrease of background fluorescence in polymer thin-films - a survey of materials and how they can complicate fluorescence detection in microTAS. *Lab on a chip*, 3(4):248–52, November 2003.

[48] Younan Xia and George M Whitesides. Soft lithography. *Annual Review of Materials Science*, 28(1):153–184, August 1998.

[49] Dong Qin, Younan Xia, and George M Whitesides. Soft lithography for micro- and nanoscale patterning. *Nature protocols*, 5(3):491–502, March 2010.

[50] Weiqiang Chen, Raymond H W Lam, and Jianping Fu. Photolithographic surface micromachining of polydimethylsiloxane (PDMS). *Lab on a chip*, 12(2):391–5, January 2012.

[51] Ningsong Qu, Xiaolei Chen, Hansong Li, and Di Zhu. Fabrication of PDMS micro through-holes for electrochemical micromachining. *The International Journal of Advanced Manufacturing Technology*, 72(1-4):487–494, February 2014.

[52] Albert Folch, B H Jo, Octavio Hurtado, David J Beebe, and Mehmet Toner. Microfabricated elastomeric stencils for micropatterning cell cultures. *Journal of biomedical materials research*, 52(2):346–53, November 2000.

[53] Jongchan Choi, Kyeong-Hwan Lee, and Sung Yang. Fabrication of PDMS through-holes using the MIMIC method and the surface treatment by atmospheric-pressure CH 4 /He RF plasma. *Journal of Micromechanics and Microengineering*, 21(9):097001—-, 2011.

[54] Enoch Kim, Younan Xia, and George M Whitesides. Polymer microstructures in capillaries. *Nature*, 376:581–584, 1995.

[55] Jacqueline R Rettig and Albert Folch. Large-Scale Single-Cell Trapping And Imaging Using Microwell Arrays. *Anal. Chem.*, 77(17):5628–5634, July 2005.

[56] Christophe Geuzaine and Jean-François Remacle. Gmsh: a three-dimensional finite element mesh generator with built-in pre- and post-processing facilities. *International Journal for Numerical Methods in Engineering*, 79(11):1309–1331, 2009.

[57] Xiaolin Wang, Shuxun Chen, Yu Ting Chow, et al. A microengineered cell fusion approach with combined optical tweezers and microwell array technologies. *RSC Advances*, 3(45):23589, 2013.

[58] Emmanuel Delamarche, Heinz Schmid, Bruno Michel, and Hans Biebuyck. Stability of molded polydimethylsiloxane microstructures. *Advanced Materials*, 9(9):741–746, 1997.

[59] Sung Hwan Kim, Jin Hee Moon, Jeong Hun Kim, Sung Min Jeong, and Sang Hoon Lee. Flexible, stretchable and implantable PDMS encapsulated cable for implantable medical device. *Biomedical Engineering Letters*, 1(3):199–203, 2011.

[60] R. Ian Freshney. *Culture of Animal Cells Set*, volume 82. 2000.

[61] C Geers and G Gros. Carbon dioxide transport and carbonic anhydrase in blood and muscle. *Physiological reviews*, 80:681–715, 2000.

[62] W. J. Thomas and M. J. Adams. Measurement of the diffusion coefficients of carbon dioxide and nitrous oxide in water and aqueous solutions of glycerol. *Transactions of the Faraday Society*, 61:668, 1965.

[63] Yu-Chieh Chiu, EricM. Brey, and VÃctorH. PÃrez Luna. A Study of the Intrinsic Autofluorescence of Poly (ethylene glycol)-co-(L -Lactic acid) Diacrylate. *Journal of Fluorescence*, 22(3):907–913—-, 2012.

[64] Richard S Hotchkiss, Andreas Strasser, Jonathan E McDunn, and Paul E Swanson. Cell death. *The New England journal of medicine*, 361(16):1570–83, October 2009.

[65] Ram Dixit and Richard Cyr. Cell damage and reactive oxygen species production induced by fluorescence microscopy: effect on mitosis and guidelines for non-invasive fluorescence microscopy. *The Plant Journal*, 36(2):280–290, October 2003.

[66] V. Krishnamurthy and Ihab L. Kamel. Argon plasma treatment of glass surfaces. *Journal of Materials Science*, 24:3345–3352, 1989.

[67] Dale Muzzey and Alexander van Oudenaarden. Quantitative time-lapse fluorescence microscopy in single cells. *Annual review of cell and developmental biology*, 25(June):301–27, January 2009.

[68] Valentin Magidson and Alexey Khodjakov. Circumventing photodamage in live-cell microscopy. *Methods in cell biology*, 114:545–60, January 2013.

[69] Artifacts of light. *Nature Methods*, 10(12):1135–1135, November 2013.

[70] David I Pattison and Michael J Davies. *Cancer: Cell Structures, Carcinogens and Genomic Instability*, volume 96 of *Experientia Supplementum*. Birkhäuser-Verlag, Basel, 2006.

[71] Michael D Abramoff, Paulo J Magalhaes, and Sunanda J Ram. Image Processing with ImageJ. *Biophotonics international*, 11(7):36–42, 2004.

[72] Kang Li. The image stabilizer plugin for {ImageJ}, February 2008.

[73] Jens Rietdorf. Bleach Correction, 2005.

[74] Farzad Sekhavati, Max Endele, Susanne Rappl, et al. Marker-free detection of progenitor cell differentiation by analysis of Brownian motion in micro-wells. *Integr. Biol.*, 7:178–183, 2015.

[75] Matthias P Lutolf, Penney M Gilbert, and Helen M Blau. Designing materials to direct stem-cell fate. *Nature*, 462(7272):433–41, November 2009.

[76] Chantal S Léger and Thomas J Nevill. Hematopoietic stem cell transplantation: a primer for the primary care physician. *CMAJ : Canadian Medical Association journal = journal de l'Association medicale canadienne*, 170(10):1569–1577, 2004.

[77] Kazutoshi Takahashi and Shinya Yamanaka. Induction of pluripotent stem cells from mouse embryonic and adult fibroblast cultures by defined factors. *Cell*, 126(4):663–76, August 2006.

[78] Martin Evans. Discovering pluripotency: 30 years of mouse embryonic stem cells. *Nature reviews. Molecular cell biology*, 12(10):680–6, October 2011.

[79] Michael A Rieger and Timm Schroeder. Instruction of lineage choice by hematopoietic cytokines. *Cell Cycle*, 8(1538-4101):4019–4020, December 2009.

[80] Carsten Marr, Michael Strasser, Michael Schwarzfischer, Timm Schroeder, and Fabian J Theis. Multi-scale modeling of GMP differentiation based on single-cell genealogies. *FEBS Journal*, 279(18):3488–3500, September 2012.

[81] National Institutes of Health, Department of Health Services., and Human. Stem cells: scientific progress and future research directions. Technical report, National Institutes of Health, Department of Health and Human Services, 2001.

[82] Peter Johan Friedrich Röttgermann, Alicia Piera Alberola, and Joachim Oskar Rädler. Cellular Self-Organization on Micro-Structured Surfaces. *Soft Matter*, 2013.

[83] Michael J Saxton and Ken Jacobson. Single particle tracking: Applications to Membrane Dynamics. *Annu. Rev. Biophys. Biomol. Struct.*, 26(1):373–399, June 1997.

[84] Anthony M.J. Davis, Michael T. Kezirian, and Howard Brenner. On the Stokes-Einstein Model of Surface Diffusion along Solid Surfaces: Slip Boundary Conditions. *Journal of Colloid and Interface Science*, 165(1):129–140, June 1994.

[85] Thomas Bickel. A note on confined diffusion. *Physica A: Statistical Mechanics and its Applications*, 377(1):24–32, April 2007.

[86] E. S. ES S Page. Continuous inspection schemes. *Biometrika*, 41(1):100–115, June 1954.

[87] OA A Grigg, V T Farewell, and D J Spiegelhalter. Use of risk-adjusted CUSUM and RSPRT charts for monitoring in medical contexts. *Stat Methods Med Res*, 12(2):147–170, April 2003.

[88] David Dingli, Arne Traulsen, and Jorge M. Pacheco. Stochastic Dynamics of Hematopoietic Tumor Stem Cells. *Cell Cycle*, 6(4):461–466, February 2007.

[89] J C Reed. Dysregulation of apoptosis in cancer. *Journal of clinical oncology*, 17(9):2941–53, September 1999.

[90] Shinji Miwa, Shuya Yano, Hiroaki Kimura, et al. Cell-cycle fate-monitoring distinguishes individual chemosensitive and chemoresistant cancer cells in drug-treated heterogeneous populations demonstrated by real-time FUCCI imaging. *Cell Cycle*, 14(4):621–629, 2014.

[91] G Kroemer, L Galluzzi, P Vandenabeele, et al. Classification of cell death: recommendations of the Nomenclature Committee on Cell Death 2009. *Cell death and differentiation*, 16(1):3–11, January 2009.

[92] David Hockenbery. Defining apoptosis. *The American journal of pathology*, 146(1):16–19, 1995.

[93] G Majno and I Joris. Apoptosis, oncosis, and necrosis. An overview of cell death. *The American journal of pathology*, 21(8):34–42, August 1995.

[94] B. E Trump, I. K. Berezesky, S. H. Chang, and P. C. Phelps. The Pathways of Cell Death: Oncosis, Apoptosis, and Necrosis. *Toxicologic Pathology*, 25(1):82–88, January 1997.

[95] Laurence Calzone, Laurent Tournier, Simon Fourquet, et al. Mathematical modelling of cell-fate decision in response to death receptor engagement. *PLoS Computational Biology*, 6(3), 2010.

[96] Guido Kroemer, Lorenzo Galluzzi, and Catherine Brenner. Mitochondrial membrane permeabilization in cell death. *Physiological reviews*, 87(1):99–163, January 2007.

[97] S W G Tait and D R Green. Caspase-independent cell death: leaving the set without the final cut. *Oncogene*, 27(50):6452–61, October 2008.

[98] Linda E Bröker, Frank A E Kruyt, and Giuseppe Giaccone. Cell death independent of caspases: a review. *Clinical cancer research : an official journal of the American Association for Cancer Research*, 11(9):3155–62, May 2005.

[99] Susan Elmore. Apoptosis: a review of programmed cell death. *Toxicologic pathology*, 35(4):495–516, June 2007.

[100] Inna N Lavrik, Alexander Golks, and Peter H Krammer. Caspases: pharmacological manipulation of cell death. *The Journal of clinical investigation*, 115(10):2665–72, October 2005.

[101] Tom Vanden Berghe, Andreas Linkermann, Sandrine Jouan-Lanhouet, Henning Walczak, and Peter Vandenabeele. Regulated necrosis: the expanding network of non-apoptotic cell death pathways. *Nature reviews. Molecular cell biology*, 15(2):135–47, February 2014.

[102] D L Vaux, S Cory, and J M Adams. Bcl-2 gene promotes haemopoietic cell survival and cooperates with c-myc to immortalize pre-B cells., 1988.

[103] John C. Reed, Cy Stein, C. Subasinghe, et al. Antisense-mediated inhibition of BCL2 protooncogene expression and leukemic cell growth and survival: Comparisons of phosphodiester and phosphorothioate oligodeoxynucleotides. *Cancer Research*, 50:6565–6570, 1990.

[104] Douglas R Green and Guido Kroemer. Pharmacological manipulation of cell death: clinical applications in sight? *The Journal of clinical investigation*, 115(10):2610–7, October 2005.

[105] Vincent T DeVita and Edward Chu. A history of cancer chemotherapy. *Cancer research*, 68(21):8643–53, November 2008.

[106] F Sasse, B Kunze, T M Gronewold, and H Reichenbach. The chondramides: cytostatic agents from myxobacteria acting on the actin cytoskeleton. *Journal of the National Cancer Institute*, 90(20):1559–63, October 1998.

[107] F Foerster, S Braig, C Moser, et al. Targeting the actin cytoskeleton: selective antitumor action via trapping PKC. *Cell death & disease*, 5(8):e1398, January 2014.

[108] Magdalena H Menhofer, Dominik Bartel, Johanna Liebl, et al. In vitro and in vivo characterization of the actin polymerizing compound chondramide as an angiogenic inhibitor. *Cardiovascular research*, pages 1–12, September 2014.

[109] H Ehrhardt, F Wachter, M Grunert, and I Jeremias. Cell cycle-arrested tumor cells exhibit increased sensitivity towards TRAIL-induced apoptosis. *Cell death & disease*, 4:e661, 2013.

[110] Sabrina L Spencer, Suzanne Gaudet, John G Albeck, John M Burke, and Peter K Sorger. Non-genetic origins of cell-to-cell variability in TRAIL-induced apoptosis. *Nature*, 459(7245):428–32, May 2009.

[111] Subhadip Raychaudhuri. How can we kill cancer cells: Insights from the computational models of apoptosis. *World journal of clinical oncology*, 1(1):24–8, November 2010.

[112] John G Albeck, John M Burke, Bree B Aldridge, et al. Quantitative analysis of pathways controlling extrinsic apoptosis in single cells. *Molecular cell*, 30(1):11–25, April 2008.

[113] L Galluzzi, I Vitale, J M Abrams, et al. Molecular definitions of cell death subroutines: recommendations of the Nomenclature Committee on Cell Death 2012. *Cell death and differentiation*, 19(1):107–20, January 2012.

[114] Oded Sandler, Sivan Pearl Mizrahi, Noga Weiss, et al. Lineage correlations of single cell division time as a probe of cell-cycle dynamics. *Nature*, 2015.

[115] Y Matsuo, R A F MacLeod, C C Uphoff, et al. Two acute monocytic leukemia (AML-M5a) cell lines (MOLM-13 and MOLM-14) with interclonal phenotypic heterogeneity showing MLL-AF9 fusion resulting from an occult chromosome insertion, ins(11;9)(q23;p22p23). *Leukemia*, 11(9):1469–1477, December 1997.

[116] J Jackman and P M O'Connor. Methods for synchronizing cells at specific stages of the cell cycle. *Current protocols in cell biology*, Chapter 8:Unit 8.3, May 2001.

[117] J Matas, O Chum, M Urban, and T Pajdla. Robust wide-baseline stereo from maximally stable extremal regions. *Image and Vision Computing*, 22(10):761–767, September 2004.

[118] Nicolas Chenouard, Ihor Smal, Fabrice de Chaumont, et al. Objective comparison of particle tracking methods. *Nature methods*, 11(3):281–9, March 2014.

[119] Donald Wlodkowic, Joanna Skommer, Dagmara McGuinness, et al. Chip-based dynamic real-time quantification of drug-induced cytotoxicity in human tumor cells. *Analytical chemistry*, 81(16):6952–9, August 2009.

[120] M Schwarzfischer and P S Hoppe T Schroeder F J Theis C. Marr J. Krumsiek. Efficient fluorescence image normalization for time lapse movies. In *In Proc. Microscopic Image Analysis with Applications in Biology*, September 2011.

[121] Paul Bogdan, Bridget M Deasy, Burhan Gharaibeh, Timo Roehrs, and Radu Marculescu. Heterogeneous structure of stem cells dynamics: statistical models and quantitative predictions. *Scientific reports*, 4:4826, January 2014.

[122] Gregory Driessens, Benjamin Beck, Amélie Caauwe, Benjamin D Simons, and Cédric Blanpain. Defining the mode of tumour growth by clonal analysis. *Nature*, 488(7412):527–30, August 2012.

[123] Walter M. Gregory, Michael A. Richards, Maurice L. Slevin, and Robert L. Souhami. A Mathematical Model Relating Response Durations to Amount of Subclinical Resistant Disease. *Cancer Research*, 51(4):1210–1216, 1991.

[124] Heinz von Foerster. Some remarks on Changing Populations. In Fredik Jr. Stohlman, editor, *Kinetics of Cellular Proliferation*, pages 382–407. Grune and Stratton, New York, NY, 1959.

[125] Evgeny B. Stukalin, Ivie Aifuwa, Jin Seob Kim, Denis Wirtz, and Sean X. Sun. Age-dependent stochastic models for understanding population fluctuations in continuously cultured cells. *Journal of The Royal Society Interface*, 10(85):20130325, 2013.

[126] Zoltán Kutalik, Moe Razaz, Anders Elfwing, András Ballagi, and József Baranyi. Stochastic modelling of individual cell growth using flow chamber microscopy images. *International Journal of Food Microbiology*, 105(2):177–190, 2005.

[127] Ha Youn Lee and Alan S. Perelson. Modeling T cell proliferation and death in vitro based on labeling data: Generalizations of the Smith-Martin cell cycle model. *Bulletin of Mathematical Biology*, 70:21–44, 2008.

[128] David G Kendall. On the Role of Variable Generation Time in the Development of a Stochastic Birth Process. *Biometrika*, 35(3):316–330, 1948.

[129] E O Powell. Some Features of the Generation Times of Individual Bacteria. *Biometrika*, 42(1):16–44, 1955.

[130] J Baranyi and C Pin. A parallel study on bacterial growth and inactivation. *Journal of theoretical biology*, 210(3):327–336, 2001.

[131] Kazufumi Hosoda, Tomoaki Matsuura, Hiroaki Suzuki, and Tetsuya Yomo. Origin of lognormal-like distributions with a common width in a growth and division process. *Physical Review E - Statistical, Nonlinear, and Soft Matter Physics*, 83(3):1–5, 2011.

[132] Karl Pearson. Note on Regression and Inheritance in the Case of Two Parents. *Proceedings of the Royal Society of London (1854-1905)*, 58(-1):240–242, January 1895.

[133] Joseph Lee Rodgers and W Alan Nicewander. Thirteen Ways to Look at the Correlation Coefficient. *The American Statistician*, 42(1):59, February 1988.

[134] A.M. Mathai. On Noncentral Generalized Laplacianness of Quadratic Forms in Normal Variables. *Journal of Multivariate Analysis*, 45(2):239–246, 1993.

[135] Bernhard Klar. A note on gamma difference distributions. *Journal of Statistical Computation and Simulation*, (1):1–8, 2015.

[136] Trevor Stewart, Leo Strijibosch, Hans Moors, and Paul van Batenburg. A Sample Approximation to the convolution of Gamma Distributions. 2007.

[137] Stephanie Heinrich, Eva-Maria Geissen, Julia Kamenz, et al. Determinants of robustness in spindle assembly checkpoint signalling. *Nature cell biology*, 15(11):1328–39, 2013.

[138] Ulfert Rand, Melanie Rinas, Johannes Schwerk, et al. Multi-layered stochasticity and paracrine signal propagation shape the type-I interferon response. *Molecular Systems Biology*, 8(584):1–13, 2012.

[139] Naama Geva-Zatorsky, Nitzan Rosenfeld, Shalev Itzkovitz, et al. Oscillations and variability in the p53 system. *Molecular systems biology*, 2:2006.0033, 2006.

[140] Sabrina L. Spencer and Peter K. Sorger. Measuring and modeling apoptosis in single cells. *Cell*, 144(6):926–939, 2011.

[141] Sabine Schmitz. *Der Experimentator: Zellkultur*. 2011.

[142] Stephan H K Eder, Alexander M Gigler, Marianne Hanzlik, and Michael Winklhofer. Submicrometer-scale mapping of magnetite crystals and sulfur globules in magnetotactic bacteria using confocal Raman micro-spectrometry. *PloS one*, 9(9):e107356, January 2014.

[143] Robert Keiner, Torsten Frosch, Stefan Hanf, et al. Raman spectroscopy - An innovative and versatile tool to follow the respirational activity and carbonate biomineralization of important cave bacteria. *Analytical Chemistry*, 85:8708–8714, 2013.

[144] Nina Kamennaya, Caroline Ajo-Franklin, Trent Northen, and Christer Jansson. Cyanobacteria as Biocatalysts for Carbonate Mineralization. *Minerals*, 2:338–364, 2012.

[145] S. Koch, H. Walles, K. H. Krause, et al. Novel cell identification: markerfree and suitable for living cells. In Volker Deckert and Nirmala Ramanujam, editors, *Clinical and Biomedical Spectroscopy and Imaging III*, page 87980J, Munich, June 2013.

[146] Tobias J Moritz, Douglas S Taylor, Denise M Krol, John Fritch, and James W Chan. Detection of doxorubicin-induced apoptosis of leukemic T-lymphocytes by laser tweezers Raman spectroscopy. *Biomedical optics express*, 1(4):1138–1147, January 2010.

[147] Eva Brauchle, Sibylle Thude, Sara Y Brucker, and Katja Schenke-Layland. Cell death stages in single apoptotic and necrotic cells monitored by Raman microspectroscopy. *Scientific reports*, 4:4698, January 2014.

[148] Kerstin Ramser, Jonas Enger, Mattias Goksör, et al. A microfluidic system enabling Raman measurements of the oxygenation cycle in single optically trapped red blood cells. *Lab on a chip*, 5(4):431–6, April 2005.

[149] Flavius C Pascut, Spandan Kalra, Vinoj George, et al. Non-invasive label-free monitoring the cardiac differentiation of human embryonic stem cells in-vitro by Raman spectroscopy. *Biochimica et biophysica acta*, 1830(6):3517–24, June 2013.

[150] Paul H C Eilers. A perfect smoother. *Analytical Chemistry*, 75(14):3631–3636, 2003.

[151] Zhi-Min Zhang, Shan Chen, and Yi-Zeng Liang. Baseline correction using adaptive iteratively reweighted penalized least squares. *The Analyst*, 135(2):1138–1146, 2010.

[152] Komsta. Comparison of several methods of chromatographic baseline removal with a new approach based on quantile regression. *Chromatographia*, 73:721–731, 2011.

[153] Dominique van de Sompel, Ellis Garai, Cristina Zavaleta, and Sanjiv Sam Gambhir. A hybrid least squares and principal component analysis algorithm for Raman spectroscopy. *PLoS ONE*, 7(6), 2012.

[154] M. J. Pelletier. Quantitative analysis using Raman spectrometry. *Applied Spectroscopy*, 57, 2003.

[155] Richard D Snook, Timothy J Harvey, Elsa Correia Faria, and Peter Gardner. Raman tweezers and their application to the study of singly trapped eukaryotic cells. *Integrative biology*, 1(1):43–52, January 2009.

[156] Silvia Caponi, Lavinia Liguori, Alessandra Giugliarelli, et al. Raman micro-spectroscopy: a powerful tool for the monitoring of dynamic supramolecular changes in living cells. *Biophysical chemistry*, 182:58–63, December 2013.

[157] Yi Hong Ong, Mayasari Lim, and Quan Liu. Comparison of principal component analysis and biochemical component analysis in Raman spectroscopy for the discrimination of apoptosis and necrosis in K562 leukemia cells: errata. *Optics Express*, 20(20):25041, 2012.

[158] Alina Zoladek, Flavius C. Pascut, Poulam Patel, and Ioan Notingher. Non-invasive time-course imaging of apoptotic cells by confocal Raman micro-spectroscopy. *Journal of Raman Spectroscopy*, 42(3):251–258, March 2011.

[159] Zanyar Movasaghi, Shazza Rehman, and Ihtesham U. Rehman. Raman Spectroscopy of Biological Tissues. *Applied Spectroscopy Reviews*, 42(5):493–541, September 2007.

[160] T. H. Maiman. Stimulated Optical Radiation in Ruby, 1960.

[161] A Ashkin. Acceleration and Trapping of Particles by Radiation Pressure. *Physical Review Letters*, 24(4):156–159, January 1970.

[162] A Ashkin. Forces of a single-beam gradient laser trap on a dielectric sphere in the ray optics regime. *Biophysical journal*, 61(2):569–582, 1992.

[163] Keir C Neuman and Attila Nagy. Single-molecule force spectroscopy: optical tweezers, magnetic tweezers and atomic force microscopy. *Nature methods*, 5(6):491–505, June 2008.

[164] Michael a. Taylor, Joachim Knittel, and Warwick P. Bowen. Fundamental constraints on particle tracking with optical tweezers. *New Journal of Physics*, 15, 2013.

[165] P. C. Chaumet and M. Nieto-Vesperinas. Coupled Dipole Method Determination of the Electromagnetic Force on a Particle over a Flat Dielectric Substrate. 61(20):10, 2003.

[166] Yasuhiro Harada and Toshimitsu Asakura. Radiation forces on a dielectric sphere in the Rayleigh scattering regime. *Optics Communications*, 124(March):529–541, 1996.

[167] T.a. Nieminen, H. Rubinsztein-Dunlop, N.R. Heckenberg, and H Heckenberg N R Nieminen T. A. Rubinsztein-Dunlop. Calculation and optical measurement of laser trapping forces on non-spherical particles. *Journal of Quantitative Spectroscopy and Radiative Transfer*, 70(4-6):627–637, August 2001.

[168] K Svoboda and S M Block. Biological Applications of Optical Forces. *Annu. Rev. Biophys. Biomol. Struct.*, 23(1):247–285, June 1994.

[169] Robert; Spidich James A.; Chu Steven Finer Jeffrey; Simmons. Optical trap system and method, April 1996.

[170] K. Visscher, S.P. Gross, and S.M. Block. Construction of multiple-beam optical traps with nanometer-resolution position sensing. *IEEE Journal of Selected Topics in Quantum Electronics*, 2(4):1066–1076, 1996.

[171] Kirstine Berg-Sø rensen and Henrik Flyvbjerg. Power spectrum analysis for optical tweezers. *Review of Scientific Instruments*, 75(3):594, 2004.

[172] Filipp V. Ignatovich, Achim Hartschuh, and Lukas Novotny. Detection of nanoparticles using optical gradient forces. *Journal of Modern Optics*, 50(10):1509–1520, January 2003.

[173] J T Finer, R M Simmons, and J a Spudich. Single myosin molecule mechanics: piconewton forces and nanometre steps. *Nature*, 368:113–119, 1994.

[174] K Svoboda, C F Schmidt, B J Schnapp, and S M Block. Direct observation of kinesin stepping by optical trapping interferometry. *Nature*, 365:721–727, 1993.

[175] A D Mehta, J T Finer, and J A Spudich. Reflections of a lucid dreamer: optical trap design considerations. *Methods in cell biology*, 55:47–69, 1998.

[176] M W Berns, J R Aist, W H Wright, and H Liang. Optical trapping in animal and fungal cells using a tunable, near- infrared titanium-sapphire laser. 198:375–378, 1992.

[177] Peter J. F. Röttgermann, Samira Hertrich, Ida Berts, et al. Cell Motility on Polyethylene Glycol Block Copolymers Correlates to Fibronectin Surface Adsorption. *Macromolecular Bioscience*, 14:1755–1763, 2014.

[178] Jean-Christophe Baret, Oliver J Miller, Valerie Taly, et al. Fluorescence-activated droplet sorting (FADS): efficient microfluidic cell sorting based on enzymatic activity. *Lab on a chip*, 9(13):1850–1858, 2009.

[179] Shia-Yen Teh, Robert Lin, Lung-Hsin Hung, and Abraham P Lee. Droplet microfluidics. *Lab on a chip*, 8(2):198–220, 2008.

[180] Xiaolin Wang, Xue Gou, Shuxun Chen, Xiao Yan, and Dong Sun. Cell manipulation tool with combined microwell array and optical tweezers for cell isolation and deposition. *Journal of Micromechanics and Microengineering*, 23(7):075006, July 2013.

[181] Ali Asgar S Bhagat, Hansen Bow, Han Wei Hou, et al. Microfluidics for cell separation. *Medical and Biological Engineering and Computing*, 48(10):999–1014, October 2010.

[182] Daniel R Gossett, Westbrook M Weaver, Albert J Mach, et al. Label-free cell separation and sorting in microfluidic systems. *Analytical and bioanalytical chemistry*, 397(8):3249–67, August 2010.

[183] T N Buican, M J Smyth, H a Crissman, et al. Automated single-cell manipulation and sorting by light trapping. *Applied optics*, 26(24):5311–5316, 1987.

[184] a. Ashkin, J. M. Dziedzic, and T. Yamane. Optical trapping and manipulation of single cells using infrared laser beams. *Nature*, 330(6150):769–771, 1987.

[185] Kerstin Ramser and Dag Hanstorp. Optical manipulation for single-cell studies. *Journal of biophotonics*, 3(4):187–206, April 2010.

[186] Hu Zhang and Kuo-Kang Liu. Optical tweezers for single cells. *Journal of the Royal Society, Interface / the Royal Society*, 5(24):671–90, July 2008.

[187] J. R. Kovac and J. Voldman. Intuitive, image-based cell sorting using optofluidic cell sorting. *Analytical Chemistry*, 79(24):9321–9330, 2007.

[188] Nien-Tsu Huang, Hua-Li Zhang, Meng-Ting Chung, Jung Hwan Seo, and Katsuo Kurabayashi. Recent advancements in optofluidics-based single-cell analysis: optical on-chip cellular manipulation, treatment, and property detection. *Lab on a chip*, 14(7):1230–45, 2014.

[189] Chunsun Zhang and Da Xing. Miniaturized PCR chips for nucleic acid amplification and analysis: Latest advances and future trends. *Nucleic Acids Research*, 35(13):4223–4237, 2007.

[190] I. S. Gradshteyn and I. M. Ryzhik. *Table of Integrals, Series, and Products*. 7 edition, 2007.

[191] Sandra Plancade, Yves Rozenholc, and Eiliv Lund. Generalization of the normal-exponential model: exploration of a more accurate parametrisation for the signal distribution on Illumina BeadArrays. *BMC bioinformatics*, 13(1):329, 2012.